CFD Analysis of Steady State Flow Reaction Forces in a Rim-Spool Valve

A Thesis Submitted to the
College of Graduate Studies and Research
In Partial Fulfillment of the Requirements
for the Degree of Master of Science
in the Department of Mechanical Engineering,
University of Saskatchewan, Saskatoon
Canada

By
Norense Okungbowa

Permission to Use

In presenting this thesis in partial fulfillment of the requirements for a postgraduate degree from the University of Saskatchewan, I agree that the Libraries of this University may make it freely available for inspection. I further agree that the permission for copying this thesis in any manner, in whole or in part for scholarly purposes, may be granted by the professors who supervised my work or, in their absence, by the Head of the Department or Dean of the College in which my thesis work was conducted. It is understood that any copying or publication or use of this thesis or parts thereof for financial gain shall not be allowed without my written permission. It is also understood that due recognition shall be given to me and to the University of Saskatchewan in any scholarly use which may be made of any material in my thesis.

Request for permission to copy or to make other use of material in this thesis, in whole or part, should be addressed to:

Head, Department of Mechanical Engineering
University of Saskatchewan
College of Engineering
57 Campus Drive
Saskatoon, Saskatchewan, S7N 5A9
Canada

Acknowledgements

Firstly, I would like to thank my supervisors, Professors R. T. Burton and D. J. Bergstrom for their general guidance and help during my research.

I would like to acknowledge the support of many professors in the Mechanical Engineering Department of the University of Saskatchewan. I appreciate the sound instruction I received in the graduate courses taught by Professors Burton, Bergstrom, Bugg, Sumner and Habibi. They have greatly influenced my vision and appreciation of scientific knowledge.

A special thanks to Doug Bitner of the Fluid Power Lab for his dedication. This work has been made possible by his constant support and guidance.

I would also like to acknowledge the support of my family who have been a source of strength and encouragement throughout my education.

Most importantly, I thank the Holy One who gave me the dream, the vision, the provision, the guidance, the strength, the support, the victory and the future.

Abstract

Hydraulic spool valves are found in most hydraulic circuits in which flow is to be modulated. Therefore their dynamic performance is critical to the overall performance of the circuit. Fundamental to this performance is the presence of flow reaction forces which act on the spool. These forces can result in the necessity of using two stage devices to drive the spool and in some cases have been directly linked to valve and circuit instabilities. As such, a great deal of research and design has concentrated on ways to reduce or compensate for flow forces. In one particular series of studies conducted on flow divider valves, it was established that a rim machined into the land of the spool reduced the flow dividing error by approximately 70-80%, and it was deduced that the main contribution to this error was flow forces. Direct verification of the claim regarding flow force reduction was not achieved and hence was the motivation for this particular study.

This thesis will consider the reaction (flow) force associated with a conventional spool land and one with a rim machined into it, and a modified form of the rimmed land referred to as a "sharp edge tapered rim spool land". The rim and the sharp edge tapered rim were specially designed geometrical changes to the lands of the standard spool in order to reduce the large steady state flow forces (SSFF) inherent in the standard spool valve. In order to analyze the flow field inside the interior passages of the valve, three configurations of the spool were considered for orifice openings of 0.375, 0.5, 0.75 and 1.05 *mm*. Computational Fluid Dynamics (CFD) analysis was used to describe the fluid mechanics associated with the steady state flow forces as it provided a detailed structure of the flow through the valve, and to identify the flow mechanism whereby flow forces are reduced by the machining of a rim and tapered rim on the land of the spool. For all openings of the spool, the sharp tapered rim valve provides the largest reduction in SSFF. It was also observed that for all cases studied, the inflow SSFF's were smaller than for the outflow conditions

The prediction of the steady state flow force on the rim spool was investigated in a flow divider valve configuration, and the results from the CFD analysis indicated a reduction by approximately 70%.

Contents

Permission to Use ..... **ii**
Acknowledgements ..... **iii**
Abstract ..... **iv**
Contents ..... **vi**
List of Figures ..... **x**
List of Tables ..... **xv**
Nomenclature ..... **xvii**

1 Introduction **1**

1.1 Background 1
1.2 Physical Representation of Flow Reaction Forces 3
1.3 Literature Review 5
1.4 Lumped Parameter (LP) and CFD Approach 8
1.5 Research Objectives 9
1.6 Thesis Overview 9

2 Basic Valve Operation and Models for Steady Flow Forces in a Spool Valve **11**

2.1 Basic Components and Operation of Hydraulic Spool Valve 11
2.2 Steady State Flow Forces (SSFF) Equations 14
2.2.1 Lumped Parameter (LP) Model 15
2.2.2 Differential Model 16
2.2.2.1 Near Wall Treatment 18
2.2.2.2 Discretization 19
2.2.2.3 Finite Volume Method (FVM) 19
2.2.2.4 The SIMPLE Algorithm 20
2.2.2.4.1 Discrete Transport Equations 21
2.2.2.4.2 The Pressure Equation 22

2.2.2.4.3 Solution Procedure 25
2.2.3 Boundary Conditions 26
2.2.4 Estimating Steady State Flow Forces (SSFF) 27
2.2.5 Summary 28

3 Development of Numerical Model Using CFX 5.6 Tool-kit 29

3.1 Numerical Methodology 30
3.2 Definition of the Problem 30
3.3 Solution Procedure Using CFX 5.6 33
3.3.1 CFX-Build 33
3.3.1.1 Specify Geometry 34
3.3.1.2 Meshing 34
3.3.2 CFX-Pre 36
3.3.2.1 Inlet Boundary 37
3.3.2.2 Outlet Boundary 38
3.3.2.3 Wall Boundary 38
3.3.2.4 Symmetry Boundary 39
3.3.3 CFX-Solver 39
3.3.4 CFX-Post 40
3.4 Results and Discussions ..... **Error! Bookmark not defined.**
3.4.1 Comparison of CFX 5.6 Prediction to Gao's PIV and FEM Results 45
3.5 Summary 48

4 Simulation Results and Analysis of the Flow Field inside the Spool Valve 50

4.1 Introduction 50
4.2 Geometrical Model of Standard Spool Valve 50
4.3 Boundary Conditions 55
4.4 Fluid Properties 56
4.5 Solution Process 56
4.6 Near-Wall Resolution 59

4.7 Simulation Results 59
4.7.1 Analysis of the Flow Field 59
4.7.2 Measuring the Fluid Jet Angle 69
4.7.3 Flow Reaction Forces 71
4.7.4 Comparison of CFD with the Classical Equation 72
4.8 Inflow Condition for the Standard Spool Valve 74
4.9 Compensating for SSFF 78
4.9.1 Rim Spool Valve 79
4.9.2 Describing the Flow Field (Rim Spool Valve) 80
4.9.3 Comparison of TSSFF and Fluid Jet Angle for Standard and Rim Spool Valve 84
4.9.4 Discussions 86
4.9.5 Comparison of SSFF for the Standard and Rim Spool Valve (Inflow Condition) 87
4.10 Further Modification to the Rim Spool Valve 88
4.10.1 Sharp Edge Tapered Rim Spool Valve 88
4.11 Summary 97

5 Application of CFD to a Rimmed Flow Divider Valve 98

5.1 Model and Describing Equations of the Flow Divider Valve 98
5.2 Simulation Results 104
5.2.1 Results from the Dynamic Model 104
5.2.2 CFD Model 108
5.3 Summary 112

6 Conclusions and Recommendations for Future Research 113

6.1 Summary of Accomplishments 113
6.2 Conclusions 114
6.3 Contributions 115
6.4 Future Research 115

References **117**
A Modeling Steady Flow Forces (Lumped Parameter Approach) 121
B Analytical Solutions for Steady Laminar Flow Between Parallel Plates for Viscous, Incompressible Fluid 134
C The 2-D Incompressible Navier-Stokes Equations 141
D1 Geometry Creation and Mesh Generation using the Commercial CFD Software Module CFX-Build 149
D2 Defining the Flow Physics in CFX-Pre 155
D3 Visualizing the Results in CFX-Post 160
E Numerical Methodology ..... **Error! Bookmark not defined.**
F1 Calculation of the Fluid Jet Angle from CFD Results 170
F2 Velocity Plots for the Inflow Conditions 173
F3 Velocity and Pressure Contours for Spool Opening of 0.375 and 0.75 mm for the Outflow 179
G Model Parameters and Dynamic Model 185

List of Figures

Figure 1. 1: Standard and rim spool valve configuration 3
Figure 1. 2: Development of flow reaction forces 4
Figure 1. 3: A flow divider valve 6

Figure 2. 1: Schematic of a spool valve (critically centered i.e. $x_v = 0$) 12
Figure 2. 2: Operation of a spool valve (spool displaced to the right, i.e. $x_v > 0$) 13
Figure 2. 3: Control Volume and nomenclature for the valve studied 16
Figure 2. 4: Finite volume grid structure 20
Figure 2. 5: A staggered grid structure. 21
Figure 2. 6: A schematic of the flow domain for a typical spool valve 26

Figure 3. 1: 2-D valve geometry 31
Figure 3. 2: Geometry of the flow model used in CFX 5.6 33
Figure 3. 3: The rectangular grid (fine mesh) 34
Figure 3. 4: A section of the inlet mesh. 35
Figure 3. 5: A section of the outlet mesh. 36
Figure 3. 6: The inlet velocity profile (10) 38
Figure 3. 7: The velocity vector field for a spool opening of 0.375 cm 41
Figure 3. 8: The velocity field for a spool opening of 0.75 cm 43
Figure 3. 9: The velocity vector field for a spool opening of 1.125 cm 44
Figure 3. 10: Locations in the outlet port where velocity profiles are compared 45
Figure 3. 11: Vertical velocity profiles at y = 1.419 cm 46
Figure 3. 12: Vertical velocity profiles at y = 1.892 cm 46
Figure 3. 13: Horizontal velocity at y = 1.419 cm for a spool opening of 0.375 cm 47
Figure 3. 14: Horizontal velocity at y = 1.892 cm for a spool opening of 0.375 cm 48

Figure 4.1. 1: Assembly of 3-D spool valve 51
Figure 4.1. 2: 3-D spool and rod 51

Figure 4.1. 3: Representation of the 3-D model by a 2-D model..... 52
Figure 4.1. 4: Representation of the inlet and outlet slots on the sleeve..... 53
Figure 4.1. 5: The true representation of the 2-D model of the valve..... 53

Figure 4. 1: Schematic of the model geometry for a standard spool valve..... 55
Figure 4. 2: Simulation approach..... 56
Figure 4. 3: Velocity vector of the flow field showing recirculation zones 61
Figure 4. 4: Pressure plot for the standard spool configuration (*xv* = 0.5 mm). 62
Figure 4. 5: Pressure plot for the standard spool configuration for an increased pressure level..... 64
Figure 4. 6: Static pressure plot on the right land face 65
Figure 4. 7: Static pressure plot on the left land face..... 66
Figure 4. 8: Cross-sectional plots for the standard spool configuration 67
Figure 4. 9: X-Y plots for the standard spool configuration showing the static pressure along a line section in the chamber..... 68
Figure 4. 10: Velocity plot through gap (orifice opening)..... 69
Figure 4. 11: Velocity contour for the standard (non-rimmed) spool configuration for the inflow condition (*xv* = 0.5 mm) 75
Figure 4. 12: Pressure contour for the standard (non-rimmed) spool configuration for inflow condition (*xv* = 0.5 mm) 76
Figure 4. 13: Static pressure plot on the left and right land faces..... 77
Figure 4. 14: Schematic of the model geometry of a rim spool valve. 80
Figure 4. 15: Velocity vector for the rim spool valve configuration 81
Figure 4. 16: Pressure contour for the rim spool valve configuration 83
Figure 4. 17: Visualization of the velocity for the standard and rim spool valve..... **Error! Bookmark not defined.**
Figure 4. 18: Schematic of the sharp edge tapered rim geometry 89
Figure 4. 19: Velocity vector for the sharp edge tapered rim spool valve configuration . 91
Figure 4. 20: Pressure contour for the sharp edge tapered rim spool valve configuration 93
Figure 4. 21: X-Y plot of SSFF for different spool openings for the outflow condition.. 95

Figure 4. 22: X-Y plot showing the % reduction in SSFF for the outflow condition..... 97

Figure 5. 1: Schematic of a flow divider valve with the rim (6)..... 99
Figure 5. 2: Spool position..... 102
Figure 5. 3: Spool positioning of the flow divider valve (simulated from the dynamic valve)..... 104
Figure 5. 4: Pressure plot (dynamic model) for the flow divider valve without the rim 105
Figure 5. 5: Pressure plot (dynamic model) for the flow divider valve with the rim 106
Figure 5. 6: Load flow rates through the flow divider valve 107
Figure 5. 7: Flow forces on the flow dividing valve..... 108

Figure 5.8. 1: Velocity contour for the flow dividing valve WOR (x_{v1} = 0.174 cm; x_{v2} = 0.226 cm) 109
Figure 5.8. 2: Pressure contour for the flow dividing valve WOR (x_{v1} = 0.174 cm; x_{v2} = 0.226 cm) 110

Figure 5.9. 1: Velocity contour for the flow dividing valve WR (x_{v1} = 0.164 cm; x_{v2} = 0.236 cm) 110
Figure 5.9. 2: Pressure contour for the flow dividing valve WR (x_{v1} = 0.164 cm; x_{v2} = 0.236 cm) 111

Figure A1. 1: Schematic of the fluid control volume for a metering–out valve chamber 123

Figure A2. 1: Schematic of the fluid control volume for metering–in valve chamber... 130

Figure B. 1: Typical velocity and shear stress distribution of the viscous flow between parallel fixed plates..... 134

Figure C2. 1: Control volume 145

Figure E1. 1: Typical velocity profile in turbulent flow near a wall 163

Figure E4. 1: The vertical velocity profile at y = 1.419 cm for a spool opening of 0.75 cm. 167
Figure E4. 2: The vertical velocity profile at y = 1.892 cm for a spool opening of 0.75 cm. 168
Figure E4. 3: The vertical velocity profile at y = 1.419 cm for a spool opening of 1.125 cm. 168
Figure E4. 4: The vertical velocity profile at y = 1.892 cm for a spool opening of 1.125 cm. 169

Figure F1. 1: Estimation of velocity streamlines showing the jet angle 171
Figure F1. 2: Vector Diagram 171

Figure F2.1. 1: Velocity contour of the flow field of the standard spool valve for a meter–in orifice (x_v = 0.5 mm) 173
Figure F2.1. 2: Pressure contour of the flow field of the standard spool valve for a meter–in orifice (x_v = 0.5 mm) 174

Figure F2.2. 1: Velocity contour of the flow field of the rim spool valve for a meter–in orifice (x_v = 0.5 mm)..... 175
Figure F2.2. 2: Pressure contour of the flow field of the rim spool valve for a meter–in orifice (x_v = 0.5 mm)..... 176

Figure F2.3. 1: Velocity contour of the flow field of the sharp edge tapered rim spool for a meter – in orifice (x_v = 0.5 mm)..... 177
Figure F2.3. 2: Pressure contour of the flow field of the sharp edge tapered rim spool for a meter – in orifice (x_v = 0.5 mm)..... 178

Figure F3.1. 1: Velocity contour for the standard spool configuration 179
Figure F3.1. 2: Pressure contour plot for the standard spool configuration 180

Figure F3.2. 1: Velocity contour for the rim spool valve configuration 181
Figure F3.2. 2: Pressure contour for the rim spool valve configuration 182

Figure F3.3. 1: Velocity contour for the sharp edge tapered rim spool valve configuration 183
Figure F3.3. 2: Pressure contour for the sharp edge tapered rim spool valve configuration 184

Figure G. 1: Schematic of a Flow Divider Valve without the rim (6) 186
Figure G. 2: The dynamic model 188

List of Tables

Table 3. 1: The number of nodes used for Gao and CFX 5.6 simulations 36

Table 4. 1: Grids used to test the refinement for simulation done for spool opening of 0.5 *mm.* 58

Table 4. 2: The estimated jet angle from CFD analysis for standard spool land 70

Table 4. 3: The TSSFF estimated using the CFD approach compared to the classical approach 72

Table 4. 4: Percentage of the viscous friction to TSSFF on the spool 73

Table 4. 5: The estimated SSFF from CFD results for the inflow condition as compared to the outflow condition 78

Table 4. 6: The estimated jet angle, TSSFF and SSFF from CFD analysis for rim spool land (rim thickness t_{rim} = 0.8 mm) 84

Table 4. 7: The estimated jet angle and TSSFF from CFD analysis for standard and rim spool land (rim thickness t_{rim} = 0.8 mm) 85

Table 4. 8: The estimated jet angle and TSSFF from CFD analysis for standard spool and rimmed land (t_{rim} = 1 mm) 86

Table 4. 9: The longitudinal momentum flux for both the Standard and rim spool valve with rim thinckness of 0.8 mm 87

Table 4. 10: The SSFF for both the standard and rim spool valve with a rim thinckness of 0.8 mm for a meter–in orifice 88

Table 4. 11: The estimated jet angle and SSFF from CFD analysis for the standard, rim spool land (rim thickness t_{rim} = 0.8 mm) and the sharp edge tapered rim (outflow condition) 94

Table 4. 12: The SSFF for the standard, rim (t = 0.8 mm) and sharp edge tapered rim (inflow condition) 95
Table 4. 13: Percentage reduction of TSSFF by the Rim and Sharp Edge Tapered Rim compared to the standard land Spool (Outflow condition) 96
Table 5.1: Flow forces and jet stream angle for the flow divider valve (pressure differential across the ports of 1.2 MPa and rim thickness of 0.16 mm) 112
Table G. 1: The parameter values used in the dynamic model 187

Nomenclature

$\%E_{ss}$	Steady state error [%]
β	Bulk modulus [Pa]
ΔP	Pressure drop across the orifice (CFD model) [Pa]
θ_i	Discharge angle at port i [^{0}]
δ_{ij}	Kronecker delta
η	Switching function (1 or 0)
Ω	Magnitude of the vorticity
ω	The inverse of the turbulence time scale, [s^{-1}]
ρ	Fluid density [kg/m^3]
μ	Viscosity of the fluid [Pa.s]
μ_t	Turbulent viscosity [Pa.s]
$k = (1/2)\overline{u_i' u'}$	Turbulence kinetic energy [m^2/s^2]
τ_{rod}	Shear stress acting on the rod [N/m^2]
τ_{sleeve}	Shear stress acting on the sleeve [N/m^2]
$\frac{\partial V_x}{\partial y}$	Velocity gradient of V_x in the y direction [s^{-1}]
$\rho\overline{u_i' u_j'}$	Reynolds stress tensor [$kg/m.s^2$]
a_1	A constant
A_{eff}	Effective area on the spool on which the pressure act [m^2]
A_s	Area of the sleeve [m^2]
A_{pi}	The spool area of surface i [m^2]

A_{vi}	Flow divider variable orifice *i* [m^2]
A_0	Area of the orifice (CFD model) [m^2]
B	Flow divider spool damping coefficient. [N.s/m]
C_C	Contraction coefficient
C_D	Discharge coefficient (assume constant in this study)
d	The rim depth [m]
D_{eff}	Effective diameter of the spool [m]
D_L	Diameter of the land [m]
D_R	Diameter of the rod [m]
$\vec{F}_{spool}$	Steady state reaction force on the spool [N]
F_{fi}	The flow reaction force on flow divider surface *i* [N]
F_f	The frictional force [N]
i	Subscript that refers to the two outlets ports 1 & 2
K_i	The flow divider orifice *i* valve coefficient [$m^3/kg]^{1/2}$
l	The length between lands [m]
l_c	The length within the chamber in which flow is significant [m]
m	The mass of the flow divider spool [kg]
$\overline{P}$	Mean pressure [Pa]
P_A	Pressure acting on land surface A [Pa]
P_B	Pressure acting on land surface B [Pa]
P_{ii}	The pressure acting on flow divider land surface *i* [Pa]
P_{Li}	The load port pressure at port *i* for the flow divider valve [Pa]
P_s	The supply pressure (constant) [Pa]
Q_s	The supply flow [m^3/s]
Q_i	The flow through orifice *i* on the flow divider valve [m^3/s]
SSFF	The Steady State Flow Forces [N]
TSSFF	The Total Steady State Flow Forces [N]
t_r	The rim thickness [m]
u_i	Velocity component in the x_i direction [m/s]

u_i'	Fluctuating velocity component in the x_i direction [m/s]
u_j'	Fluctuating velocity component in the x_j direction [m/s]
$\overline{U}_i$	Mean velocity component in the x_i direction; [m/s]
v	Velocity component in the y - direction [m/s]
$\overline{U}_j$	Mean velocity component in the x_j direction; [m/s]
x	The spool displacement from centre for the flow dividing valve [m]
x_{vi}	The opening displacement of orifice i for the flow divider valve [m]
$\dot{x}$	The velocity of the spool [m/s]
$\ddot{x}$	The acceleration of the spool [m/s^2]
w	The area gradient for the flow divider valve (width of flow domain) [m]

Chapter 1

Introduction

1.1 Background

Hydraulic valves are a very important component in any hydraulic system. The primary functions of these valves are to control the rate of flow, the direction of flow, and the pressure in hydraulic systems. They directly affect the dynamic performance of the hydraulic system. Valve dynamics determine the basic response and stability characteristics of hydraulic systems since they are often the only actively controlling component in the system.

Valves may be of the poppet type, rotary spool type, or the sliding spool type. Unlike the on/off seat poppet type which allows flow in only one direction, the sliding spool type can handle flows in multiple directions by adding extra lands and ports. This capability to direct flows in multiple directions makes the spool valve the most common type of control valve used in fluid power applications. The valve can be operated by shifting the spool manually, hydraulically by a pilot stage, or directly by an electromagnetic solenoid, or some combination thereof.

Inherent to all types of valve is the presence of a highly nonlinear reaction force which is often referred to as a "flow reaction force" (to be discussed in detail later). These forces can be described as the effect of momentum changes as oil flows through the valve. The flow force has both steady and transient components. The steady flow force is the most dominant and acts in a direction so as to close the valve. The transient flow force is a function of the spool velocity, and can either be a positive or a negative damping force depending on the direction of the flow.

These inherent flow forces are undesirable for two main reasons. Because these forces are a function of the product of pressure drop and orifice opening, the force term is highly non-linear. This introduces non-linearities to the valve operation and could cause the valve to become unstable. Second, since flow forces always act in a direction so as to close the valve, the forces could affect the metering accuracy of the valve. The magnitude of flow forces is proportional to the pressure drop and flow rate across the valve. Thus for high bandwidth and high flow rate applications, these forces become significant in which a larger external force (more commonly referred to as the stroking force) is needed to actuate the spool. The stroking force has to overcome the forces acting on the spool which includes inertial forces, frictional forces and the dominant force, the flow force.

Many attempts have been made to overcome flow forces by the use of one or more pilot stage valves or by using large (high power) solenoids. The problem with these methods is that the use of one or more pilot stage valves introduces higher order dynamics to the valve operation (which makes control design more challenging); in addition, larger solenoid actuators are usually expensive and have distinct force limitations (usually in the order of 45 N to 90 N). Such force limitations limit single stage electro-hydraulic servo-valves to low performance applications (1).

Merritt (1) prescribed two methods by which the flow forces can be reduced. One way is to place many small holes symmetrically around the valve sleeve so that the angle at which the fluid leaves the metering orifice reaches 90^o when the hole is completely uncovered. The second method of compensation is to increase the shank diameter at both ends. The problem with the first method is that it introduces additional non-linearities to the valve operation because of the round holes, while the second method is effective only at large flows. Other researchers such as Borghi et al (2), Bao et al (3), and very recently, Jyh et al (4) have compensated for the flow forces by modifying the spool geometry. Finke et al, (5) compensated for flow forces by substantially varying the spool geometry. In their design study, the flow forces were reduced from 25 N to 9 N at a pressure drop of 320 bars by adding a compensation cone to the spool and a full angular scallop to the body.

Chan (6) and Chan et al (7) at the University of Saskatchewan reduced flow forces by designing a novel configuration of a spool with a rim machined into it (Figure 1.1) to reduce the flow division error in a flow divider valve.

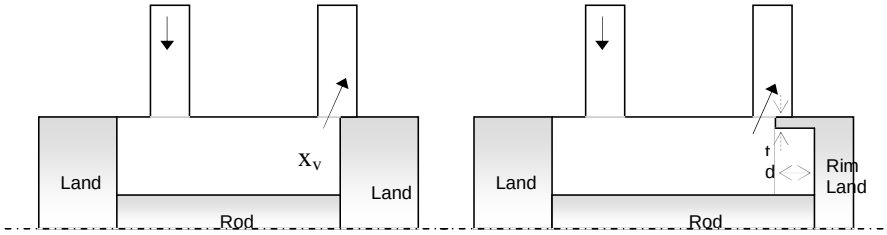

(a) Typical spool valve (b) Rim spool valve

Figure 1.1: Standard and rim spool valve configuration

Chan et. al.(6, 7 and 8) identified friction and flow forces as the major contribution to the flow division error. The new rimmed valve was able to significantly reduce the flow dividing error and the design has been implemented in some commercial flow divider valves. Chan et al.(6, 7 and 8), suggest that the reason for the reduction was that the surface area that the pressure gradient (across the surface of the spool lands) acted on was quite small so that the angle of discharge approached 90 degrees. This conjecture has not been proven other than by indirect methods (such as the observed reduction in flow dividing error in the valve with the rim). To this point, no further studies, have addressed this problem, which is one of the motivations for the present research.

1.2 Physical Representation of Flow Reaction Forces

Before proceeding, it is of some benefit to describe how steady state flow reaction forces occur in a valve. In the operation of a valve, the fluid entering and leaving the valve chamber can have different momentum in each coordinate direction. This produces reaction forces on the spool in both the lateral and axial directions. The net lateral forces acting on the spool can in general be eliminated by locating the ports symmetrically

around the circumference of the sleeve (1). However, the axial forces are significant and contribute to the steady flow forces on the spool. Thus, the external force needed to stroke the valve has to counteract the axial forces acting on the spool.

The axial forces include the inertial forces, the frictional forces and the forces resulting from the fact that fluid is flowing in and out of the valve and exerting force on the spool. These forces are known as flow reaction forces or Bernoulli's forces or simply flow force (1). The inertial forces and the frictional forces are generally small for a properly designed valve. The flow forces are dominant and have to be estimated.

The development of flow forces can be best understood based on an explanation such as that presented by Blackburn (26). Consider Figure 1.2 which represents one metering orifice of a spool valve. Upstream of the orifice is the valve chamber and downstream is the port usually connected to an actuator. The cross – sectional area for the flow at the orifice is much smaller than it is anywhere else in the chamber. Hence, the velocity is a maximum near the orifice. According to Bernoulli's principle, this region of high velocity is also a region of low pressure. This reduction in pressure is indicated by the pressure profile on face B in Figure 1.2.

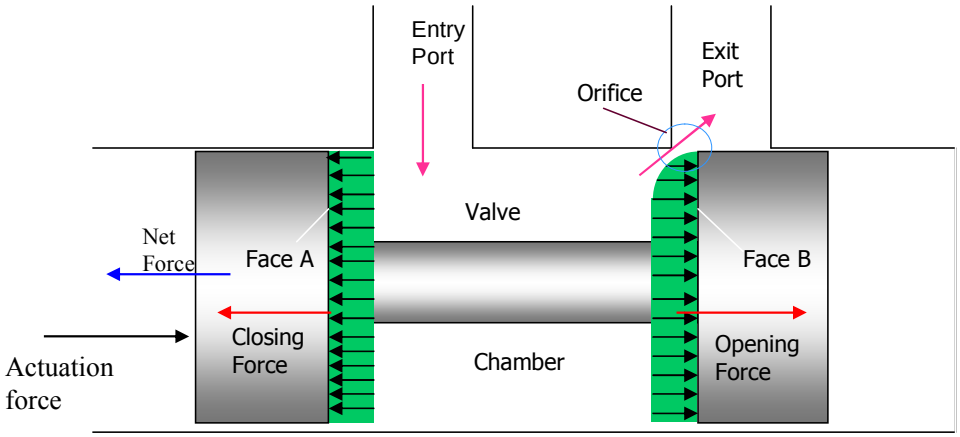

Figure 1.2: Pressure distribution on the land of a spool valve

The force on the left land (piston) face, (face B) is approximately proportional to the area under the pressure curve, and this force tends to open the valve. The pressure against the right land (piston) face, (face A) is approximately independent of position because the adjacent fluid is moving slowly. The pressure curve is therefore approximated by a rectangle. The force on Face A tends to close the valve. The area it encloses is greater than that enclosed by the first curve. Therefore, the closing force is greater than the opening force, and the net force tends to close the valve. This net force is referred to as the steady state flow force (SSFF). The steady state flow reaction force always acts in a direction so as to close the valve independent of the flow direction.

1.3 Background and Literature Review

A number of studies have been done to compensate for flow forces. Several of these studies have been discussed in the last section. The classical method of determining the magnitude of flow forces has been based on a Lumped Parameter (LP) approach. Merritt (1) used the LP approach to derive an expression for calculating flow forces as a function of the spool orifice opening, pressure drop across the valve, and angle of discharge. He also prescribed methods that can be used to reduce and compensate for flow forces as discussed in the introduction.

Pertinent to this research, Chan et al. (6) and Burton et al. (7 and 8) used a spool with a rim machined into the lands to reduce the flow division error in a flow divider valve (Figure 1.3). A flow divider valve is used to divide flow into two or more portions at a pre-determined ratio irrespective of the operating load pressure. The quality of a flow divider valve is determined by its flow division error. Chan (6) identified friction and flow forces as contributions to this flow division error. They proposed machining a rim into the lands of the spool as shown schematically in Figure 1.3. They surmised that within the cavity created by the rim, the velocity of flow would be very low (almost stagnant) and as such a static pressure would exist in this region. The total pressure on the face of the valve land to the right was now comparable to that of the left.

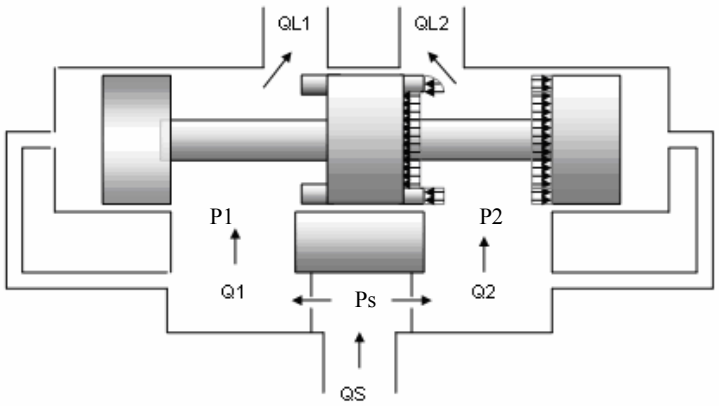

Figure 1.3: A flow divider valve

For this configuration, it was conjectured that the pressure gradient across the orifice only acted on the small rim and not the complete area of the land. The closing and opening forces thus tended to become more equal. The valve was tested experimentally and the addition of the rim was found to reduce the flow division error significantly. Since Chan (6) surmised that friction and flow forces were the major contributor to the flow division error, any reduction was primarily a consequence of reduced flow forces; thus they concluded that the rimmed configuration did contribute to this reduction. The authors were not able to directly measure flow forces on the particular spool arrangement that was used in their study. Thus, their conclusions were based solely on indirect information such as the observed reduction in flow dividing error in the valve using the rim.

The challenge of verifying that flow reactions forces were indeed reduced was part of the motivation for this research. In addition, since Chan (6) had demonstrated the difficulties in experimentally verifying their claim, it was decided that another approach using Computational Fluid Dynamics (CFD) could be a viable alternative to address the problem.

In the past decade significant advances to CFD and Particle Image Velocimetry (PIV) approaches have been made and applied to numerous fluid dynamics problems and more recently, hydraulic components. Wang et al. (9) used PIV to acquire data in a simplified

valve geometry. They measured the velocity field in a spool valve based on two-dimensional PIV. Their results showed PIV to be an effective method to measure velocity field in a spool valve. Similarly, Gao (10) investigated the flow structure inside a spool valve by numerical simulation based on the Finite Element Method (FEM) and tried to validate his results with PIV experiments. Both visualization results indicated a similar flow structure, but the specific data acquired from both methods did not agree well.

Borghi et al. (2) showed how the flow characteristics of a complex geometry can be dramatically simplified using axi-symmetric approaches. This allowed for a reduction in the time needed to solve the governing equations. Bao (3) investigated the flow behavior inside a hydraulic spool valve using CFD methods. He analyzed the relationship between flow rate, geometry and pressure losses by comparing the computed pressure loss for different flow rate and chamber structures. His results show that the changes in flow rate and in geometry decreased the pressure drop significantly in the valve, but modifications to the valve's spool geometry resulted in little improvement. Linda et al. (11) used CFD as a tool to improve a valve design. With CFD, the authors predicted the primary source of pressure losses in the existing valve and then modified the valve features to minimize those losses. Vescovo and Lipolis (12, 13) provided a detailed study of flow forces in traditional and proportional directional valves using a commercial CFD code. In particular, a complete three dimensional analysis of both types of valves was demonstrated and the dependence of flow forces on pressure drop and on the spool opening were analyzed.

Another school of thought proposed using flow forces advantageously instead of eliminating them. Yuan et al. (14 and 15) used fundamental momentum analysis, CFD analysis and experimental studies to examine how transient and steady flow forces can be manipulated to improve spool agility (dynamic response) in a single stage valve. They proposed that spool agility can be improved by inducing unstable transient flow forces, that is, by configuring the valve to have a negative damping length, and the unstable valves could be stabilized via closed-loop feedback. The idea is similar to the design of high-performance fighter airplanes in which the aerodynamics is sometimes designed to

be open-loop unstable so as to enhance their agility. Also in this work, it was found that two previously ignored components, i.e. viscosity effects and non–orifice momentum fluxes, have a strong influence on steady flow forces.

Based on the success that these researchers (and many others) have had in using CFD to analyze flow forces and to assist in flow visualization in valves and other hydraulic components, it was decided to use CFD as a means of establishing that the rim effect of Chan's design was indeed able to reduce the flow reaction forces. The rim effect was most interesting in that the fabrication was very straight forward compared to the valve contouring that alternate approaches used.

1.4 Lumped Parameter (LP) and CFD Approach

As identified in the literature review, numerous studies have used the LP and CFD methods to address fluid power problems. In the LP approach, the description of the fluid dynamics is based on applying the momentum equations to the fluid inside the control volume (valve chamber) and assuming that the fluid properties (pressure, velocities) are uniform over a cross section within the control volume. This approach is at best an approximation as the fluid properties are not constant over a cross section and the flow geometry is usually complex. In spite of this shortcoming, the LP approach has been the primary analytical tool used by engineers in most valve designs. However, as the demand for better valve performance increases, so must be the sophistication of the analytical tools.

An alternative analytical tool that is gaining widespread application in the area of fluid power (as indeed, many other areas) is Computational Fluid Dynamics (CFD). The CFD technique obtains numerical solutions to the Navier-Stokes equations that govern fluid flow. It does this by applying the governing Navier-Stokes equations to small elemental volumes within which the variation of the flow parameters is assumed to be linear. Apart from providing visualization of the flow field, CFD simulations can also give the pressure distribution and velocity field even for complex geometries. The analytical LP approach

can be used for relatively simple models, but CFD techniques enable researchers to obtain simulation results for more realistic models.

According to Finke et al., (5), in the past CFD has had limited use in fluid power applications because the calculations would quickly become extremely too large. Hydraulic problems tend not to be axi-symmetric and therefore require a large number of computing nodes and perhaps dozens of hours of computing time. A typical hydraulic valve problem could take 40 hours to run. The advent of high-speed computers has enabled CFD to provide solutions to many flow problems including fluid power applications. It was believed that applying CFD to the flow reaction force – rim configuration of a spool might be an appropriate method to verify the claims of Chan et al. (6).

1.5 Research Objectives

It is well known that flow forces exist in valves and can have a significant impact upon the metering accuracy of the valve. These forces are non-linear and lead to a degradation in controllability, accuracy, and stability. A rim in the spool has been proposed by Chan (6), which would be an inexpensive way to reduce the effects of the flow reactions forces. However, the actual concept has never been adequately explained.

The overall objective of the research in this area was to better understand the actual physics of flow reactions force that exist on spool valves. A specific objective of this research project was to study the flow reactions forces on the rimmed spool proposed by Chan (6) using CFD analysis. At this stage, no experimental work will be conducted.

1.6 Thesis Overview

This thesis is divided into six chapters. Chapter 1 provides a general introduction to the study, including a review of previous literature, the development of flow forces and a

statement of the objectives of the thesis. The LP and CFD approaches for determining flow forces are also discussed. In Chapter 2, the basic operation of a valve is discussed. The LP (otherwise known as the control volume analysis) models for steady flow forces and the CFD analysis for incompressible viscous flow are presented. Chapter 3 presents the CFD solution process using commercial numerical software, CFX 5.6. The steps in using a commercial CFD code (i.e. CFX-5.6) will be demonstrated by doing a similar study of the valve that was used by Gao (10). In Chapter 4, the simulation results shall be presented for the steady flow forces for typical and compensated valve geometry. The simulation results will also be compared to the results obtained from the classical equations for estimating flow forces which was based on the LP approach. In Chapter 5, the CFD method is applied to the rimmed flow divider valve of Chan et. al. (6). Chapter 6 gives a summary and the conclusions of the study, and also indicates some meaningful direction for future research.

Chapter 2

Basic Valve Operation and Models for Steady Flow Forces in a Spool Valve

In hydraulic spool valve design, a major problem is to determine the forces acting on the spool which the spool actuation device (such as solenoid actuator) must overcome. As reported in Chapter 1, the dominant force on the spool is the steady state flow force, which is a consequence of a change in fluid momentum within the valve. These forces are generally quite substantial when a large amount of flow is passing through the valve. Often, the size of the flow forces are so large that it prohibits the direct actuation of the spool using standard solenoid technology.

The focus of this chapter, is to give a brief overview of the basic components and operation of a hydraulic spool valve, and to present models for steady state flow forces using the Lumped Parameter (LP) approach. This approach is also known as the control volume analysis. This chapter shall also provide the mathematical framework which describes the flow through the valve. The flow shall be considered to be steady, two-dimensional (2D), incompressible and turbulent; in addition, the fluid is assumed to be viscous with constant density and viscosity. Because the flow is assumed to be steady, dynamic changes in flow and hence transient flow forces are not considered. The finite volume method, which is the discretization technique employed by the CFX 5.6 code used to solve the fluid problem, shall also be discussed.

2.1 Basic Components and Operation of a Hydraulic Spool Valve

Figure 2.1 shows the basic components of a spool valve that is typically used to control the direction of fluid flow in a hydraulic circuit.

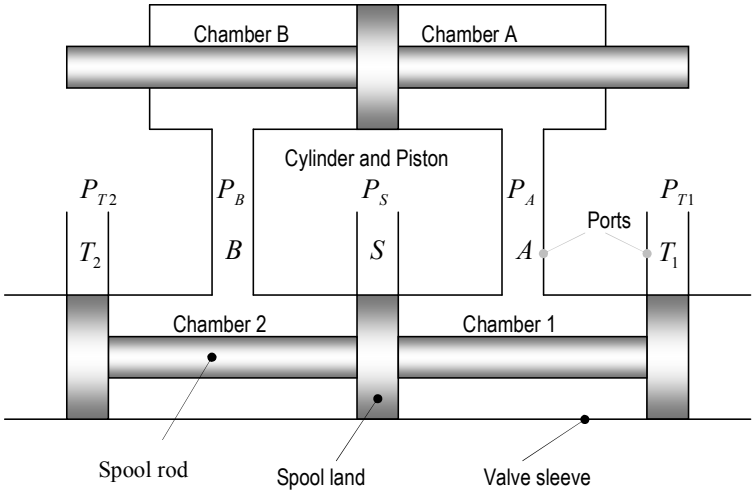

Figure 2.1: Schematic of a spool valve (critically centered i.e. $x_v = 0$)

Consider Figure 2.1. The valve is made up of two parts, the body (sleeve) containing the ports, and the spool or sliding element, which consists of the lands and the rod. The spool has multiple lands, and the relative motion between the lands and port openings in the sleeve can be used to modulate the flow. Each valve chamber (1 and 2) is partitioned by two lands. The movement of the spool causes each land to vary the area of the corresponding ports exposed to the flow. The variable orifice thus created is the basic element for modulating flow (or in some instances, pressure) to hydraulic systems.

The valve can be stroked hydraulically (via a pilot stage valve) or directly by an electromagnetic device, such as a torque motor or a solenoid. However, these direct actuation components often have distinct force and power limitations. It is important to understand the nature of and to estimate the magnitude of, steady state flow forces on the spool in order to choose the most appropriate driving mechanism.

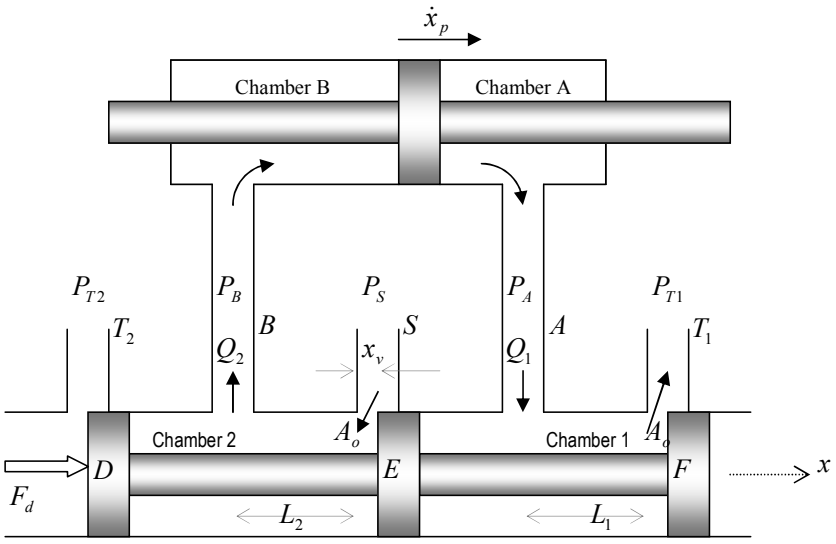

Figure 2.2: Operation of a spool valve (spool displaced to the right, i.e. $x_v > 0$)

The valve model used in the following analysis is the critical centered valve, where the spool lands perfectly match the valve ports as shown in Figure 2.1. The valve in Figure 2.2 shows the spool actuated to the right creating two orifices at lands B and C. With reference to Figure 2.2, there are two chambers (1 and 2), three lands (D, E and F), a supply port S (from the pump), two control ports A and B (to/from the cylinder) and two return ports T_1 and T_2 , that exit to a tank. The arrows show the direction of flow.

The operation of the valve is as follows. In Figure 2.1, the spool is centered in position where the actual displacement of the spool, $x_v = 0$. The spool lands are aligned with ports T_1, S and T_2, so that there is no flow. As the spool is displaced (i.e. towards the right or left), the ports on the sleeve open to supply port S, and return port T_1. Figure 2.2 shows the case where the spool valve is forced to the right by the driving (actuation) force F_d which must be capable of overcoming the forces acting on the spool. When the spool is displaced in the positive (negative) x- direction, the hydraulic oil is ported from the

supply S to port B (A) on one side, and from port A (B) into the tank T_1 (T_2) on the other side, creating flows Q_1 and Q_2, respectively.

The actual displacement of the spool which causes the flow restriction is usually so small relative to the port diameter that the pressure/flow relationships obey Bernoulli's equation (1). Thus, the classical orifice equation can be applied:

$$Q_1 = C_D w(-x_v)\sqrt{2/\rho}\sqrt{P_S - P_A} \qquad x_v < 0 \qquad (2.1)$$

$$Q_2 = C_D w x_v \sqrt{2/\rho}\sqrt{P_S - P_B} \qquad x_v > 0. \qquad (2.2)$$

In the example shown in Figure 2.2, the hydraulic actuator (cylinder) is a double acting cylinder (moves hydraulically in both directions) and it is connected to the valve by ports A and B. The piston motion of the cylinder is controlled by regulating the oil flow rates Q_1 and Q_2 into and out of the cylinder chambers (A and B) by the valve.

2.2 Steady State Flow Forces (SSFF) Equations

The focus of this section is to present models for the Steady State Flow Force (SSFF). The SSFF is the net force due to pressure acting on the faces of the spool lands. It could also be described as the effect of fluid momentum as fluid moves in and out of the valve. The Total Steady State Force (TSSFF) that includes the SSFF component and the viscous force acting on the sleeve or rod surface was studied by Yuan and Li, (14 and 15). Yuan expressed the momentum flux at the inlet to be proportional to the square of the flow rate, and used the assumption of laminar flow and a Newtonian fluid to model the shearing forces that act on the spool rod and valve sleeve. In this thesis, however, the SSFF component and the viscous contribution to the total steady state flow forces are considered.

2.2.1 Lumped Parameter (LP) Model

Merritt (1) provides the classical treatment for flow reaction forces using the LP approach. The valve configuration and nomenclature are given in Figure 2.3. The development of the classical model of flow reaction forces for inflow and outflow conditions is presented in Appendix A. Applying appropriate assumptions (1), and using the nomenclature of Figure 2.3, it can be shown from conservation of momentum that:

$$\vec{F}_{spool} = \iint_{A(RightFace)} PdA - \iint_{A(LeftFace)} PdA + \eta \iint_{A(Rod)} \tau_{rod}\, dA \tag{2.3}$$

which can be expressed as

$$\vec{F}_{spool} = -\left(2C_D A_o \Delta P \cos\theta \pm \eta \iint_{A(Rod)} \mu \frac{\partial V_x}{\partial y} dA \right) \tag{2.4}$$

where C_D is the discharge coefficient; A_o is the orifice area; ΔP is the pressure drop across the valve; θ is the jet efflux angle; μ is the fluid viscosity; $\partial V_x / \partial y$ is the velocity gradient in the y – direction evaluated at the rod wall; dA is the differential area and η is a switching function. When viscous effects are neglected, η = 0, Merritt (1); if they are included, then η = 1, as done in Yuan and Li (14 and 15). For the outflow condition, the viscosity contribution is an addition to the total steady state flow forces whereas for inflow condition, the viscosity contribution reduces the total steady state flow forces.

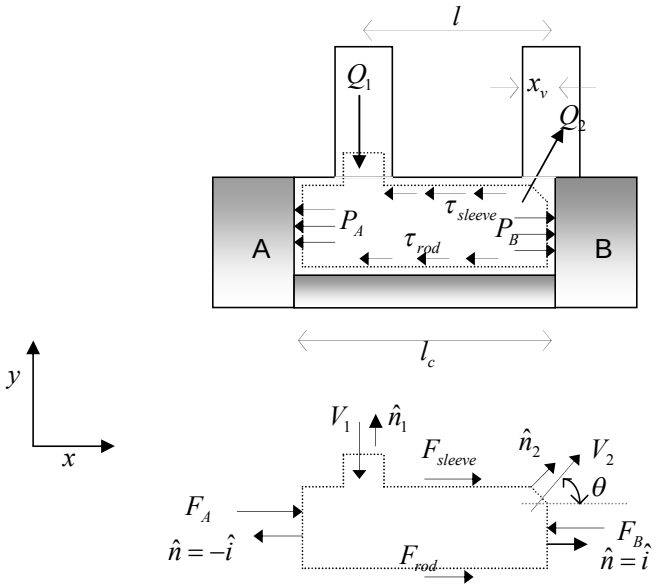

Figure 2.3: Control volume and nomenclature for the valve studied

2.2.2 Differential Model

An introduction to the 2D incompressible Navier – Stokes equations is provided in Section 1 of Appendix C. In stating the flow equations, the following assumptions are adopted;

- Flow is 2D, steady, incompressible and turbulent
- Fluid is Newtonian with constant density and viscosity

The basic equations that govern the flow are the time-averaged conservation equations for mass and momentum. For compactness, Cartesian tensor notation shall be used. For steady, incompressible flow, the Reynolds averaged Navier – Stokes (RANS) equations are,

$$\frac{\partial \overline{U}_j}{\partial x_j} = 0 \qquad (2.5)$$

$$\underbrace{\frac{\partial}{\partial x_j}\left(\rho\overline{U_i U_j}\right)}_{convection} = -\underbrace{\frac{\partial \overline{P}}{\partial x_i}}_{pressure\,gradient} + \underbrace{\frac{\partial}{\partial x_j}\left(\mu\frac{\partial U_i}{\partial x_j}\right)}_{viscous\,diffusion} - \underbrace{\frac{\partial}{\partial x_j}\left(\rho\overline{u_i' u_j'}\right)}_{\text{Re}\,ynolds\,stress} \qquad (2.6)$$

In equations (2.5 and 2.6), repeated indices imply summation; for 2D, i = 1, 2; ρ is the density; μ is the dynamic viscosity; $\overline{U}_i$ is the mean Cartesian velocity component; u_i' is the fluctuating Cartesian velocity component; $\overline{P}$ is the mean pressure; and x_i is spatial coordinate.

Equation (2.6) represents a momentum balance in which the left side of the equation is the acceleration of the fluid, while the terms on the right represent the net force consisting of the pressure force, the frictional force due to viscosity, and the turbulent or Reynolds stress. Equation (2.6) is not closed because of the Reynolds stress tensor, $\rho\overline{u_i' u_j'}$ which results from the averaging procedure. The Reynolds stress tensor represents an effective fluid stress due to turbulence, and is dominant in most of the flow.

In order to close the RANS equations, a turbulence model must be implemented for the Reynolds stress tensor. One of the most popular turbulence models for engineering calculations is the eddy viscosity model, which relates the turbulent stress to the mean strain rate as follows:

$$\rho\overline{u_i' u_j'} = -\mu_t\left(\frac{\partial \overline{U}_i}{\partial x_j} + \frac{\partial \overline{U}_j}{\partial x_i}\right) + \frac{2}{3}\rho k\delta_{ij} \qquad (2.7)$$

where μ_t is the turbulent viscosity, k is the turbulence kinetic energy and δ_{ij} is the Kronecker delta. The quantity $k = (1/2)\overline{u_i' u'}$ is the turbulence kinetic energy associated with the fluctuations of the velocity field. Note that unlike the dynamic viscosity, the turbulent viscosity is not a fluid property but a function of the local flow field. In this

case, it is evaluated using the Shear Stress Transport (SST) turbulence model available in the code CFX-5.6.

The local value of μ_t is calculated using the following relation:

$$\mu_t = \frac{\rho a_1 k}{\max(a_1 \omega \Omega)} \tag{2.8}$$

whereas before, k is the turbulence kinetic energy, ω is the inverse of the turbulence time scale, a_1 is a constant, and Ω is the absolute value of the vorticity. In order to calculate μ_t, two additional transport equations are solved for k and ω. The specific form of the transport equations is described in the documentation for CFX-5.6, and their derivation is given in Menter (16). One important aspect of this two-equation closure is that it is a low Reynolds number formulation that remains valid in the immediate vicinity of the wall, where typically the turbulence is strongly damped and viscous forces are dominant. The SST model requires a sufficiently fine grid near the wall, but when correctly implemented can accurately resolve the local wall shear stress, τ_w, which can then be used to calculate the viscous friction force acting on the surface. The flow forces are evaluated by integrating the pressure profiles over the surfaces of the two lands, and integrating the shear stresses over the rod and piston faces. For complex geometries, this set of equations can only be solved numerically.

2.2.2.1 Near Wall Treatment

An important consideration in the accurate prediction of turbulence is the formulation and numerical treatment of the equations in the regions close to solid walls. As already stated, the SST model together with a fine-grid in the near-wall region will be used. The model is a hybrid of two two - equation turbulence models, namely the k – ε and the k – ω models. The SST model combines the best elements of both models with the help of a

blending function F_1. Far from wall the blending function F_1 is set to 1 yielding the k – ε model and set to 0 near the wall yielding the k – ω model.

2.2.2.2 Discretization

In order to solve the non-linear, continuous, partial differential Navier – Stokes (or RANS) equations, the equations must first be discretized. The method of approximating these non-linear, partial differential equations (i.e. equation 2.6) by a system of algebraic equations for the variables *u, v* and *p*, at a set of discrete locations in space and time is called discretization. The discrete spatial locations are defined by the grid or mesh. For this study, at each node of the mesh, three primary variables are to be solved: the pressure and two velocity components. In addition, turbulence quantities such as *k* and ω are also solved.

As part of the discretization process, the variables located at the face (to be shown later) must be related to the nodal values. This process involves numerical approximation. All numerical approximation schemes introduce some degree of error. This error can be reduced by using an appropriate differencing scheme.

In CFD, three well-known discretization techniques are: the Finite Difference Method (FDM), Finite Element Method (FEM) and Finite Volume Method (FVM). Since the CFD code (CFX 5.6), which was used in this study, employs the FVM, only the finite volume approach shall be discussed.

2.2.2.3 Finite Volume Method (FVM)

The Finite Volume Method **(**FVM) involves integrating the governing equations over a control volume to obtain the discrete equations. The integration of the governing equations ensures that the expressions for the dependent variables are conservative. A representative grid structure used by the FVM is shown in Figure 2.4. In the FVM, each node is located at the centre of a finite control volume, which is bounded by a set of surfaces.

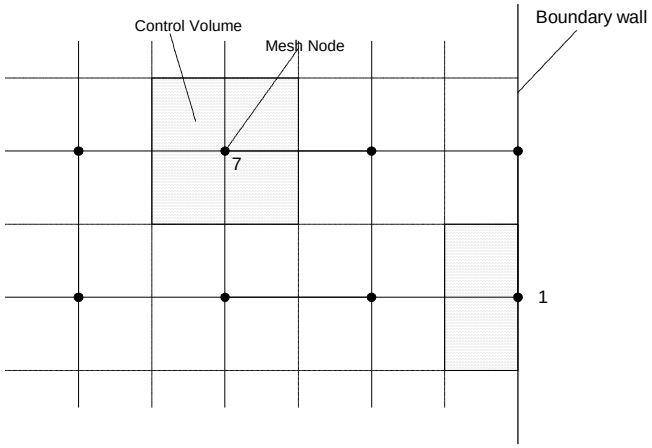

Figure 2.4: Finite volume grid structure

For example, the velocity value calculated at a mesh node (i.e. node 7 in Figure 2.4) is based upon the 'average' value of the velocity over the control volume surrounding that node. For calculation purposes, the entire control volume is then assumed to possess that velocity. At a boundary node (i.e. node 1), the control volume consists of an area in the bulk of the fluid which is highlighted in Figure 2.4. Hence, the conservative velocity calculated at the wall is not zero, but an average over the control volume. For a no-slip boundary condition (i.e. $u = 0$), the CFX 5.6 code uses a "hybrid" value. Hybrid values are obtained by taking the results produced by the CFX -5 Solver and "over – writing" the results on the boundary nodes with the specified boundary conditions. This will ensure that the velocity is displayed as zero on no-slip walls.

2.2.2.4 The SIMPLE Algorithm

The SIMPLE (Semi – Implicit Method for Pressure Linked Equations) algorithm was used to solve the pressure field. This algorithm was originally derived by Patankar (22) and also appears in Ferziger and Peric (24).

2.2.2.4.1 Discrete Transport Equations

The momentum equation is discretized on the "staggered" grid shown in Figure 2.5 as was first proposed by Harlow and Welch (23). On a staggered grid, the velocity components are evaluated at the faces while the pressure or scalar variables are evaluated at the nodes. Referring to Figure 2.5, node *P* is located at the centre of the cell and nodes *E, W, S*, and *N* are located at the centre of the neighboring cells; *e*, *w*, *s* and *n* are the associated faces of nodes *E*, *W*, *S* and *N*. Nodes *EE, WW, NN* and *SS* are the neighboring nodes of *E, W, N* and *S*.

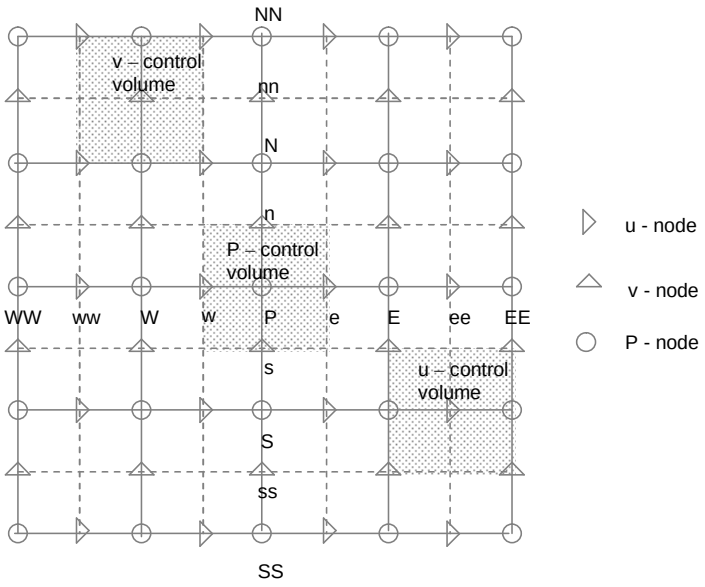

Figure 2.5: A staggered grid structure. Capital letters refer to the cell node; lower case letters refer to the cell face

For the *u* - control volume of Figure 2.5, integration of the partial differential equation over the control volume yields an algebraic equation written as follows,

$$a_e u_e = \sum a_{nb} u_{nb} + A_e \left(P_P - P_E \right) \qquad (2.9)$$

where a_e is the discrete variable to be evaluated at the cell face e; a_{nb} indicates the neighboring discrete coefficients a_w, a_{ee}, a_{se} and a_{ne} at the cell faces in 2D of a_e ; u_e is the velocity evaluated at the cell face *e*; u_{nb} are the neighboring velocities u_w, u_{ee}, u_{se} and u_{ne} evaluated on cell faces *w, ee, ne* and *se*, respectively; P_P and P_E are the pressures evaluated at node *P* and *E*, and A_e is the cell face area of the *u* - control volume. The volume of the control volume is given as $\Delta x \Delta y \Delta z$. For 2D flow, the *z*-dimension is assumed to be unity (1 unit), so that $A_e = \Delta y \times 1$. Hence the term $A_e\left(P_P - P_E\right)$ is the pressure force acting on the *u* – control volume. The meaning of the coefficients is illustrated in Appendix C for a 1-D convection-diffusion problem.

Similarly, for the *v* – control volume, the discretized momentum equation can be written for the *y* – direction as,

$$a_n v_n = \sum a_{nb} v_{nb} + A_n\left(P_P - P_N\right) \tag{2.10}$$

2.2.2.4.2 The Pressure Equation

In general, a solution for both the velocity and pressure fields is required. For incompressible flow, it is assumed that the correct pressure field is that which ensures that the velocity field conserves mass. This is the solution strategy of the SIMPLE algorithm. The SIMPLE algorithm begins by using a "guessed" value for the pressure P^*, to solve the momentum equation. The resulting velocities denoted by u^* and v^* will not satisfy the continuity equation. Based on the previous (*) value of the velocity and pressure fields, the momentum equations can be written as follows,

$$a_e u_e^* = \sum a_{nb} u_{nb}^* + A_e\left(P_P^* - P_E^*\right) \tag{2.11}$$

$$a_n v_n^* = \sum a_{nb} v_{nb}^* + A_n\left(P_P^* - P_N^*\right) \ . \tag{2.12}$$

The SIMPLE algorithm seeks to find corrections to the pressure field such that the resulting velocity field will better satisfy the continuity equation. If the correct pressure field is defined as P and the pressure correction is defined as P', then,

$$P = P^* + P' \tag{2.13}$$

In a similar fashion, the velocity corrections are written as,

$$u = u^* + u', \qquad v = v^* + v' \tag{2.14 a, b}$$

Subtracting equation (2.11) from equation (2.9), yields,

$$a_e u'_e = \sum a_{nb} u'_{nb} + A_e \left(P'_P - P'_E\right) \tag{2.15}$$

The unknown term $\sum a_{nb} u'_{nb}$ of equation (2.15) is dropped at this point to simplify the equations. The omission of this term is the main approximation adopted by the SIMPLE algorithm. It allows a coupling between the velocity and pressure correction fields that enables the continuity equation to be solved for the pressure correction field.
Hence,

$$a_e u'_e = A_e \left(P'_P - P'_E\right) \tag{2.16}$$

or,

$$u'_e = D_e \left(P'_P - P'_E\right) \tag{2.17}$$

where $D_e = \dfrac{A_e}{a_e}$ (2.18)

Equation (2.17) defines the velocity correction. Substituting equation (2.17) into equation (2.14), yields,

$$u_e = u_e^* + D_e\left(P_P' - P_E'\right) \tag{2.19}$$

In a similar fashion,

$$v_n = v_n^* + D_n\left(P_P' - P_N'\right) \tag{2.20}$$

Equations (2.19 and 2.20) can be substituted into the discretized continuity equation to obtain an equation for the pressure correction field.

Recall the steady state continuity equation:

$$\frac{\partial}{\partial x}(\rho u) + \frac{\partial}{\partial y}(\rho v) = 0\,. \tag{2.21}$$

Integrating the continuity equation over the P – control volume results in the following mass balance for the control volume,

$$\dot{m}_w - \dot{m}_e + \dot{m}_n - \dot{m}_s = 0 \tag{2.22}$$

where $\dot{m}_w, \dot{m}_e, \dot{m}_n$ and $\dot{m}_n$ are the mass flow rates at cell faces *w, e, n* and *s*, respectively, and are given as,

$$\dot{m}_w = (\rho u)_w \Delta y \tag{2.23}$$

$$\dot{m}_e = (\rho u)_e \Delta y \tag{2.24}$$

$$\dot{m}_n = (\rho u)_n \Delta x \tag{2.25}$$

$$\dot{m}_s = (\rho u)_s \Delta x \tag{2.26}$$

Substituting equations (2.23) - (2.26) into equation (2.22), and using equations (2.19) and (2.20) to express the velocity in terms of the old and correction fields, a discretized equation for the pressure correction field is obtained as follows:

$$a_P P'_P = a_E P'_P + a_W P'_W + a_N P'_N + a_S P'_S + b \tag{2.27}$$

where $a_E = \rho_e D_e \Delta y \times 1$ (2.28)

$a_W = \rho_w D_w \Delta y \times 1$ (2.29)

$a_N = \rho_n D_n \Delta x \times 1$ (2.30)

$a_S = \rho_s D_s \Delta x \times 1$ (2.31)

$a_P = a_E + a_W + a_N + a_S$ (2.32)

$b = p_w u^*_w \Delta y - p_e u^*_e \Delta y + p_s v^*_s \Delta x - p_n v^*_n \Delta x$ (2.33)

The term b is the local mass residual which arises because the velocities do not satisfy the continuity equation. The closer *b* is to zero, the better the velocity field satisfies the continuity equation.

Once the pressure corrections are determined, the pressure and velocities can be updated, and the updated pressure is then used as the initial guess for the next iteration. This procedure is repeated until convergence is achieved.

2.2.2.4.3 Solution Procedure

A summary of the procedure is as follows:

1. Guess the velocity and pressure fields, u^*, v^* and P^*

2. Solve the momentum equations, i.e. equations (2.11) and (2.12), to obtain u^* and v^*
3. Solve the P' equation, i.e. equation (2.27)
4. Calculate P from equation (2.13) by adding P' to P^*
5. Calculate u and v from equations (2.19) and (2.20)
6. Solve the discretized equations for any other variables, e.g. turbulence quantities
7. Return to step 2 and repeat the procedure until a converged solution is obtained.

2.2.3 Boundary Conditions

The RANS equations require boundary conditions to obtain a solution to the equations. It is the boundary conditions that produce different solutions for a given geometry and set of physical models. For the computational domain shown in Figure 2.6, the aim is to define appropriate boundary conditions that neither over- nor under-specify the problem. One way to determine if the boundary conditions are well-posed is to ensure that the same configuration can be physically recreated in a laboratory. For the flow problem, the boundaries in CFX 5.6 are basically divided into four types: inlet, outlet, wall and symmetry. The boundaries are illustrated in Figure 2.6.

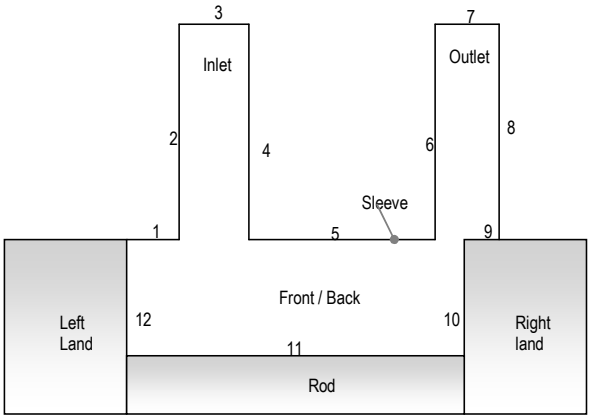

Figure 2.6: A schematic of the flow domain for a typical spool valve

In Figure 2.6, a label is used to identify each boundary. The spool surface is comprised of boundary 10, 11 and 12; the sleeve, 1 and 5; and the inlet and outlet 3 and 7, respectively. Because the model is actually 3D, the "front" and "back" surfaces in the z – direction, are separated by 1 mesh unit (1 control volume). The front and back boundaries cap the computational domain shown in Figure 2.6. Apart from the inlet (3), outlet (7), and the front and back, which are symmetry boundaries, all other surfaces are classified as no – slip boundaries. The no-slip boundary condition implies that the tangential velocity at each wall is zero due to friction. Furthermore, there is no velocity through the walls (no-penetration). The inlet and outlet are strictly one way flow boundary conditions. For the inlet, the flow is directed into the flow domain, while at an outlet boundary, it is directed out of the domain. The symmetry boundary conditions imply that there is no change in the flow variables in the normal direction.

2.2.4 Estimating Steady State Flow Forces (SSFF)

Based on either equation (A1.2) or (A1.6) of Appendix A, the steady state flow forces can be estimated from the pressure and velocity field provided by the CFD solution.

$$F_{spool} = \underbrace{\iint_{A(LeftFace)} PdA - \iint_{A(RightFace)} PdA}_{SSFF} \pm \eta \underbrace{\iint_{A(Rod))} \tau_{Rod} dA}_{Viscous} \tag{2.34}$$

where the first term on the *R.H.S* of equation (2.34) is the integrated pressure force acting on the left land surface; the second term is the integrated pressure force acting on the right land surface; and the last term is the viscous force acting on the rod surface.

In the code, the SSFF values are calculated using a method defined as "Pressure Integral", which is a built-in function of the CFX 5.6 software which integrates the pressure field over the nodes attached to the respective prescribed surface areas. The CFD program also outputs the viscous force which is calculated by integrating the wall shear stress over the surface area of the rod.

2.2.5 Summary

In this chapter, the basic components and operation of a spool valve were described. SSFF models were developed using the control volume analysis or lumped parameter approach. The total force on the spool was found to be a product of pressure drop, orifice opening and the angle at which the jet of fluid discharges at the variable orifice, plus the viscous force acting on the sleeve wall as given by equation (2.34).

Also in this chapter, the RANS equations governing the fluid flow were presented. A 2D finite volume solver based on the SIMPLE algorithm was described in order to provide a better understanding of the solution process.

Chapter 3

Development of Numerical Model Using CFX 5.6 Tool-kit

It is of interest when using any commercial software such as CFX 5.6 to apply the software to some appropriate benchmark for comparison purposes. For this study, an established benchmark was not available; however simulation and experimental results on the flow field inside a spool valve for various displacements of the spool were published by Gao (10). Gao used a numerical based Finite Element Method (FEM) and an experimental method using Particle Image Velocimetry (PIV) to study the flow fields. Because of the similarity of his valve flow to the one investigated in this thesis, Gao's study was adopted as a basis for comparison.

As will be discussed below, some boundary conditions in Gao's study had to be reformulated to accommodate CFX 5.6. It was recognized that changes to the actual boundary conditions made the two systems non- compatible for full comparison purposes. Gao's prediction is flawed in the outlet section as he implemented a fully - developed outflow boundary condition where it should not be, which then produces the erroneous results observed in his section profiles. However, it was believed that the trends predicted from Gao's work (particularly his PIV results) and this simulation could be compared; in addition, the structure of Gao's valve did facilitate an explanation of the procedure on how to use CFX 5.6.

3.1 Numerical Method

The objective of this section is to demonstrate the procedure for obtaining CFD solutions using the commercial numerical software CFX 5.6 (developed and distributed by ANSYS CFX (USA)), and will consider a similar type of valve geometry used by Gao (10). A second objective was to do a comparison study which investigates quantitatively the influence of the valve opening on the flow structure of a 2D valve geometry. Gao (10) used the Finite Element Method (FEM), which is a numerical formulation to discretize the continuity and Navier-Stokes equations. He developed his own simulation code to compute the velocity components in the flow domain. PIV techniques were then used to map the flow field inside the valve, and the experimental results were used to evaluate the numerical simulations.

The code used in this thesis, CFX 5.6, solves the system of algebraic equations obtained from a finite volume approximation of the governing system of partial differential equations. The discretization and solution algorithm follows the methodology of SIMPLE as discussed in section 2 of Chapter 2.

3.2 Definition of the Problem

The valve geometry modeled by Gao (10) is shown in Figure 3.1. This same structure was modeled in CFX 5.6.

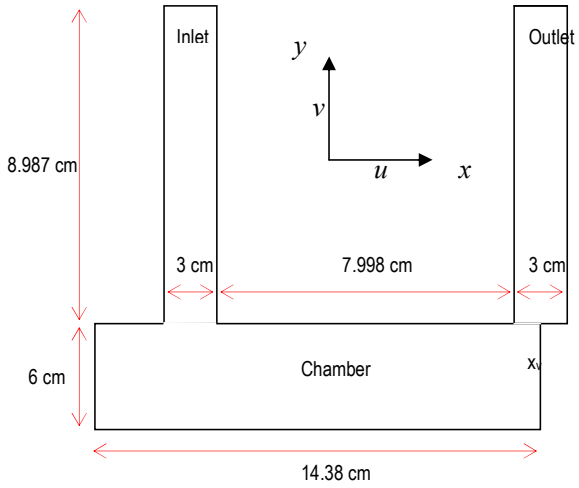

Figure 3.1: 2-D valve geometry

The dimensions of the valve are specified in Figure 3.1. The characteristic depth of the domain was defined by Gao to be 3 cm.

Since Gao used the stream – vorticity formulation, his boundary conditions were defined in terms of the stream - function φ and the vorticity ω. For this study, Gao's boundary conditions will be defined in terms of the velocities u and v. A summary of the boundary conditions and solution methodology for his study is as follows:

(i) The flow was taken to be incompressible, laminar, 2D, and steady; the fluid was water with constant density of 998 kg/m^3 and viscosity of 1 x 10^{-3} N.s/m^2.

(ii) The discretization of the governing equations was based on the Finite Element Method (FEM).

(iii) A parabolic velocity profile in the stream-wise (y) direction was specified at the inlet, i.e.

$$u = 0 \text{ m/s}, \qquad (3.1)$$

$$v = -0.4444\left(2.25 - x^2\right) \quad \text{(parabolic velocity profile)} \qquad (3.2)$$

(iv) At the outlet, the derivative of the velocity component in the y direction was set to zero. This condition implies that, at the outlet, u is set to zero and the derivatives of v in the y – direction are assumed to be zero;

(v) Simulations were conducted for spool openings of 0.375 cm, 0.75 cm and 1.125 cm.

(vi) The simulated results were compared to the measurements obtained using PIV for the spool opening of 0.375 cm.

For a similar valve structure as Gao (10), a simulation using CFX 5.6 was conducted. In order to achieve a fully developed flow at the outlet for the CFX 5.6 calculation, the outlet boundary was moved further downstream by 21 cm. In Gao's case, the fluid was forced (via the outflow boundary condition) to be fully developed within a short length from the metering section; this condition may be inconsistent with the physical nature of the flow. When an outlet is placed too close to a region of developing flow, erroneous recirculation patterns can occur upstream of the outlet boundary. Among other things, this could lead to convergence problems, since a portion of the outlet is "walled off" which prevents fluid from leaving the solution domain. For this reason, the outlet boundary was moved further downstream by extending the outlet duct. At this location, the flow was expected to leave smoothly without any recirculation. The flow geometry used in the CFX 5.6 simulations is represented in Figure 3.2. This slight modification was expected to affect the simulation results downstream of the exit orifice, which makes comparison with Gao's result in this region ambiguous.

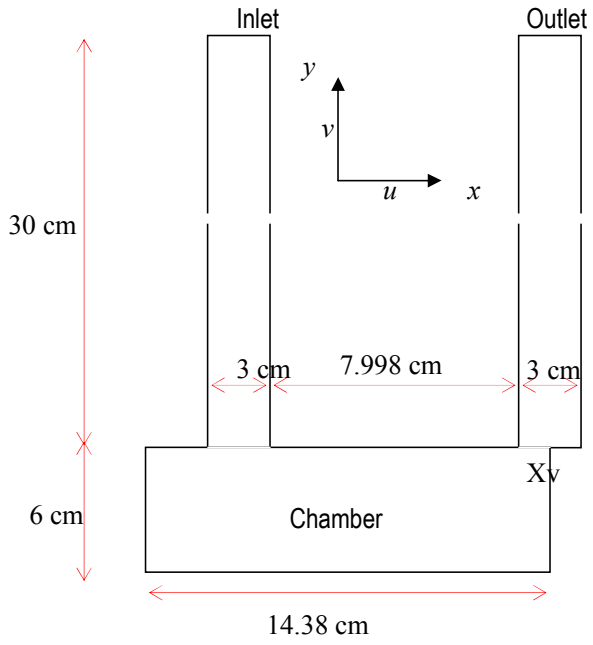

Figure 3.2: Geometry of the flow model used in CFX 5.6

3.3 Solution Procedure Using CFX 5.6

Generating CFD solutions using CFX 5.6 code involves 4 processes: CFX –Build, CFX-Pre, CFX-Solver and CFX-Post. This section will use Gao's problem to illustrate the basic approach. It should also be pointed out that the same steps were used to study the rimed spool and flow divider valve in the following chapters.

3.3.1 CFX-Build

This module is used to "build" the mesh. This aspect of the program allows for specification of the geometry and generation of the (numerical) mesh. It also allows for convenient specification of specific 2D and 3D regions. The 3D region defines the 3D computational volume of the solution domain, while the 2D regions (called patches) are

surfaces or planes where boundary conditions will be applied in CFX – Pre (the next module).

3.3.1.1 Specify Geometry

The creation of the flow geometry shown in Figure 3.2 is illustrated in Appendix D1 and will not be further discussed here. Only the meshing shall be discussed in detail.

3.3.1.2 Meshing

The fine grid for the simulation of the flow through the valve is show in Figure 3.3. Grids were created with 3 levels of refinement: coarse, medium and fine. Solving the flow on each of the 3 grids makes it possible to assess the sensitivity of the results to grid size, and allows one to extrapolate a grid independent solution.

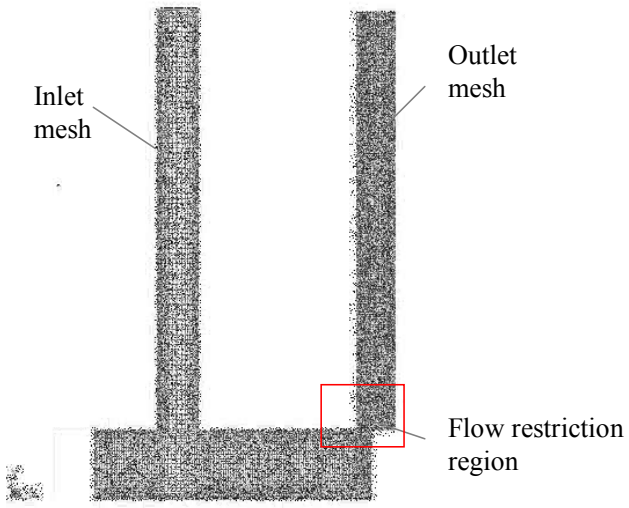

Figure 3.3: The rectangular grid (fine mesh) used for the simulation of flow through the valve

The mesh used was structured (i.e. the same mesh type was used throughout). The control volumes were hexahedral in shape, and fit the geometry of the flow problem (i.e. rectangular in 2D and hexahedral in 3D). The grid was constructed such that the size of a

grid cell, or control volume, did not change radically between neighbouring cells. Furthermore, near some walls and in the vicinity of the orifice, a finer mesh was used to ensure the sharp gradients of the field variables were adequately captured.

Near-wall typically refers to that region of a turbulent flow sufficiently close to a wall that the wall itself begins to influence the local flow structure, via both viscous drag and pressure blocking effects. In order to generate the mesh in CFX 5.6, "mesh seeds" were used to create the mesh density. (This is shown in step 6 of Section 1 of Appendix D1.) Each "seed" represented one control volume. The mesh seeds were applied to the bounding surfaces/curves of the flow domain. There are options to specify a uniform or non – uniform mesh seed (with either a 1-way or 2-way bias) along the surfaces/curves. The 2 -way bias concentrates control volumes at both ends of a curve, while the 1-way bias concentrates control volumes at one end of the curve. In this case, uniform 1-way and 2-way biased mesh seeds were implemented. For the non-uniform case, the mesh seeds were distributed using a geometrical progression for a specified ratio. Since CFX 5.6 is a 3D code, the model was actually 3D, and the "Front" and "Back" surfaces in the *z* – direction, were separated by 1 control volume. The mesh for the entry and exit ports is illustrated in Figures 3.4 and 3.5, respectively.

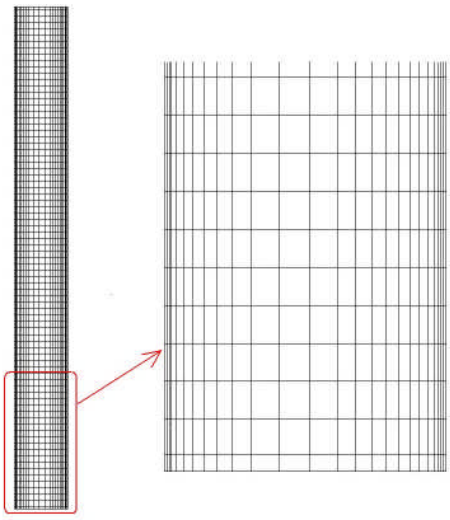

Figure 3.4: A section of the inlet mesh. A higher mesh density is used in the near-wall regions

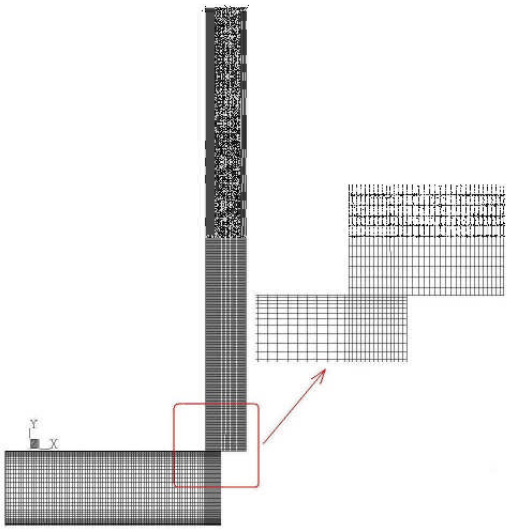

Figure 3.5: A section of the outlet mesh. A higher mesh density was used in the near-wall regions and for the metering section

The number of nodes used for Gao and CFX 5.6 simulations are summarized in Table 3.1.

Table 3.1: The number of nodes used for Gao and CFX 5.6 simulations

Spool openings (cm)	Number of nodes	
	Gao (FEM)	CFX 5.6
0.375	895	6804
0.75	894	6802
1.125	893	6842

3.3.2 CFX-Pre

This module is referred to as the pre-processor. The mesh created in CFX-Build is imported, and the boundary conditions and fluid properties are defined. This module also

enables specification of the transport equations and laminar/turbulent flow; sets the number of iterations to be carried out; defines the simulation mode (steady or transient); sets the physical timescale (a parameter that affects the convergence rate and the behaviour of the solver) and starts the solver mode. In this section, emphasis will be given to defining the boundary conditions. This CFX – Pre process is described in detail in Appendix D2.

3.3.2.1 Inlet Boundary

The inlet boundary profile of Gao (10) shown in Figure 3.6 was replicated in the simulation using CFX 5.6. The inlet to the rectangular valve geometry of Figure 3.2 can be considered as a channel flow, and the velocity profile for a fully developed channel flow, is given as,

$$V = V_{\max}\left(1-\left(\frac{x}{h}\right)^2\right) \tag{3.3}$$

where $2h$ is the axial width of the inlet port, $V_{\max}$ is the centerline velocity (1 cm/s), and V is the inlet velocity profile. The parabolic profile given by equation (3.2) can be defined in the CFX 5.6 code by using the CFX-5 .6 Expression Languages (CEL) (described in Appendix D2):

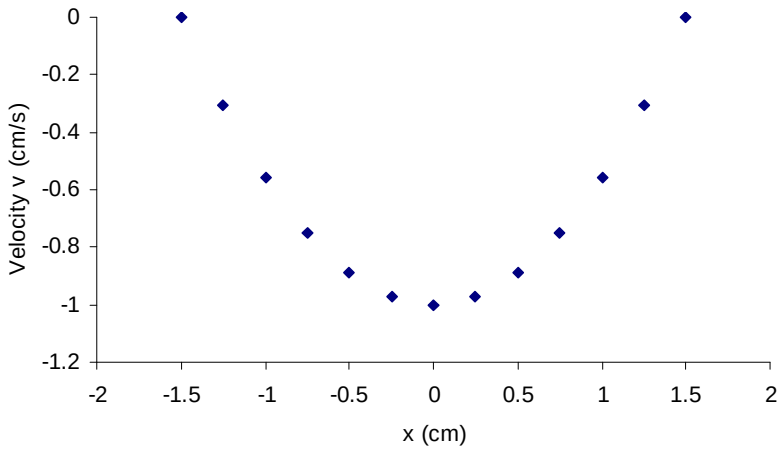

Figure 3.6: The inlet velocity profile (10) in *y*-direction

3.3.2.2 Outlet Boundary

In Gao (10), as stated earlier, the outlet boundary conditions were prescribed in terms of stream - function and vorticity. As mentioned in Section 3.2, the outlet condition pertains to a fully – developed flow. The outlet channel was extended by 21 cm such that the flow would be fully developed at the exit. Since CFX 5.6 does not enforce the stream - vorticity formulation at any outlet boundary condition, a static pressure was specified at the outlet. The combination of inlet velocity profile and outlet pressure boundaries is the most robust boundary condition of the CFX 5.6 code. An absolute pressure of 0 *Pa* was imposed at the outlet.

3.3.2.3 Wall Boundary

In defining the wall boundary conditions, it is assumed that the fluid velocity at the wall is the same as that of the wall (or zero relative velocity.) This is called a "no – slip" boundary condition, and accounts for the effect of the fluid viscosity.

3.3.2.4 Symmetry Boundary

The specification of symmetry boundaries becomes necessary because a 3D code is being used to solve the 2-D problem. To solve the 2D problem, the flow domain is given a thickness of one control volume in the third (z) direction, and symmetry boundaries are imposed on these surfaces.

3.3.3 CFX-Solver

In this module, no user input is required. The SIMPLE algorithm, which is the default in CFX 5.6, is used as the velocity – pressure correction procedure. The solver calculates the solution to the RANS equations at each computational volume using an iterative procedure. The convergence of the solution fields is checked to ensure that the residual values for the continuity and the two momentum equations become less than some specified value. As the solution progresses, the code outputs residual values to monitor the convergence process. The solver stops when the specified number of iterations is reached.

Convergence relates to the fact that the solution fields stop changing and the residual refers to the failure of the solution to exactly satisfy the discrete equation. Convergence of the iterative solutions is tested by comparing the values of u, v and p from successive iterations and ensuring that the maximum changes in u, v and p are sufficiently small. The residual criteria set for this problem required that the dimensionless maximum changes in Δu, Δv and Δp were less than 1×10^{-5}. The initial guess was the value that was set in the domain in CFX –Pre. Thus 1.0×10^{-5} implies 5 orders of decrease from the original residual (or error), which is based on the initial guess. The number of iterations required for convergence varied from 700 to 1200. More iterations were needed for the flow with the highest Reynolds numbers (for the smallest spool opening, x = 0.375 cm).

The effect of grid spacing was also investigated to ensure that the mesh generated was sufficiently fine to accurately model the problem. One way to ensure adequate near - wall resolution was by checking the value of y^+ (discussed in Section 2 of Appendix E) at the

end of each simulation. The quantity y^+ is a dimensionless wall distance that provides an indicator of the "effective proximity" of the first node to the wall. But since this was a laminar flow calculation, the concept of y^+ was not relevant for this application. The solution process was therefore completed when the solution showed that the values of velocities *u* and *v* of the previous and new simulations at the same 4 discrete locations within the solution domain were approximately the same. The new simulation used more control volumes than the previous ones.

3.3.4 CFX-Post

This module provides for easy visualization and post – processing of the CFD simulations. The flow field information is presented in terms of streamlines, contours, velocity vectors, line plots, etc. as specified by the user. The procedure for creating velocity vectors and contours plots are presented in section 3 of Appendix D.

3.4 Results and Discussions

Figure 3.7 provides detailed flow field information of the velocity field calculated using CFX 5.6 for a valve opening of 0.375 cm. In this example, only velocity profiles shall be presented as Gao (10) only presented results for the velocity field. In the figure, the stream of fluid exiting the flow restriction attaches to one wall of the outlet port, moves downstream as a wall-jet, and then detaches to form a recirculation zone. Downstream of the recirculation zone, the flow recovers toward a channel flow profile.

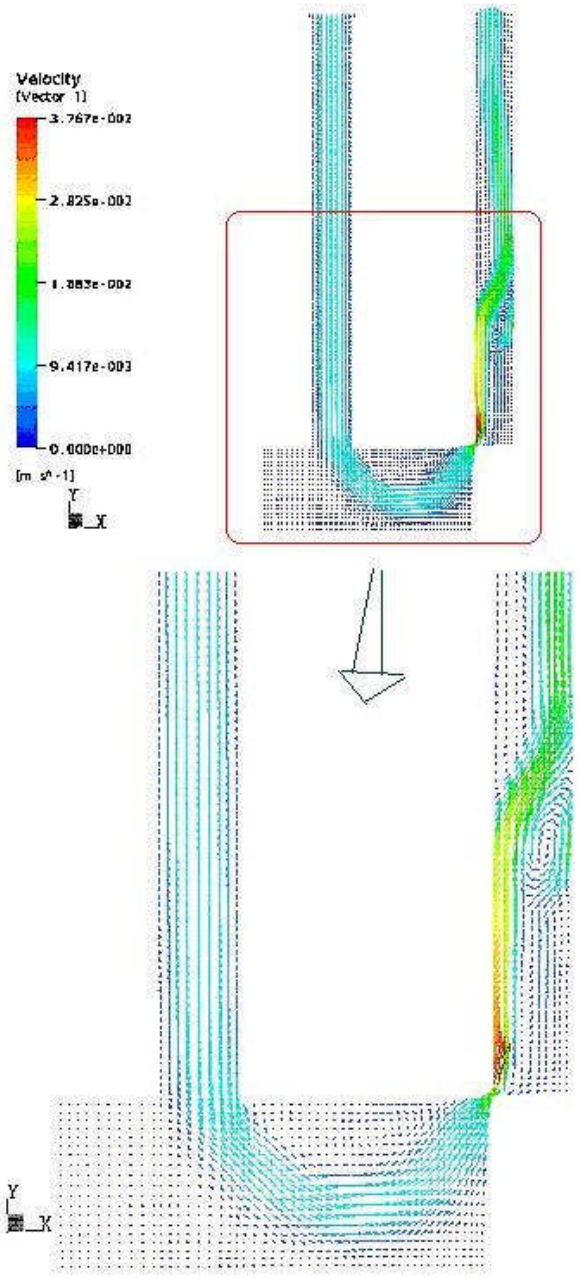

Figure 3.7: The velocity vector field for a spool opening of 0.375 cm (CFX 5.6 simulation)

The velocity vector plots for spool openings of 0.75 cm and 1.125 cm are shown in Figures 3.8 and 3.9. By comparing Figures 3.7, 3.8 and 3.9, it is seen that the jet attachment to the wall changes dramatically, as the opening increases. The attachment length of the wall jet is longer when the spool opening is smaller and vice versa. As the opening becomes larger, (i.e. from 0.375 cm to 0.75 cm to 1.125 cm), the velocity of fluid through the restriction is reduced.

.

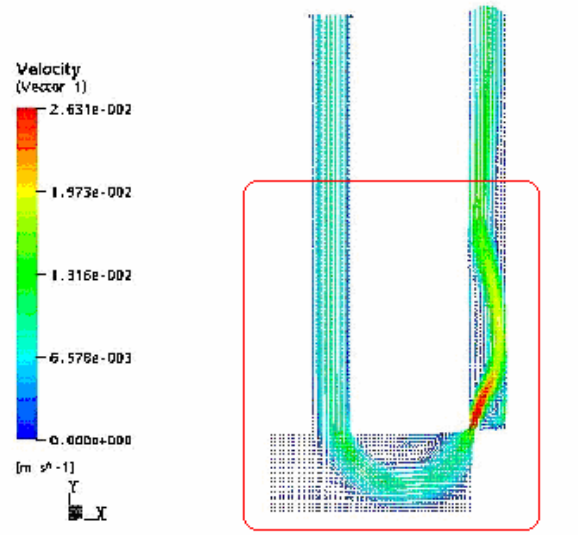

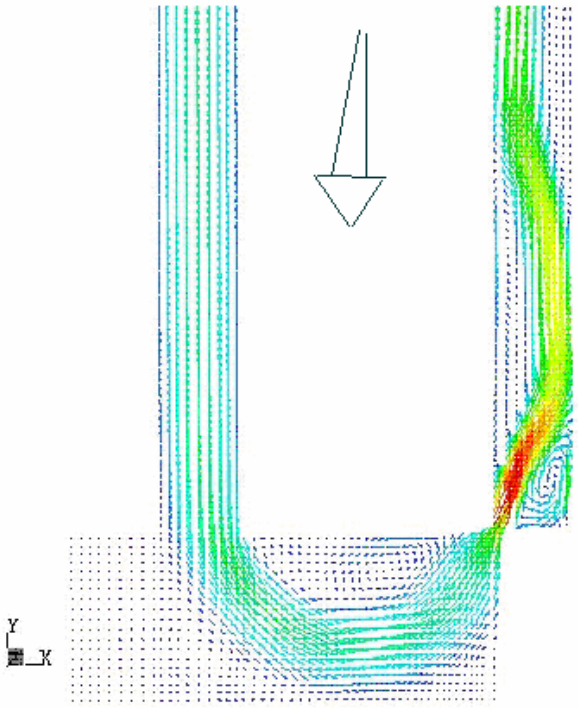

Figure 3.8: The velocity field for a spool opening of 0.75 cm (CFX 5.6 simulation)

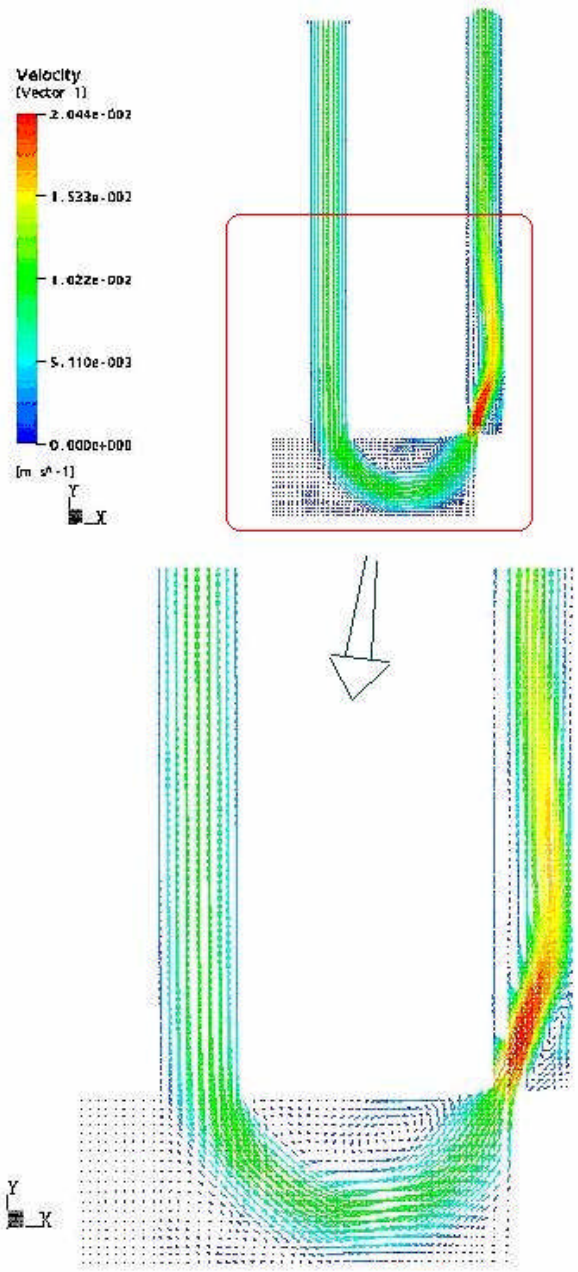

Figure 3.9: The velocity vector field for a spool opening of 1.125 cm (CFX 5.6 simulation)

3.4.1 Comparison of CFX 5.6 Prediction to Gao's PIV and FEM Results

Since the CFX 5.6 results will be compared to those predicted by both the PIV and FEM methods of Gao (10), a brief description of the PIV method is provided in Appendix E. The PIV method is a flow measurement technique which measures the local velocity vector throughout a spatial section of the flow field. This section will compare the CFX 5.6 results to those of Gao at two sections of the computational model as shown in Figure 3.10. The velocity profiles are shown in Figures 3.11 and 3.12.

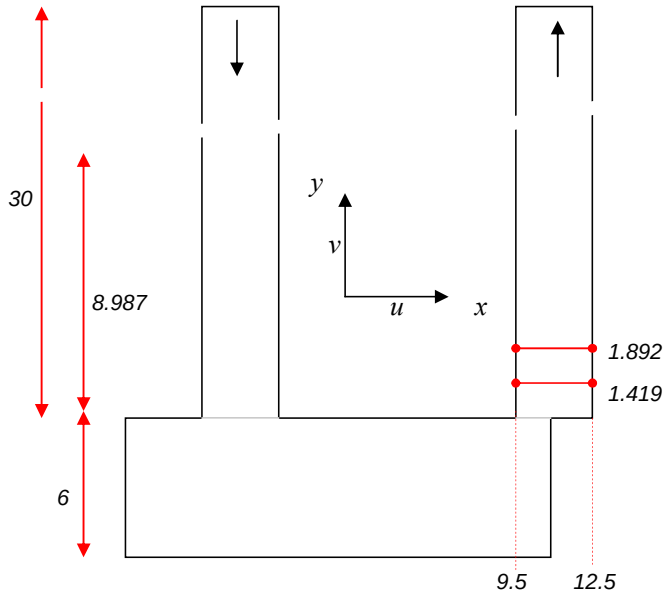

Figure 3.10: Locations in the outlet port where velocity profiles are compared

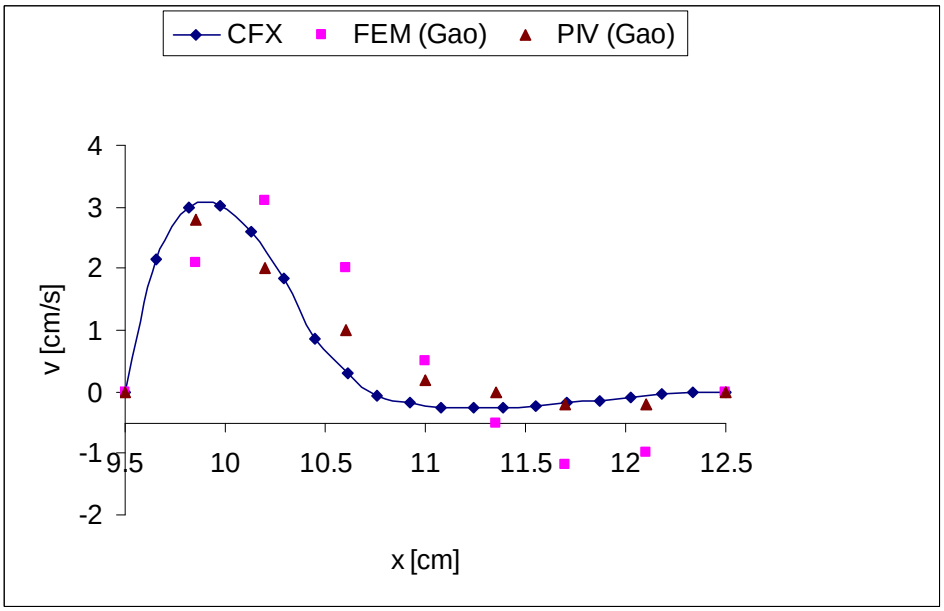

Figure 3.11: Vertical velocity profiles at y = 1.419 cm for a spool opening of 0.375 cm

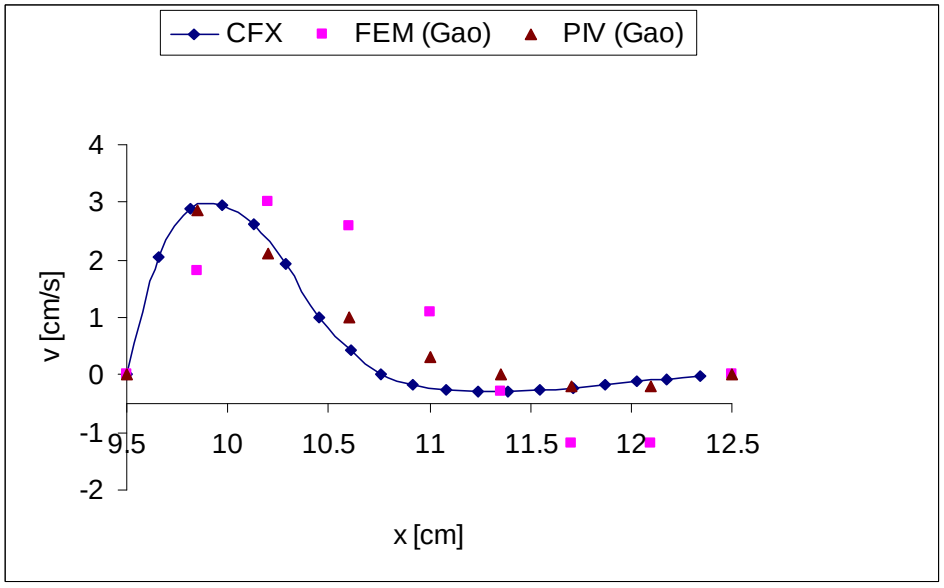

Figure 3.12: Vertical velocity profiles at y = 1.892 cm for a spool opening of 0.375 cm

In Figures 3.11 and 3.12, the three velocity profiles differ from each other. The FEM simulation by Gao has the highest velocity values and produces the largest recirculation zone (region of negative velocity). Its peak velocity occurs at x = 10.2 cm. The simulation with CFX 5.6 and the PIV measurements were in better agreement at these locations, with the peak velocity occurring at the same location (x = 9.8 cm). Figures 3.13 and 3.14 show the horizontal velocity profiles at locations in the outlet port where velocity profiles are compared**.**

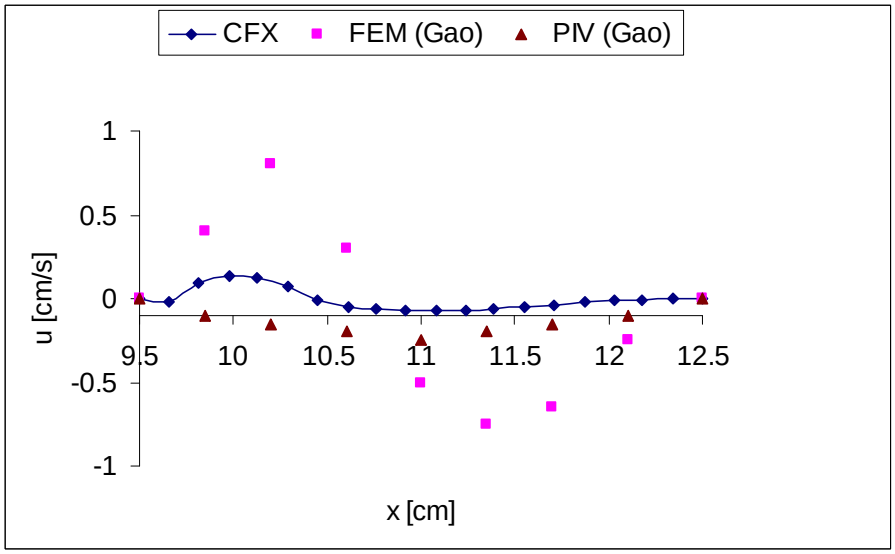

Figure 3.13: Horizontal velocity at y = 1.419 cm for a spool opening of 0.375 cm

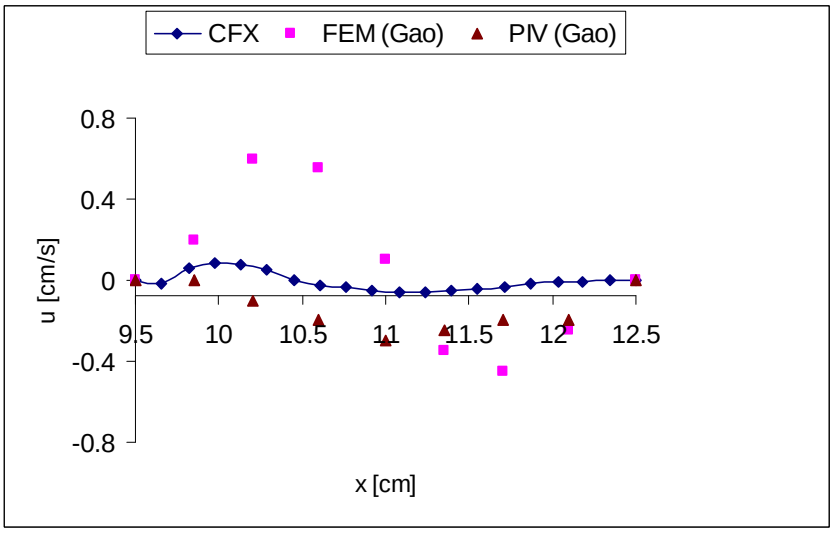

Figure 3.14: Horizontal velocity at y = 1.892 cm for a spool opening of 0.375 cm

From Figures 3.13 and 3.14, it is seen again that the FEM results do not agree with the PIV measurements or the CFX 5.6 results. The CFX 5.6 results match the PIV results of Gao but do not match his FEM results because the flow at this section is affected by Gao's poor choice of exit boundary condition.

The results for other openings of the spool (i.e. 0.75 and 1.125 cm) are presented in section 4 of Appendix E. However, there were no PIV data available for comparison for these openings.

3.5 Summary

To illustrate the numerical method, CFX 5.6 was used to simulate the same valve flow as considered by Gao (2004). This section introduced the reader to the use of the software. The simulated results were compared to both FEM and experimental results of Gao (10). The CFX 5.6 predictions agreed better with Gao's PIV measurements than did his numerical predictions. Gao also likely did not assess quality of solution. The reason is probably that the boundary conditions defined in the CFX 5.6 simulation more closely

represented the flow condition in his PIV experimental set up. While this is not a validation of the CFX simulation, the results do indicate a reasonable level of confidence in the CFX 5.6 approach.

Chapter 4

Simulation Results and Analysis of the Flow Field inside the Spool Valve

4.1 Introduction

This chapter will investigate the flow conditions inside a portion of the spool valve. In order to analyze the flow field inside the interior passages, detailed flow field information is calculated for orifice openings of 0.375, 0.5, 0.75 and 1.05 mm so as to provide visualization and specific information regarding the velocity, pressure, flow and other relevant variables. Analysis of the flow field enables the SSFF to be calculated. The same analysis is repeated for the rimmed spool valve, and a modified form of the rimmed land referred to as a "sharp edge tapered rim spool land" (a configuration which was used to compensate for the SSFF).

The objective of this chapter is to provide a visual understanding of the flow patterns in specific interior passages of conventional and rimmed spools, and to identify the flow mechanism whereby flow forces are reduced by the machining of a rim and tapered rim on the land of the spool.

4.2 Geometrical Model of Standard Spool Valve

For this initial study, only a 2D problem was examined. This was considered to be important because the approach would allow comparison to the classical 2 D control volume approach of the flow reaction forces. Figures 4.1.1 - 4.1.5 illustrate how the geometry of the actual spool chamber transforms to a form which accommodates the 2D geometrical representation. Figure 4.1.1 shows the assembly of the 3D valve showing the spool and sleeve. Figure 4.1.2 shows the diagram of the 3D spool and the rod while the

shaded area A_{eff}, in the figure is the area on the spool that the fluid pressure is acting upon.

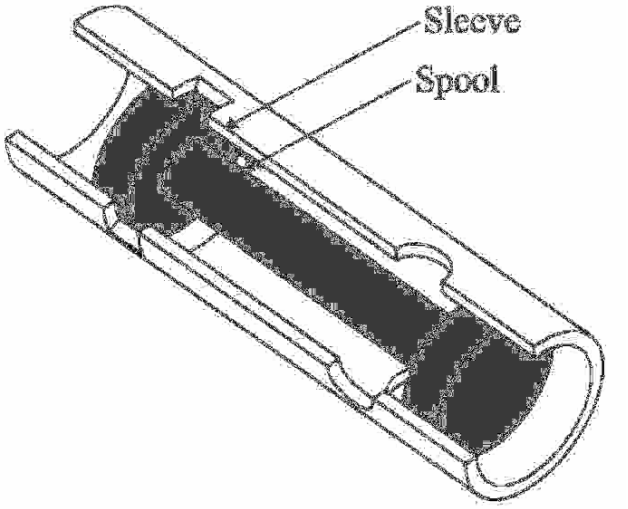

Figure 4.1.1: Assembly of 3-D spool valve

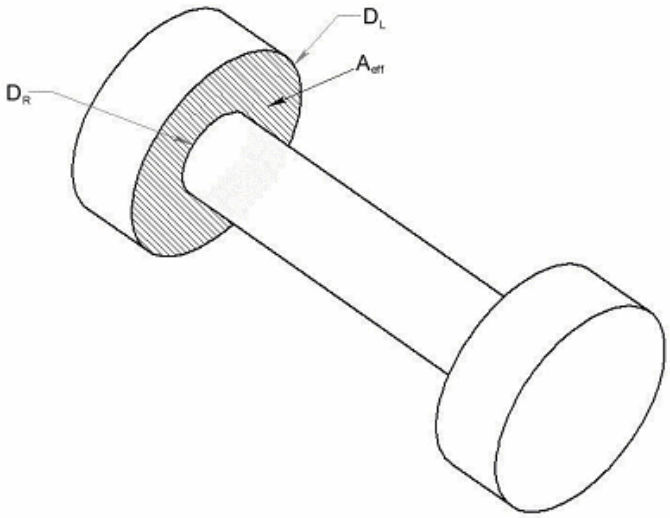

Figure 4.1.2: 3-D spool and rod

Figure 4.1.3, shows the 2D representation of the spool when spool was "unrolled". Appropriate nomenclature is defined in the figure. With reference to Figure 4.13, the

"length" in the figure is the length between the lands and the "height" is the difference between the spool and rod diameter.

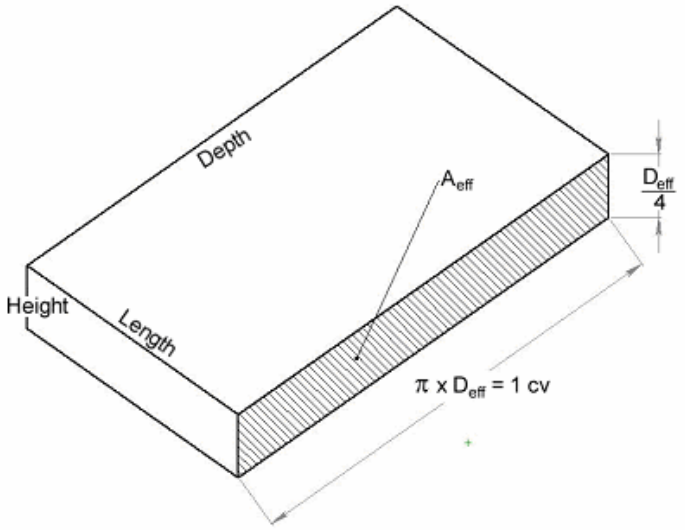

Figure 4.1.3: Representation of the 3-D model by a 2-D model

The depth of the domain was taken to be πD_{eff} (D_{eff} shall be defined shortly in equation 4.2) and the height of the land or face was $D_{eff} / 4$. Figure 4.1.4 shows the actual valve sleeve which consists of four inlet and four outlet slots that are symmetrically placed around the circumference of the sleeve. However, the 2D approximation as shown in Figure 4.1.3 approximates these slots as cuts across the whole circumference of the sleeve as shown in Figure 4.1.5.

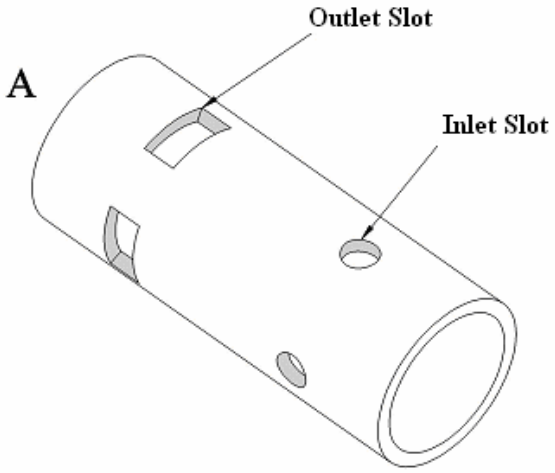

Figure 4.1.4: Representation of the actual inlet and outlet slots on the sleeve for the 3-D model

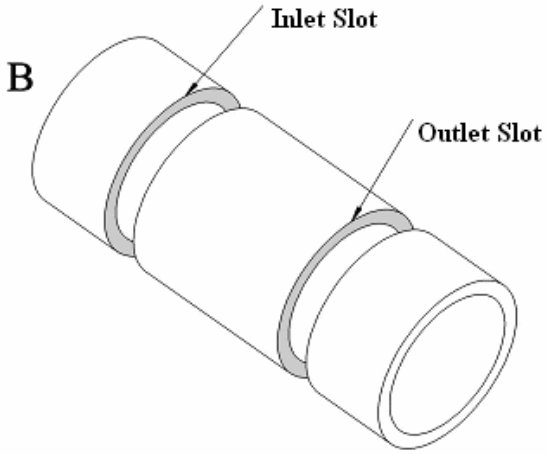

Figure 4.1.5: The approximate representation of the 2-D model of the valve

Hence, the depth of the orifices on the physical spool land was not equal to πD_{eff} (as defined in Figure 4.1.3), but some value smaller. A consequence of doing this was that the flow rates for a given spool displacement and pressure drop in this study would be

slightly larger. Since the objective was to compare different geometries for the same operating conditions, this was considered to pose no problem for this particular study.

As mentioned above, the actual valve model was 3D, but for this study, only a simplified 2D model was considered. In order for the pressure and velocity fields from the 2D model to closely represent the 3D situation, some scaling was done for the variable orifice area A_v, and the pressure force acting on the piston (land) face (see Figures 4.1.3). For example, in order to represent the force due to pressure acting on the land face correctly, the 2D model must maintain the same value of pressure per unit area for the land (piston) face. Hence,

$$A_{eff} = \frac{\pi}{4}\left(D_L^2 - D_R^2\right) = \frac{D_{eff}}{4}\left(\pi D_{eff}\right) \tag{4.1}$$

where D_{eff} was evaluated from the equality as,

$$D_{eff} = \left(D_L{}^2 - D_R{}^2\right)^{1/2} = Height \tag{4.2}$$

Hence the force due to pressure acting on the effective area of the land is given as;

$$F_l = PA_L = P\left(\frac{\pi D_{eff}{}^2}{4}\right) = P\left(\frac{D_{eff}}{4}\right)\left(\pi D_{eff}\right) \tag{4.3}$$

As mentioned above the area of the orifice was approximated by the relationship

$$A_v = x_v w = x_v\left(\pi D_{eff}\right) \tag{4.4}$$

By taking advantage of the symmetrical features of the valve, the 2D geometrical model can be simplified as shown in Figure 4.2. The depth of the domain (see Figure 4.1.3) and the height of the chamber were taken to be πD_{eff} and D_{eff}, respectively, where D_{eff} is the effective diameter of the spool (see Figure 4.1.3).

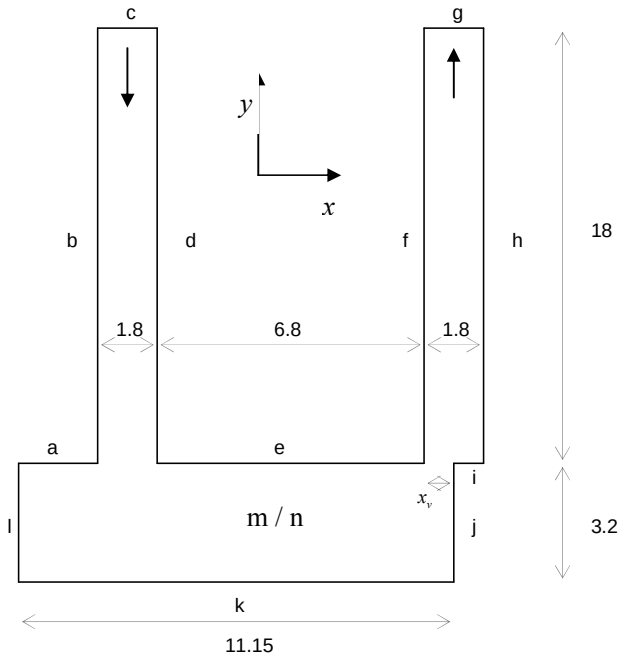

Figure 4.2: Schematic of the model geometry for a standard spool valve. All dimensions are in mm. The labels (a, b, c, etc.) represent specific boundaries

4.3 Boundary Conditions

The implementation of the pressure boundary condition in CFX 5.6 follows the same procedure discussed in section 2 of Appendix D.

With reference to Figure 4.2, the inflow boundary (*c*) was set as a pressure boundary with $p = 2.34$ MPa. The outflow boundary (*g*) was also set to a pressure boundary but with $p = 0.34$ MPa. Lower pressures were chosen to accommodate the visualization of the flow and pressure patterns. Typical pressure differentials range from 1 MPa to 10 MPa depending on the application. Increasing the pressure differentials (and flow rates) simply increases the magnitude of the flow forces. However, because the object of the study was to compare how a change in the land geometry would affect the flow forces for the same operating conditions, the choice of pressure was more dependent on facilitating the visual representation. The surfaces *m* and *n* lie "on top" and "beneath" the page and cover the

whole shape; thus low and high *z* surfaces were defined as symmetry boundaries. A no-slip boundary condition was imposed on all wall surfaces (*a, b, d, f, h, i, j, k* and *l*). The same boundary conditions were used for the simulation of each orifice opening.

4.4 Fluid Properties

The physical properties of the fluid were set to 871 kg/m^3 for the density and 0.0375 kg/m.s (40^{o}C) for the dynamic viscosity, which corresponds to a kinematic viscosity of 43 centistokes. These parameter values were consistent with those used in the experimental studies by Chan et al. (6).

4.5 Solution Process

The details of the CFD process and solution have already been discussed in Chapters 2 and 3. Some additional information presented in this section is for the sake of clarity and completeness.

The 2D geometry for four different displacements of the spool $(x_{v1}...x_{v4})$ is shown in Figure 4.3. The figure shows that as the spool is displaced from one position to the other, the axial length of the chamber l, remains the same.

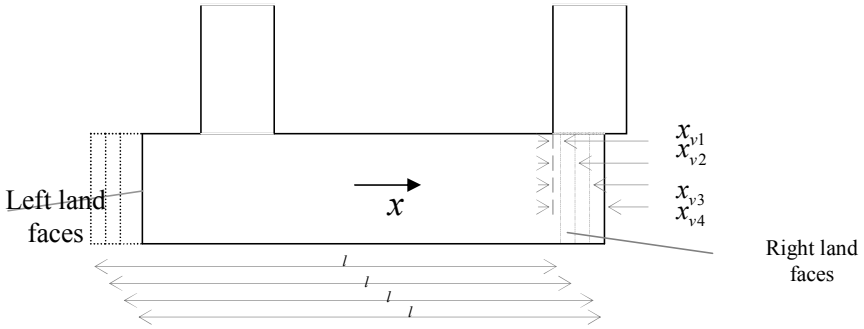

Figure 4.3: Simulation approach

The 2D geometries were created and meshed using the CFX 5.6 numerical software by applying the same procedure as described in section 1 of Appendix D. The number of the control volumes used for all simulations ranged between 23,175 and 23,548 computational nodes. All the meshes that were used in this study were structured and hexahedral in shape. On the discretized mesh, the RANS equations take the form of a system of algebraic equations. At each node at least 5 variables were solved for, namely: pressure, the two velocity components in x and y, the turbulent kinetic energy and the dissipation. As mentioned in the preceding chapter and in particular, section 1 of Appendix E, the Shear Stress Transport (SST) turbulence model was adopted, (which has been validated for a wide variety of flows). Apart from round-off errors, the approximations associated with the turbulence model and the order of the differencing scheme that was applied to discretize the key transport terms (advection and diffusion), represent an possible sources of errors in the calculations. A second order differencing scheme available in the CFX 5.6 code was used to model the convective–diffusive transport. Simulations were done for the four different spool positions using the same boundary conditions and fluid properties.

The flow was modeled in CFX 5.6 as Newtonian, turbulent everywhere (except at the wall) steady and incompressible. The CFX 5.6 code uses the finite volume method to discretize the RANS equations. The 'Auto Time Scale' option available in CFX–Pre was chosen at first, and the solver allowed to run for a few iterations. The calculation did converge but at a very slow rate. A physical time step of 0.01 seconds, which was larger than the auto computed values, was then set to accelerate the solver. For a given problem, the solver typically ran for 2 1/2 hours, and convergence of the solution was achieved after approximately 1000 iterations.

Grid refinement[1] was used to ensure that the numerical errors were sufficiently small on the final mesh to enable meaningful conclusions to be drawn from the simulation results. A refinement of the grid near the restriction was done to create a more refined grid in this

[1] As the grid is refined, the grid cells become smaller and the number of cells in the flow domain increase; thus, the spatial discretization errors should be reduced.

region, where pressure and velocity gradients were substantial. The grids used to test the refinement are summarized in Table 4.1.

Table 4.1: Grids used to test the refinement of simulation for spool opening of 0.5 mm. The grids were tested at 3 points; Point 1 - x = 6 mm, y = 1.6 mm; Point 2 - x = 10 mm, y = 3 mm; and Point 3 - x = 11 mm, y = 10 mm in the flow domain.

Mesh Type	**# of Mesh Elements**	**Points**	**Velocity vector (m/s)**	**Pressure (MPa)**
Coarse	3,192	1	6.23	2.17
		2	2.85	2.31
		3	7.42	-0.39
Medium	7,192	1	6.10	2.16
		2	2.33	2.25
		3	7.26	-0.38
$Fine_1$	12,890	1	5.97	2.16
		2	2.23	2.23
		3	7.19	-0.37
$Fine_2$	15,690	1	5.97	2.16
		2	2.23	2.23
		3	7.19	-0.37

From Table 4.1, it is seen that the solution at the three points becomes insensitive to further grid refinement.

Negative pressures were predicted by the simulation at various points in the valve. This is not physically possible for this situation and will be discussed in Section 4.7.1

4.6 Near-Wall Resolution

As discussed in section 2 of Appendix E, the mesh for turbulent flow was based on the wall distance y^+, which indicated the near-wall refinement. Hence for turbulent flow calculations, it was desirable to check the values of y^+ before modifying the mesh since turbulence models only work well for specified ranges of y^+. Outside the specified range, these models are not valid; the consequence is that the wall shear calculations would be wrong, which could then affect the flow pattern. As indicated earlier, the SST model was used. As stated in the CFX 5.6 user manual, the advantage of the SST model is that the y^+ value could be from anything less than 0 to up to 300. In this study, for all walls, the y^+ values are between 0 to 5 which meets the criterion.

4.7 Simulation Results

The results of the computation of the flow field were presented in terms of vector plots of velocity and contour plots of static and total pressures at the symmetry plane. For simplicity, the case of x_v = 0.5 mm is presented only. The results for the other openings (x_v = 0.375 and 0.75 mm) of the spool are contained in section 3 of Appendix F.

4.7.1 Analysis of the Flow Field

In order to facilitate a visual analysis of the flow structure, the plots of velocity vector and pressure contour for the meter–out orifice, are shown in Figures 4.4 and 4.5, respectively. (Similar plots for the meter-in condition are presented in section 2 of Appendix F). In the valve chamber, the flow pattern in the regions between the entry port and the metering section is observed to be complicated. The plot shows the acceleration of the fluid (through a visual comparison of the velocity colors) across the metering section. The flow on exiting the metering section separates as a result of the sharp corner at the restriction which created a recirculation zone downstream of the metering section. A total of 5 recirculation zones labelled *A, B, C, D* and *E* in Figure 4.4 are observed to be formed at different locations in the flow field.

From Figure 4.4, it is noted that the fluid is stagnant in some regions inside the chamber. In addition, it can be seen that the flow of fluid from the chamber is at an inclination with the valve axis after going through the bend.

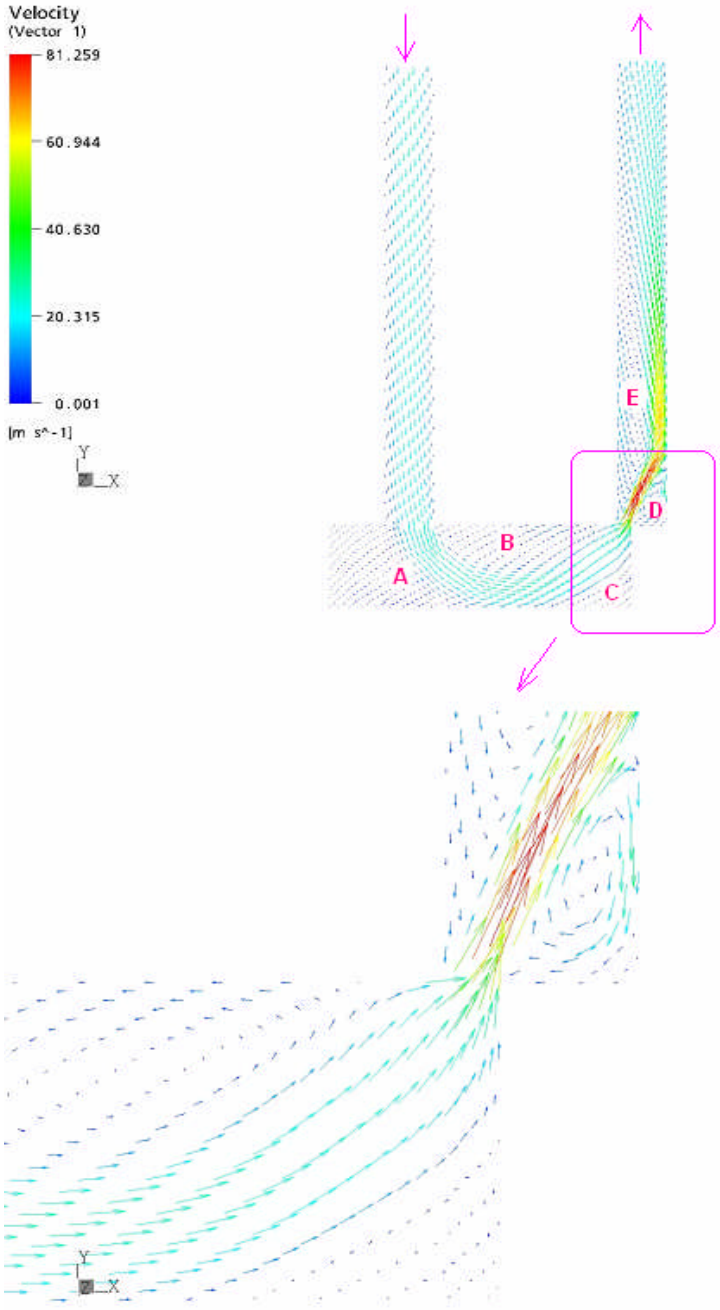

Figure 4.4: Velocity vectors of the flow field showing recirculation zones (A, B, C, D and E). The estimated jet angle from the CFD analysis is 65.54^{o}

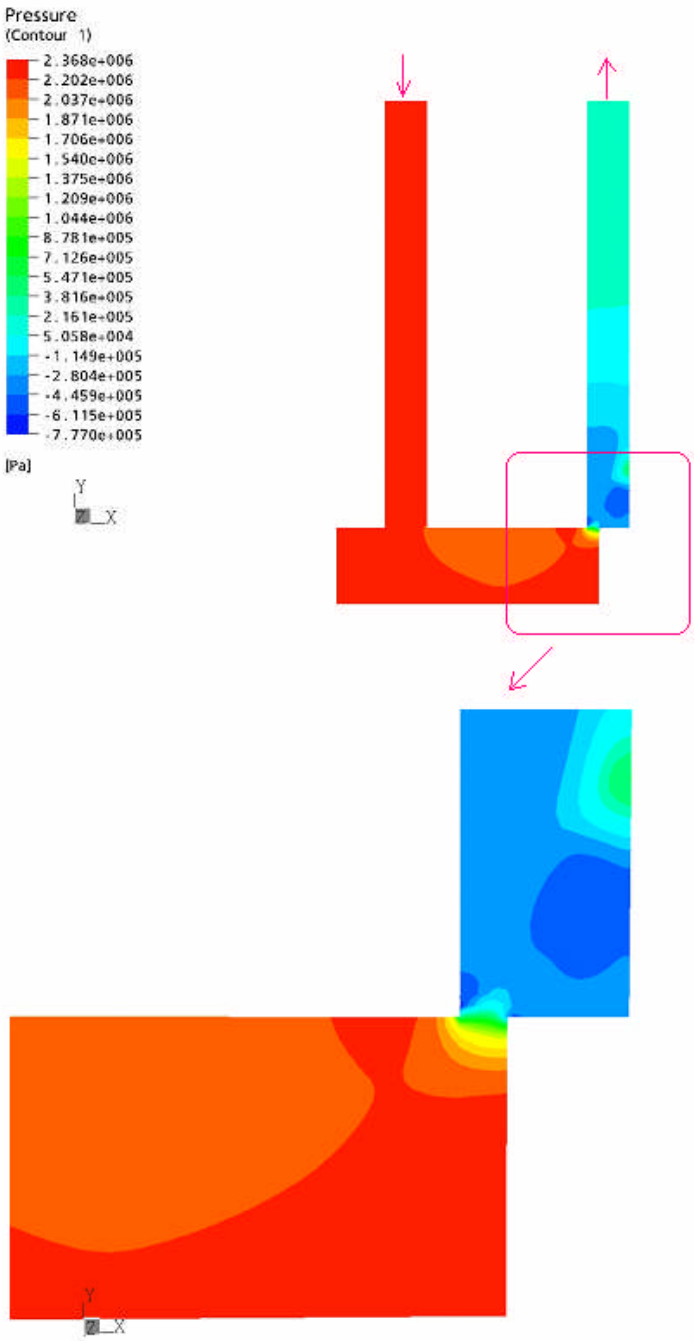

Figure 4.5: Pressure plot for the standard spool configuration (x_v = 0.5 mm). The estimated steady state flow forces from the CFD analysis is 6.31 N

The detachment of the flow at the metering section causes a "negative" pressure of -0.77 MPa (-112.65 Psi). In reality, negative pressures of this magnitude do not exist since the limiting value is -0.1 MPa (-14.7 Psi). However, CFX does not recognize or compensate negative pressures unless it has a cavitation model built into it. Thus, negative pressures of any magnitude are not flagged as a peculiarity. In this work, it is the pressure difference across the orifice and indeed, the valve and chamber itself which determines flow rate and as such, the absolute pressure does not affect the results. The level of negative pressure depends on the input level (magnitude of the inlet (2.34 MPa)and outlet pressure (0.34 MPa)), which in this study is quite low. To confirm this, the simulation was rerun by maintaining the same pressure drop across the valve (i.e. to ensure that the SSFF would remain the same), and increasing the input pressure from 2.34 MPa to 12.34 MPa, and the outlet from 0.34 MPa to 10.34 MPa. The result for the pressure field is presented in Figure 4.6. The SSFF was estimated to be 9.56 N giving the same results as for the case when the pressure level was small. It is apparent that negative pressures are not observed in the pressure profile of Figure 4.5. Thus, the presence of negative pressure in the pressure plots was not of concern in the interpretation of the results but in a real application, it would indicate the existence of cavitation (which was not considered in this study). Thus, for all subsequent plots and discussions, the results are given for only the lower pressure conditions.

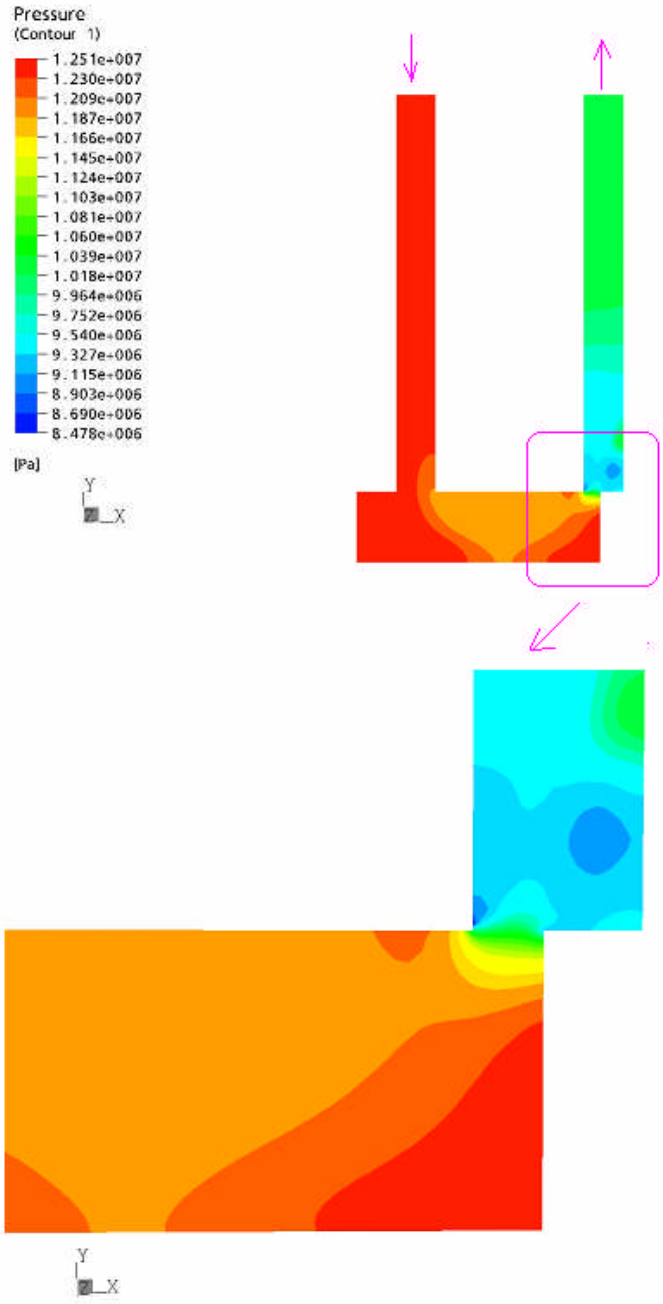

Figure 4.6: Pressure plot for the standard spool valve configuration when the magnitude of the inlet and outlet pressure was increased

For a load pressure of 0.34 MPa, Figures 4.7 and 4.8 show the pressure distribution on the left and right land face, respectively. From Figure 4.7, it is observed that the pressure acting on the left land face is almost independent of vertical position as the adjacent fluid moves only slowly in this region. This confirms the assumptions made in the control volume analysis that the fluid in this region is at a "dead end" (stagnant).

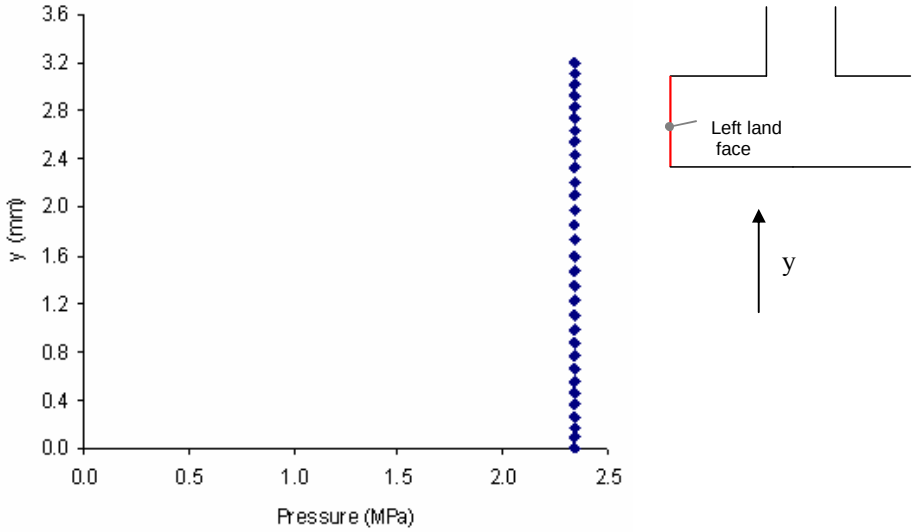

Figure 4.7: Static pressure plot on the left land face

Figure 4.8 shows the abrupt decrease in pressure along the right land face due to the acceleration of the fluid through the metering orifice.

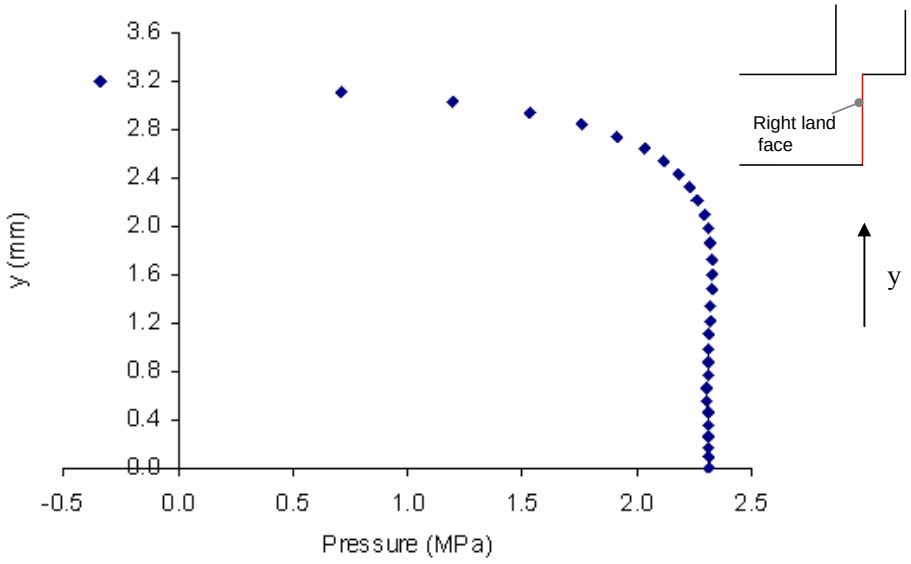

Figure 4.8: Static pressure plot on the right land face

To examine the flow in the chamber, data for velocity and pressure were extracted from a cross-section midway in the chamber. The plots are presented in Figure 4.9 for the velocity components and Figure 4.10 for pressure. Inside the chamber, it is seen that the fluid velocity is substantial in the axial direction and negligible in the radial direction. The velocity is higher in the lower regions than in the upper regions where there is significant flow.

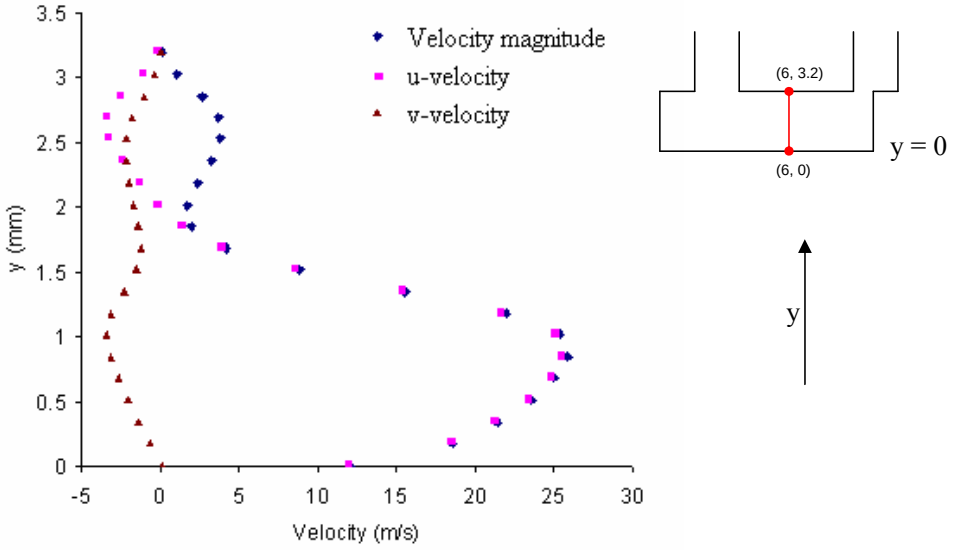

Figure 4.9: Cross-sectional plots for the standard spool configuration (x_v = 0.5 mm). The data were extracted at a location in the middle of the chamber (x = 6 mm, 0 < y < 3.2 mm)

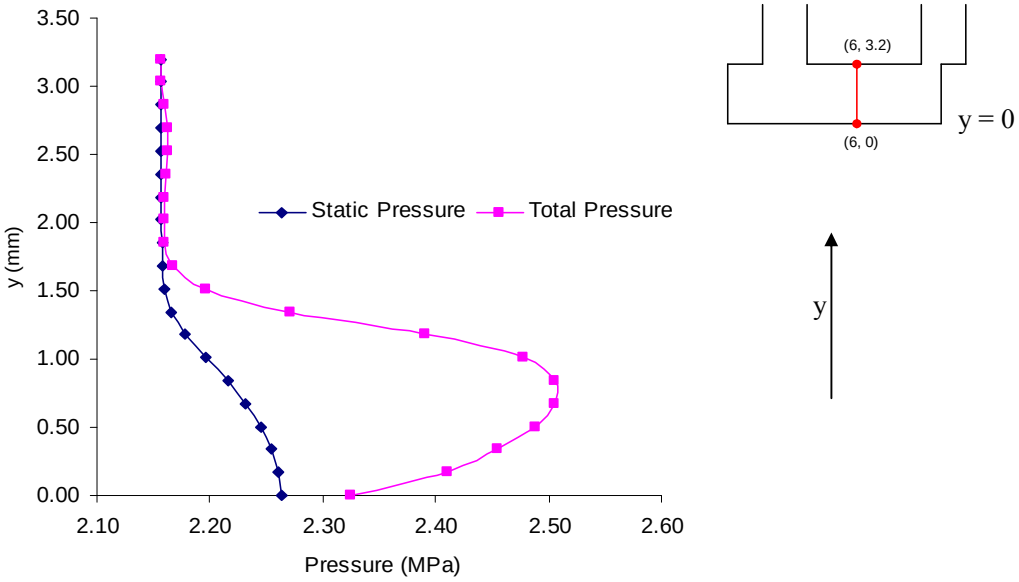

Figure 4.10: Plots for the standard spool configuration showing the static pressure along a line section in the chamber. The line data were extracted at the location mid-way in the chamber (x = 6 mm, 0 < y < 3.2 mm)

The velocity plot through the metering section is shown in Figure 4.11, with the highest velocity of 78 m/s.

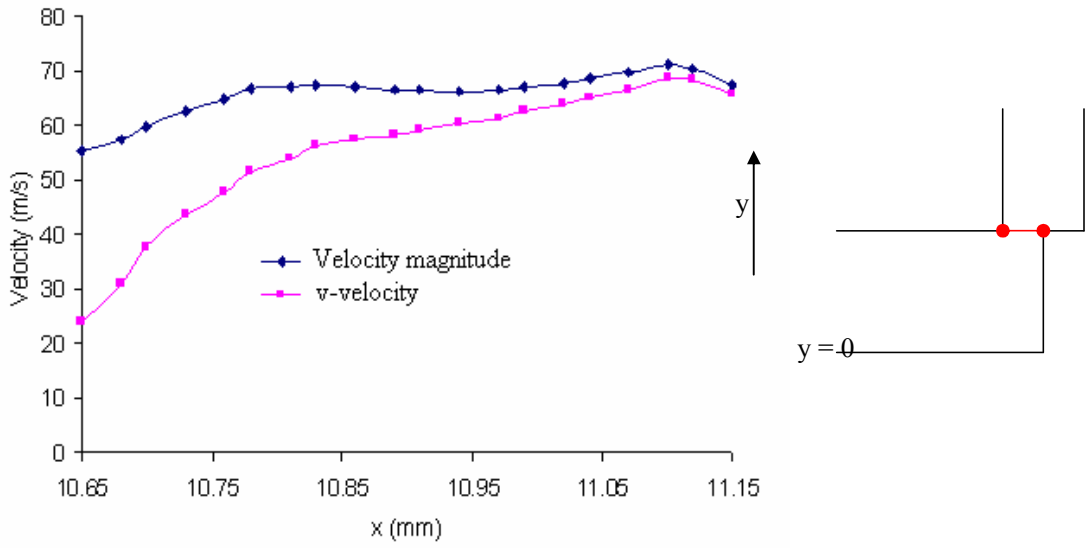

Figure 4.11: Velocity plot through gap (orifice opening, x_v)

4.7.2 Deducing the Fluid Jet Angle

The fluid discharge jet angle at the metering orifice is an important parameter in SSFF calculations. In the classical force equation, the fluid jet angle is assumed to be 69° as presented by Richard Von Mises (1883 – 1953). However, results from CFD studies (10, 14) have indicated that the jet angle varies with spool opening, spool geometry and flow Reynolds number. In this study, a systematic approach is used to estimate the fluid jet angles. Several methods can be used to calculate the fluid jet angles. In general, the angle is difficult to define as it is derived from a theoretical description of the flow which ignores the details of the velocity distribution at the orifice (i.e. the flow may exit the orifice at many angles along the orifice opening which means that a definitive jet angle may not exist). One approach could be to calculate the local mass fluxes (x and y) and then combine them to obtain some average value for the fluid jet angle. Another approach is to calculate streamlines at the jet orifice; one estimate of the angle might be then to use the angle of discharge where the local mass flux is greatest. Another possibility is to examine the velocity vectors along the orifice section (which should give the same information as streamlines). Another approach, which was adopted in this study, would

be to sum the local components of the velocity, weighted by the control volume area. It is recognized that other approaches could be used but since a standard approach has not been defined in the literature, this method was adopted in this study and is described in greater detail in section 1 of Appendix F.

Using this approach, the simulated jet angles for the different spool openings were calculated and are summarized in Table 4.2. The parameter A_o in Table 4.2 is used in the calculation of the flow forces in the classical equation.

From Table 4.2, it is observed that the jet angle θ, does vary with the opening of the spool but tends to 69^0 at larger openings.

Table 4.2: The estimated jet angle from CFD analysis for standard spool land

			CFD
$x_v(mm)$	$A_o(m^2)$	$Q(m^3/s)$	$\theta_{cfd1}(°)$
0	0	0	0
0.375	3.37 e -6	2.02 e -4	65.34
0.5	4.50 e -6	2.78 e -4	65.54
0.75	6.74 e -6	4.50 e -4	66.21
1.05	9.44 e -6	7.50 e -4	69.25

In this section, only the velocity vector and the pressure contour plots for a spool opening of 0.5 mm (Figures 4.5 and 4.6, respectively) have been presented. The plots and discharge jet angles for other openings of the valve for the meter - out orifice are contained in section 2 of Appendix F.

4.7.3 Flow Reaction Forces

In this section, equation (2.3) shall be redefined to be the Total Steady State Flow Force (TSSFF) which includes the viscous and classical force terms, while the SSFF is the classical definition that excludes viscous effects. Hence,

$$TSSFF = \underbrace{\iint_{A(LeftFace)} PdA - \iint_{A(RightFace)} PdA}_{SSFF} \pm \eta \underbrace{\iint_{A(Rod))} \tau_{Rod}\, dA}_{Viscous} \tag{4.6}$$

where the first term on the *R.H.S* of equation (4.6) is the integrated pressure force acting on the right land surface (*LeftFace*), the second term is the integrated pressure force acting on the left land surface (*RightFace*) and the last term is the viscous force acting on the rod surface. η is a switching function that is used to turn the viscous force "on" and "off", and could take the value of 0 and 1. When η is 0, the classical flow force equation (1) is invoked, and when η is 1, the TSSFF equation (Equation 4.6) is used. The positive sign indicates that the TSSFF is defined for a meter – out orifice and the negative sign indicates that the TSSFF is defined for a meter – in orifice,

The approach adopted here is to first compare the SSFF obtained from classical formulations to that evaluated from the CFD model (pressure profiles on the face), and then include the viscous terms after to determine the TSSFF.

In the CFX 5.6 code, the SSFF values are calculated using a method defined as "Pressure Integral", which is a built-in function of the CFD software which integrates the pressure distribution on both the land faces and then calculates the difference. The CFD program also outputs the viscous force by integrating the wall shear over the surface area of the rod. The viscous force constitutes approximately 5 – 10 % of the TSSFF in previous CFD simulations (14 and 15) but could reach up to 20 % or more in some special cases, where either the classical SSFF portion (as defined by Merritt, for example) is relatively small or there is a well-developed velocity field parallel to the spool displacement. The viscous force either adds or subtracts from the TSSFF depending on the metering strategy. In the

case of a meter – out orifice, the viscous force is additive to the SSFF and acts to close the spool. In the second case (reverse flow for the meter – in orifice configuration), the viscous force is subtractive to the TSSFF and reduces the effect of the SSFF (14).

The SSFF values for the four geometries corresponding to spool displacements x_v of 0.375, 0.5, 0.75 and 1.05 mm are summarized in Table 4.3. The classical SSFF is calculated using equation (2.4) by neglecting the viscous force and assuming the jet angle to be $69°$. From the table, it is seen that the classical method consistently underestimates the SSFF because of the assumed jet angle.

Table 4.3: The TSSFF estimated using the CFD approach compared to the classical approach

	CFD				**Classical**	
$x_v\,(mm)$	$\theta_{cfd1}\,(°)$	Viscous Force (N)	SSFF (N)	TSSFF (N)	$\theta_{clas}\,(°)$	SSFF (N)
0	0	0	0	0	0	0
0.375	65.34	0.0442	4.62	4.66	69	2.95
0.5	65.54	0.0593	6.18	6.24	69	3.93
0.75	66.21	0.0918	9.47	9.56	69	5.30
1.05	69.25	0.1313	12.97	13.10	69	8.25

From Table 4.3, it is evident that the SSFF and the TSSFF values increase as the valve opening increases.

4.7.4 Comparison of CFD with the Classical Equation

From Table 4.3, the CFD simulation results were compared to those obtained from the classical equation for flow force, noting that the classical force equation uses an assumed jet angle of $69°$. The difference between the CFD and classical results for the SSFF is

due only to the numerical estimation of the flow angle θ. To demonstrate this, the discharge angle θ_{cfd} obtained from the CFD results was substituted into the classical equation to obtain new values for SSFF. The idea was to ascertain if these force values were equal to the ones obtained directly from CFD simulations. The results are summarized in Table 4.4. Also, Table 4.4 also shows the percentage of viscous friction that is neglected from the classical equation.

Table 4.4: Percentage of the viscous friction to TSSFF on the spool

	CFD			**CFD/Classical**		**Percentage of the viscous friction to TSSFF**
$x_v(mm)$	Viscous Force (N)	TSSFF (N)	SSFF (N)	θ_{cfd} (^{o})	SSFF (N)	(%)
0	0	0	0	0	0	0
0.375	0.0442	4.66	4.62	65.34	3.49	0. 95
0.5	0.0593	6.24	6.18	65.54	4.62	1.0
0.75	0.0918	9.56	9.47	66.21	6.74	1.0
1.05	0.1313	13.10	12.97	69.25	8.29	1.0

From Table 4.4, it is seen that the percentage contribution of the viscous forces in the TSSFF is to 1 % or less. Also, it is seen that the SSFF values for the two approaches (classical and CFD methods) are quite different. One possible explanation for this difference is that the classical flow force equation uses the square root orifice equation which is really only an approximation. The orifice equation is derived from the Bernoulli's principle which is based on the following major assumptions: friction losses and turbulence effects are neglected, and the flow is one dimensional (flow along a

streamline). These conditions are only marginally satisfied in this situation. Li (14 and 15) found that the discharge coefficient for flow through an orifice based on his CFD results was 0.6693 (10 % higher than normally assumed value of 0.61) for the inflow condition and 0.7197 (18 % higher than normally assumed value of 0.61) for the outflow case. Another reason for the differences might be due to numerical error in the CFD model. However, the discrepancy here is in the order of 25%. The reason for such a difference has not been determined at this point and remains an area for future research. It is, however, an important observation because if substantiated experimentally, the classical formulation of the equation for flow through an orifice could be in error.

4.8 Inflow Condition for the Standard Spool Valve

Figures 4.12 and 4.13 show the velocity and pressure contour plots for the flow through the spool for the inflow condition. The same inlet pressure of 2.34 MPa and outlet pressure of 0.34 MPa was used in the simulation. The flow features are similar to that described in Figures 4.5 and 4.6 for the outflow condition. From Figure 4.13, a large pressure drop is seen between the upstream and downstream of the metering orifice, while the pressure variation inside the valve chamber is small. The highest velocity is at the orifice, and in some regions within the chamber the fluid is almost stagnant as indicated by the velocity vector plot of Figure 4.12. In particular, the region labelled D in Figure 4.12 is a stagnant region whereas the same region for the outflow condition (see Figure 4.5) was a recirculation zone. Similarly the region labelled C of Figure 4.12 is a recirculation region, but is a stagnant region for the outflow condition (see Figure 4.5). The regions labelled A, B and C in Figure 4.12 are recirculation zones. Recirculation regions are typically low velocity and therefore almost stagnant.

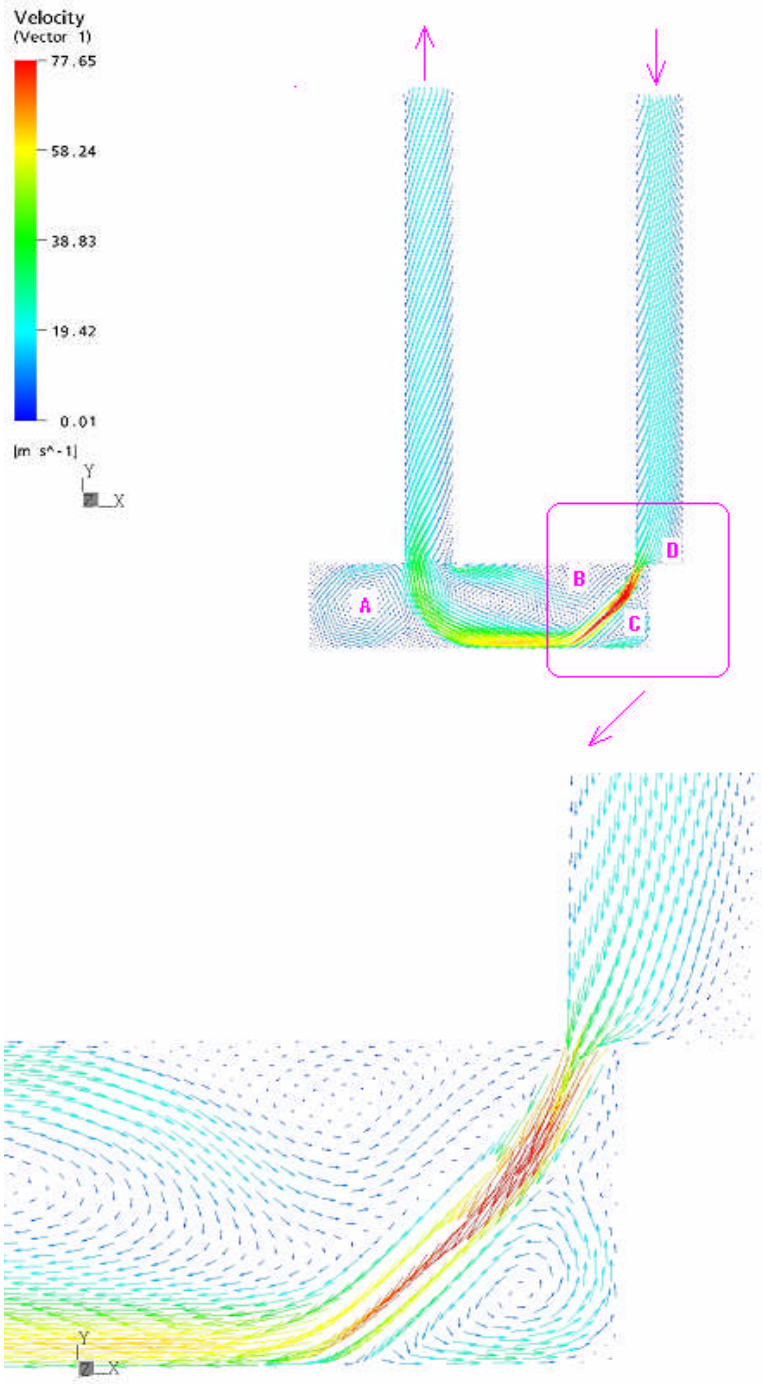

Figure 4.12: Velocity vectors for the standard (non-rimmed) spool configuration for the inflow condition (xv = 0.5 mm)

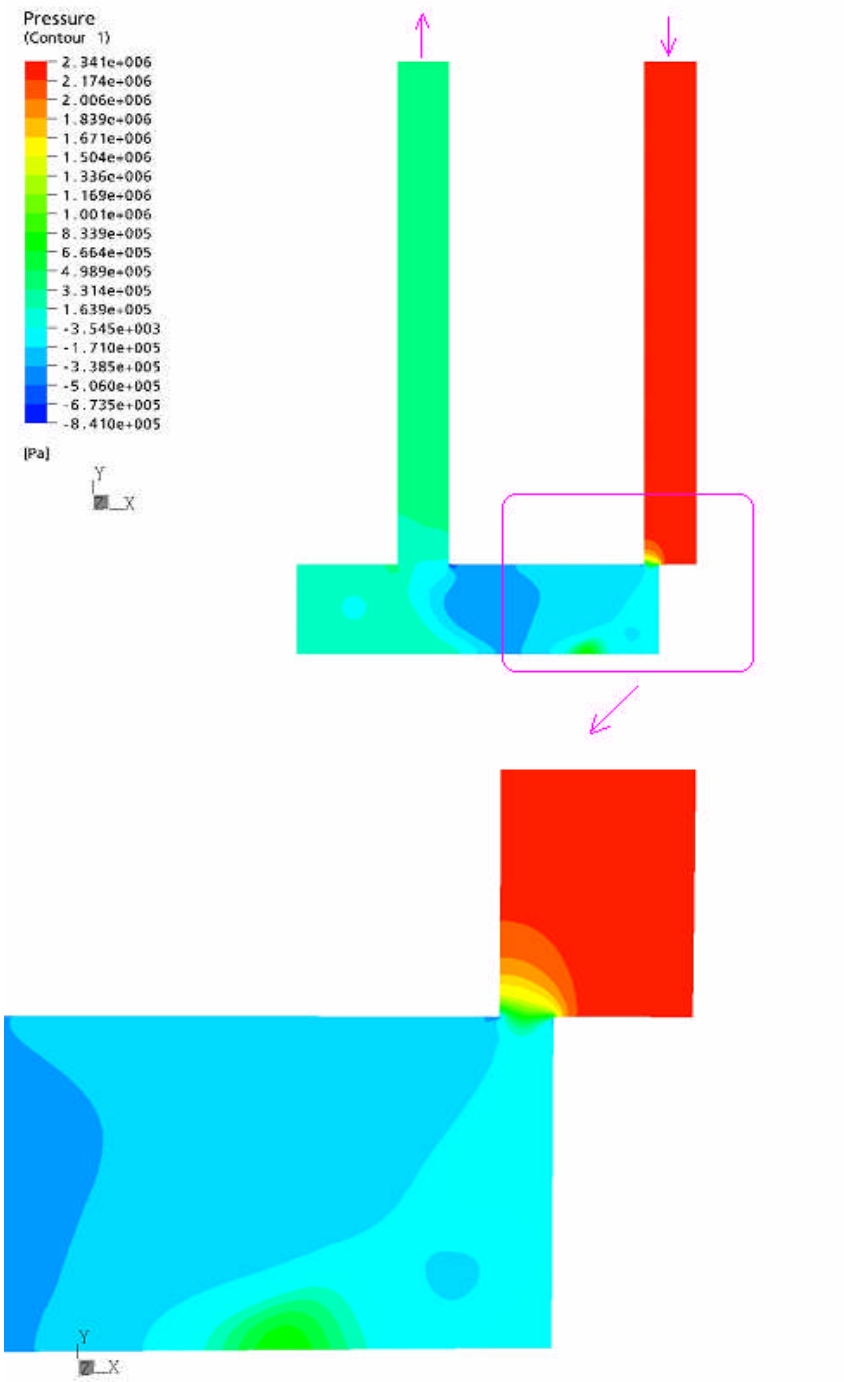

Figure 4.13: Pressure contours for the standard (non-rimmed) spool configuration for inflow condition (*xv* = 0.5 mm)

Figure 4.14 shows the pressure profiles on the right and left land faces for inflow condition. The pressure profile shows that fluid re-circulation occurred on the right corner of the right hand side of the spool ($2.5 < y < 3.2$ mm). The recirculation is a consequence of the flow separation caused by the sharp edge corner of the orifice. However, on the left hand face, the pressure profile is approximately constant. The results for the steady state flow forces as compared to the outflow condition are summarized in Table 5.5.

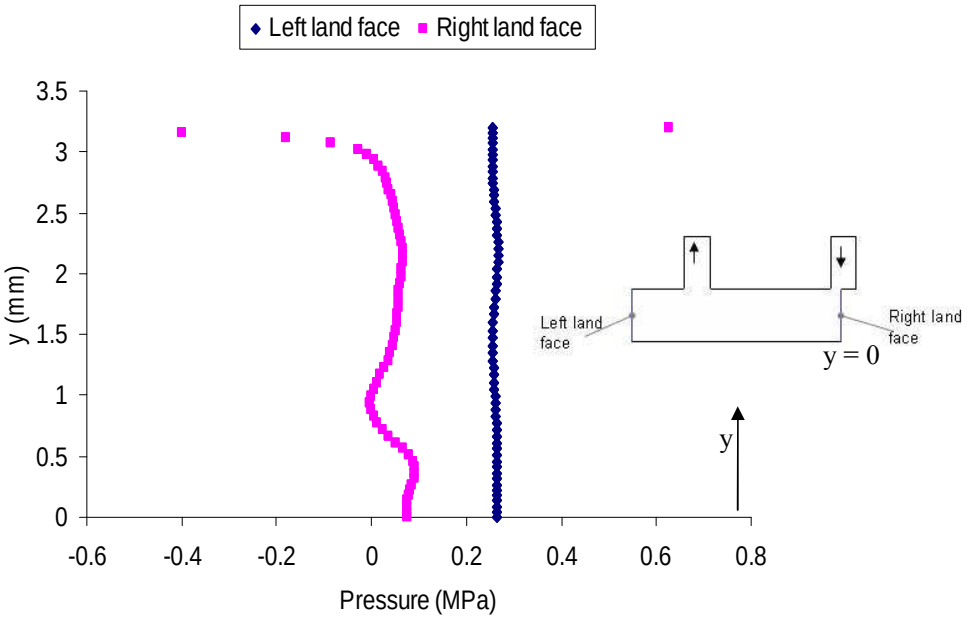

Figure 4.14: Static pressure plot on the left and right land faces for the inflow condition

Table 4.5: The estimated SSFF from CFD results for the inflow condition as compared to the outflow condition

	SSFF (N)	
$x_v(mm)$	Inflow	Outflow
0	0	0
0.375	3.21	4.62
0.5	6.14	6.18
0.75	7.82	9.47

In the classical approach to flow reaction forces, inflow and outflow SSFF are assumed to be the same for the same operating conditions, since jet angle is assumed to be 69^o for both cases. However, the results presented in Table 4.5 are very significant. The pressure profile on the right land face in Figure 4.14 (inflow condition) is substantially more uniform than that shown along the same surface in Figure 4.7 (outflow condition) in the region close to the orifice. This means that the differential closing steady state force on the land faces is smaller for the inflow than for the outflow conditions. These results in Table 4.5 appear to contradict the assumption that the SSFF for inflow and outflow condition is the same (1) and hence this defines an area that needs to be further investigated in the future.

4.9 Compensating for SSFF

The objective of SSFF compensation is to reduce the closing force. The initial method adopted in this study was by modifying the geometry as proposed by Chan et al. (6).

4.9.1 Rim Spool Valve

As mentioned earlier in the literature review section, SSFF compensation techniques have been studied by Blackburn (26) and Merritt (1). They compensated for the SSFF by focusing on altering the flow pattern at the variable orifice which involves re-shaping the spool or lands, or by the use of differential force at high flow. In one particular series of studies conducted by Chan on a flow divider valve (6, 7 and 8), it was shown that a rim machined into the lands of the spool reduced the flow dividing error by approximately 70-80 %. It was deduced that the main contribution to this reduction in error was due to a reduction in flow forces. Direct verification of the claim regarding flow force reduction was not achieved. Hence this section will attempt to present a better understanding of the reasons why this rim modification to the spool lands was successful in reducing flow forces.

Figure 4.15 shows the geometry of the spool valve with a rim (gap) cut into the land of the metering orifice. The rim spool configuration is defined in terms of the rim thickness, t_{rim} and rim depth, d_{rim}. The premise behind the use of the rim was that the pressure gradient across the meter orifices would act on a smaller portion of the rim face and not the entire land face where the pressure would essentially be static.

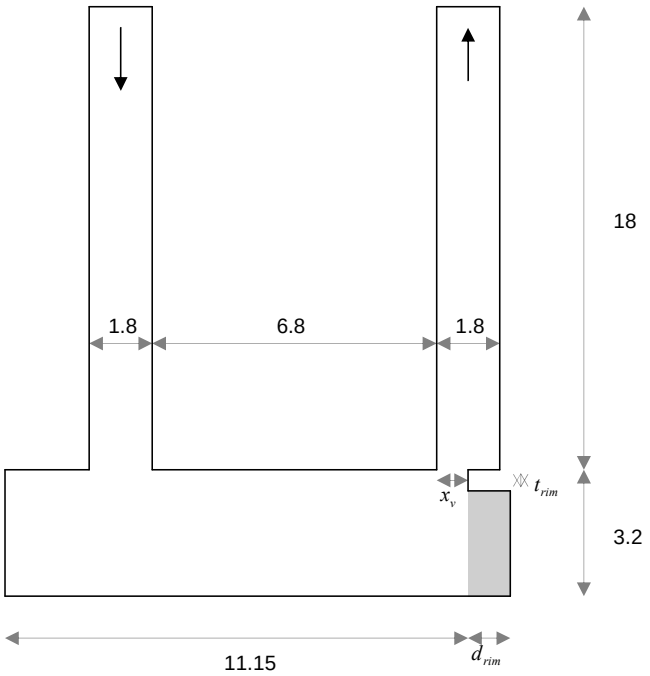

Figure 4.15: Schematic of the model geometry of a rim spool valve. All dimensions are in mm

The rim thickness and inside depth were 0.6 and 1.8 mm, respectively. Simulations were done using CFX 5.6 for four geometries corresponding to spool displacements of x_v = 0.35, 0.5, 0.75 and 1.05 mm. The same simulation conditions (fluid properties, boundary conditions) used for the standard spool valve were also used for these simulations.

4.9.2 Describing the Flow Field (Rim Spool Valve)

In this section, results for a spool opening of 0.5 mm are presented, while the results for other openings are contained in section 3 of Appendix F.

Figure 4.16 shows the velocity vector plot of the flow through the rim valve for a meter – out orifice. (Similar plots for the meter–in orifice or inflow condition are shown in section 2 of Appendix F).

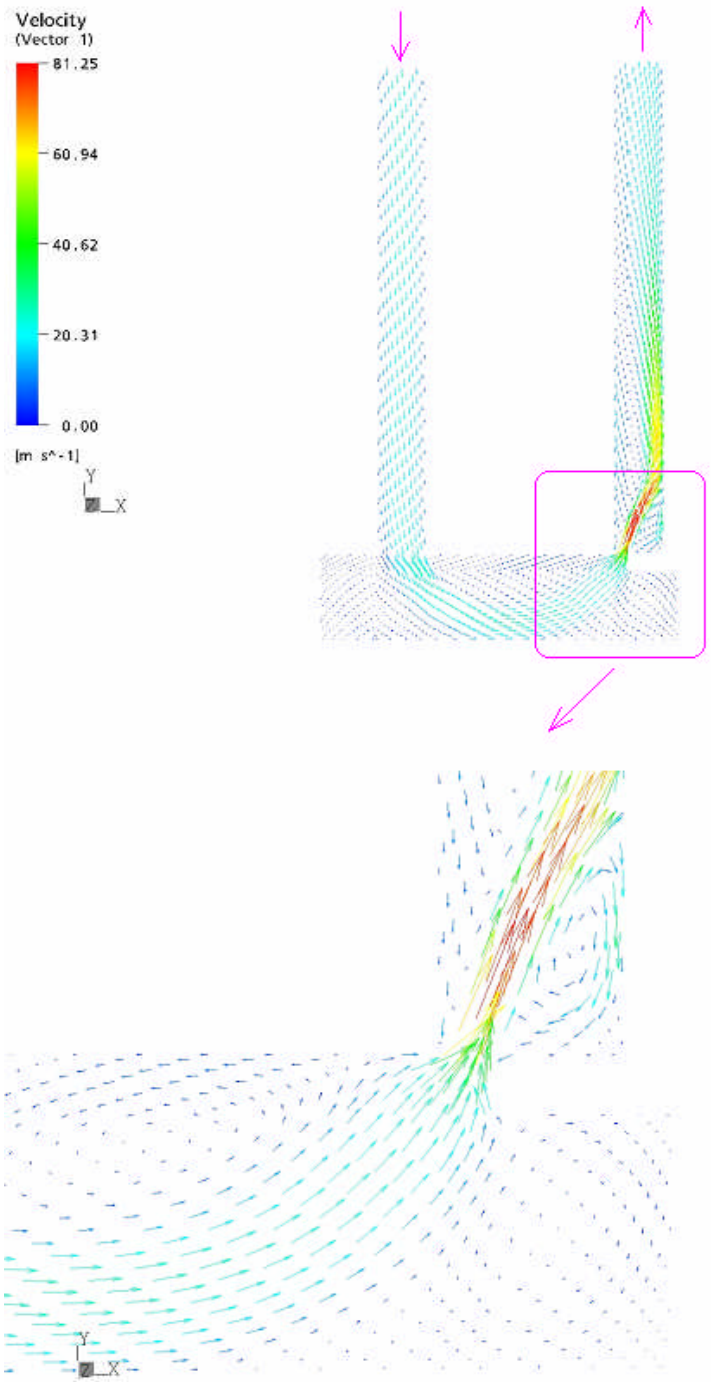

Figure 4.16: Velocity vectors for the rim spool valve configuration (t_{rim} = 0.8 mm, x_v = 0.5 mm). The estimated jet angle from the CFD analysis is 66.46^0

The plot indicates similar flow characteristics to that of Figure 4.5 for the standard spool configuration; however, there are some differences in the valve spool land area because of the cavity introduced by the rim where the fluid re-circulates as shown by Figure 4.16.

Figure 4.17 shows the pressure contour plots for the rim spool for a meter – out orifice. As indicated by Figure 4.16, the jet angle at which the fluid discharges at the metering orifice is steeper (larger) when compared to the standard spool configuration. The consequence is that as the angle increases, flow forces decrease as predicted by the SSFF equation 2.4.

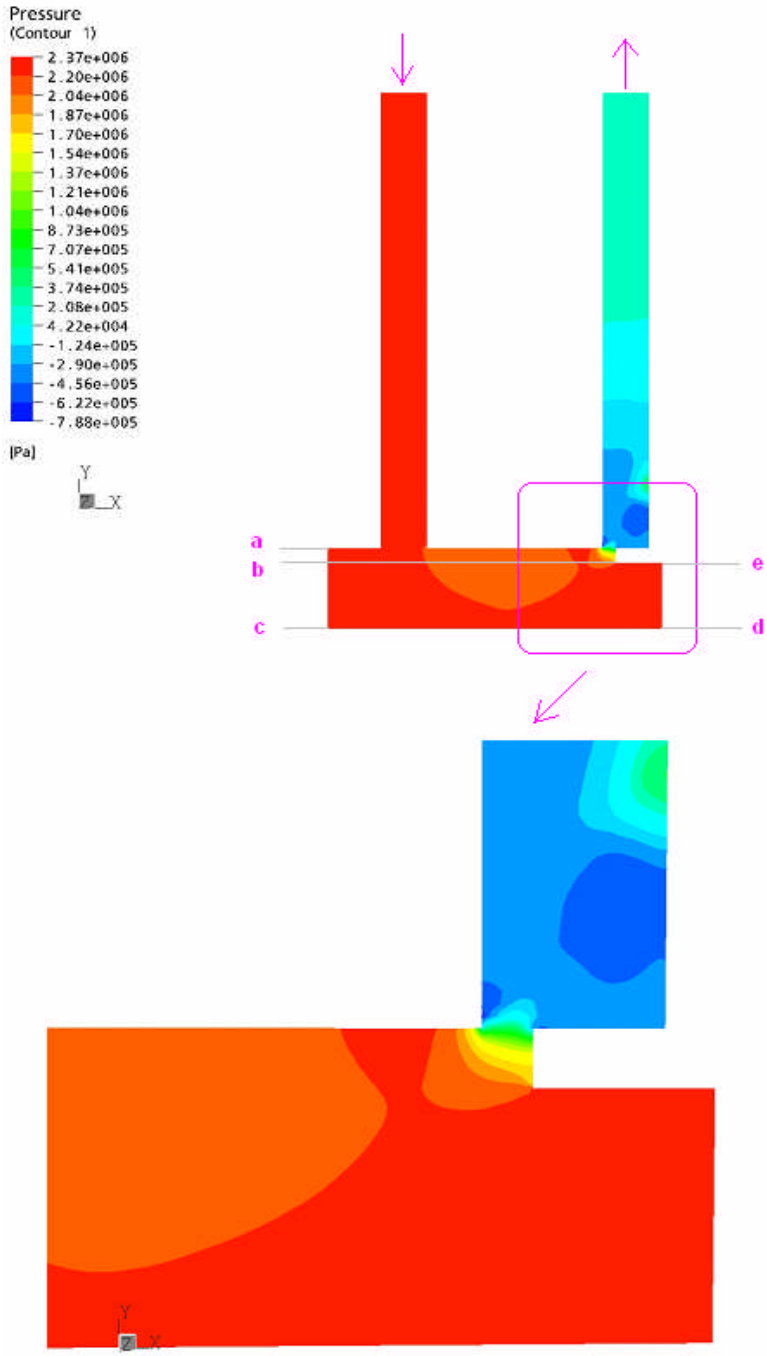

Figure 4.17: Pressure contours for the rim spool valve configuration (t_{rim} = 0.8 mm, x_v = 0.5 mm). The estimated steady state flow forces from the CFD analysis is 4.82 N

From Figure 4.17, the pressure distribution on surface *d–e* is approximately equal to that on surface *b-c*. Therefore, the SSFF is the difference between the pressures acting on faces *a–b* and the small surface area of the rim, where there is large pressure gradient. Thus, the effectiveness of the rim spool valve depends on the rim thickness; the smaller the thickness of the rim, the more SSFF reduction.

Using the same technique as was discussed for the standard spool land, the SSFF and the measured fluid jet angles were evaluated and are summarized in Table 4. 6. It is evident that the jet angle is not constant as is often assumed, but increases with orifice opening.

Table 4.6: The estimated jet angle, TSSFF and SSFF from CFD analysis for rim spool land (rim thickness t_{rim} = 0.8 mm)

			CFD (Rim)			
$x_v(mm)$	$A_o(m^2)$	$Q(m^3/s)$	$\theta_{cfd2}(°)$	TSSFF (N)	SSFF (N)	Viscous Force (N)
0	0	0	0	0	0	0
0.375	3.37 e -6	2.02 e -4	65.85	4.46	4.42	0.0452
0.5	4.50 e -6	2.78 e -4	66.46	4.82	4.76	0.0612
0.75	6.74 e -6	4.50 e -4	71.62	7.06	6.96	0.1017
1.05	9.44 e -6	7.50 e -4	73.49	9.64	9.51	0.1319

4.9.3 Comparison of TSSFF and Fluid Jet Angle for Standard and Rim Spool Valve

One of the objectives of this study was to determine whether the rim spool valve was successful in reducing the TSSFF as claimed by Chan et al (6). In order to do this, values of the TSSFF for the standard spool valve obtained from CFX 5.6 were compared to that of the rim spool valve for the same flow conditions. The results are summarized in Table 4.7.

Table 4.7: The estimated jet angle and TSSFF from CFD analysis for standard and rim spool land (rim thickness t_{rim} = 0.8 mm)

	CFD (Standard)		**CFD (Rim)**	
$x_v\,(mm)$	θ_{cfd1}(°)	TSSFF (N)	θ_{cfd2}(°)	TSSFF (N)
0	0	0	0	0
0.375	65.34	4.66	65.85	4.46
0.5	65.54	6.24	66.46	4.82
0.75	66.21	9.56	71.62	7.06
1.05	69.25	13.10	73.49	9.64

For a constant rim thickness (t_{rim} = 0.8 mm), the TSSFF are reduced by approximately 25 % for spool positions greater than 0.5 mm. For very small displacements, the pressure gradient is localized around the opening and rim area, whereas for larger openings the pressure distribution is more distributed on the metering orifice land face. The jet angle also increased for the rimmed land. The control volume analysis done in Chapter 2 indicated that the steeper (larger) the jet angle, the smaller the SSFF, and this was substantiated by the rim spool geometry.

It was also of interest to demonstrate how the rimmed lands performed when the thickness was increased to 1 mm. The results are summarized in Table 4.8 and it is evident that there was very little flow force reduction at this thickness. This result is consistent with that predicted by Chan et al. (6).

Table 4.8: The estimated jet angle and TSSFF from CFD analysis for standard spool and rimmed land (t_{rim} = 1 mm)

	CFD (Standard)		**CFD (Rim)**	
$x_v(mm)$	$\theta_{cfd1}(°)$	TSSFF (N)	$\theta_{cfd2}(°)$	TSSFF (N)
0	0	0	0	0
0.375	65.34	4.66	65.65	4.64
0.5	65.54	6.24	65.86	6.26
0.75	66.21	9.56	66.59	9.29
1.05	69.25	13.10	69.62	12.28

4.9.4 Discussion

In this section, a reason as to why the jet angle increased for the rimmed land shall be presented, which will provide a physical explanation as to why the thin rim spool land was successful in reducing the TSSFF. For the rim spool valve, the average fluid jet angle was larger than for the standard spool valve because the longitudinal momentum flux at the metering orifice was less for the rim spool configuration than for the standard spool. The longitudinal flux term in the x direction $F_{\Omega x}$, is calculated as:

$$F_{\Omega x} = \iint_A \rho \vec{V}_x \vec{V}.ndA = \rho Q V_o \cos\theta \qquad (4.7)$$

For the same spool opening, ρ, Q and V_o are the same; hence equation (4.2) implies that for a smaller $F_{\Omega x}$, θ must be greater. In CFX 5.6, there is a built-in function to calculate fluxes. Using this function, the values for the longitudinal momentum flux for the standard and the rim spool valve for each opening of the spool were calculated and are presented in Table 4.9.

Table 4.9: The longitudinal momentum flux for both the Standard and Rim spool valve with rim thickness of 0.8 mm

	Longitudinal flux $F_{\Omega x}$	
$x_v(mm)$	Standard Valve	Rim valve
0	0	0
0.375	4.36	4.24
0.5	5.8	5.39
0.75	10.11	7.89
1.05	15.38	11.75

From the table, it is seen that the flux is consistently lower for the rim spool land.

4.9.5 Comparison of SSFF for the Standard and Rim Spool Valve (Inflow Condition)

Often, in valve operation, the flow through the orifice can be both in a meter-in (inflow or reversed flow) and meter-out (outflow) configuration. In the meter-in flow condition, the variable orifice meters flow into the valve chamber. The SSFF will also act as to close the valve. Table 4.10 presents a comparison of SSFF for the standard and rim spool valve configurations for the inflow conditions. These results are based on the CFX 5.6 simulation results and do not include friction effects.

Table 4.10: The SSFF for both the Standard and Rim spool valve with a rim thickness of 0.8 mm for a meter–in orifice

	SSFF (Inflow condition)	
$x_v(mm)$	Standard (N)	Rim (N)
0	0	0
0.375	3.21	2.97
0.5	6.14	5.29
0.75	7.82	7.71

Table 4.10, indicates that the rim spool does not effectively compensate for SSFF for the inflow or meter–in condition. In addition, a comparison of the results shown in Tables 4.10 and 4.5 indicate that for either the standard land or the rimmed land, the flow forces for identical operating conditions in the meter-in case are not equal to those for the meter-out case. As stated earlier, this is contrary to what is predicted using the classical formulation for flow reaction forces for the standard valve.

4.10 Further Modification to the Rim Spool Valve

The CFD analysis indicates that the rim spool modification reduces the SSFF, but the effectiveness does depend on the rim thickness. Also the SSFF compensation technique of the rim appears to be only suitable for a meter-out orifice configuration. Using CFX 5.6 as a design and simulation tool, a novel spool land configuration called the "sharp edge tapered rim" was conceptualized to further reduce the flow reaction forces. This configuration is now considered.

4.10.1 Sharp Edge Tapered Rim Spool Valve

The sharp edge tapered rim spool valve incorporated a modification of the rim and a new port adjustment to compensate for SSFF. CFD results have shown that for flow entering

or leaving the valve chamber, the shape of the land face and port influenced the angle at which the fluid jet entered or exited the port, which relates to the SSFF. By modifying the land face and the port, as illustrated in Figure 4.18, the jet angle can be changed.

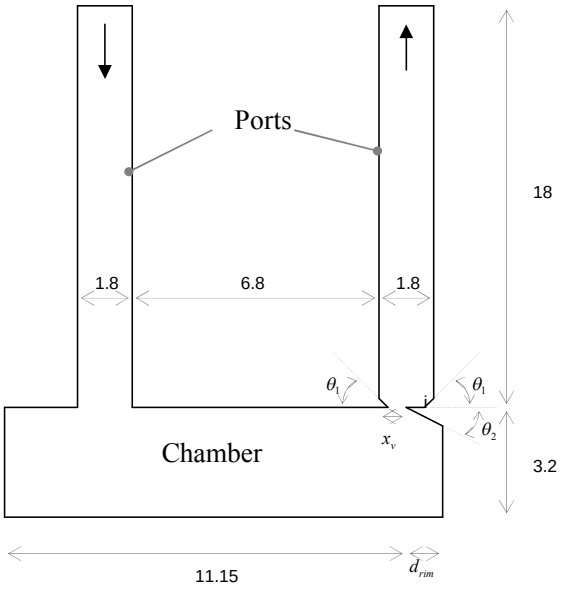

Figure 4.18: Schematic of the sharp edge tapered rim geometry

The inclusion of the sharp edge tapered rim in the valve design eliminates the dependence of the rim valve on the rim thickness. The tip of the tapered rim effectively creates a sharp edge orifice at the metering – section, thereby causing the fluid to exit at nearly $90°$. The inclination (defined by the two θ_1's) at the base of the port, which provide for the port adjustment, forces the fluid to enter the chamber at a larger jet angle, thereby reducing the SSFF for an inflow condition. For this configuration, SSFF are reduced by increasing the jet angle at which the fluid enters/leaves the valve chamber. This approach is very effective irrespective of the metering strategy as long as θ_1 and θ_2 are appropriately chosen.

The new geometry was meshed in CFX – Build. The tapered rim depth was 1.8 mm in length; θ_1 and θ_2 were set to be $52°$ and $18°$, respectively, from the spool axis. Simulations were run for four geometries corresponding to spool displacements of x_v = 0.35, 0.5, 0.75 and 1.05 mm. The same simulation conditions (fluid properties, boundary conditions) used for the standard and rim spool lands were also used for these simulations.

The results of the simulations are presented in terms of velocity vector and pressure contour plots in Figures 4.19 and 4.20. By comparing the velocity vector plot of Figure 4.19 for the sharp edge tapered rim spool valve with the standard spool valve (Figure 4.4) and the rim spool valve (Figure 4.16), substantial differences are evident in the flow angles. In the sharp edge tapered rim spool valve configuration, the fluid is discharged at $80.77°$.

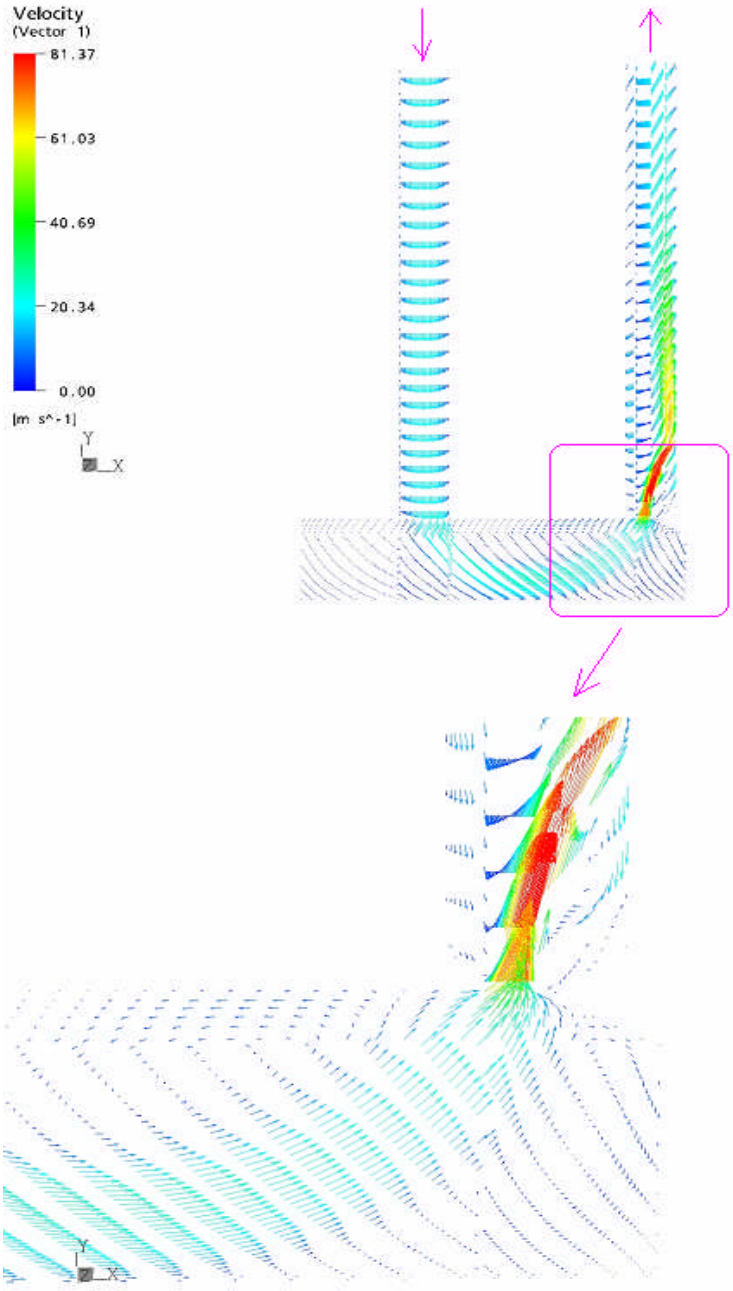

Figure 4.19: Velocity vectors for the sharp edge tapered rim spool valve configuration ($\theta_1 = 52°, \theta_2 = 18°$ and x_v = 0.5 mm) for outflow condition. The estimated jet angle from the CFD analysis is 80.77^0

Also from the pressure contour plot of Figure 4.20, it is seen that the pressure on both land faces are almost the same, as no pressure gradient exists on the right land face near the metering section. For the rim spool valve, the pressure plot of Figure 4.20 indicated a pressure gradient on the small rim surface area.

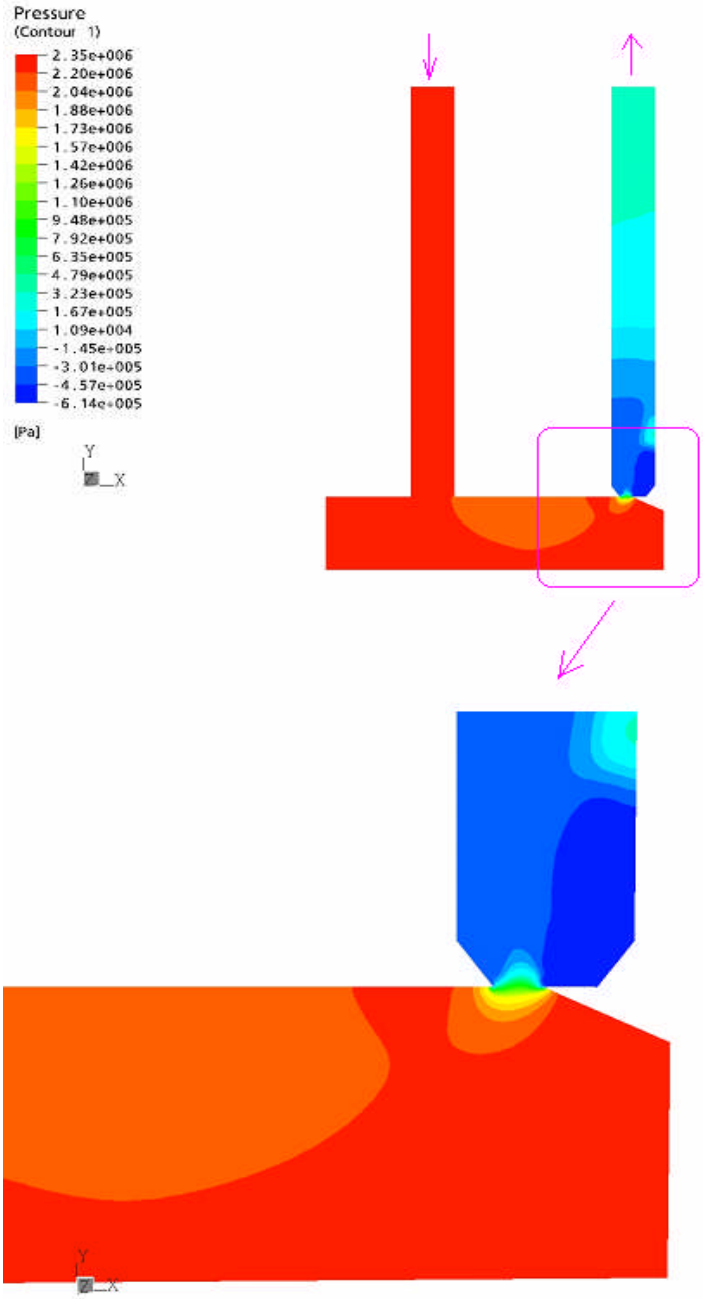

Figure 4.20: Pressure contours for the sharp edge tapered rim spool valve configuration ($\theta_1 = 52°, \theta_2 = 18°$ and $x_v = 0.5$ mm) for the outflow condition. The estimated steady state flow forces from the CFD analysis is 1.49 N

The results for the SSFF and jet angles for the tapered rim as well as the standard and rim configurations for the meter-out condition are summarized in Table 4.11 and are shown graphically as a function of the spool displacement in Figure 4.21. The results for the SSFF of the different valve configurations for the inflow condition are presented in Table 4.12. Again, the sharp edge tapered rim valve configuration provided the best compensation for SSFF.

Table 4. 11: The estimated jet angle and SSFF from CFD analysis for the standard, rim spool land (rim thickness t_{rim} = 0.8 mm) and the sharp edge tapered rim (outflow condition)

	Standard		**Rim**		**Sharp Edge Tapered Rim**	
$x_v\,(mm)$	$\theta_{std}\,(°)$	SSFF (N)	$\theta_{rim}\,(°)$	SSFF (N)	$\theta_{str}\,(°)$	SSFF (N)
0	0	0	0	0	0	0
0.375	65.34	4.62	65.65	4.42	80.5	1.03
0.5	65.54	6.18	65.86	4.76	80.77	1.49
0.75	66.21	9.47	66.59	6.96	82.25	2.32
1.05	69.25	12.97	69.62	9.51	84.65	2.28

Table 4.12: The SSFF for the Standard, Rim ($t_{rim,}$ = 0.8 mm) and Sharp edge tapered rim (inflow condition)

	SSFF (Inflow condition)		
$x_v\,(mm)$	Standard (N)	Rim (N)	Tapered (N)
0	0	0	0.0
0.375	3.21	2.97	0.6
0.5	6.14	5.29	0.6
0.75	7.82	7.71	0.6

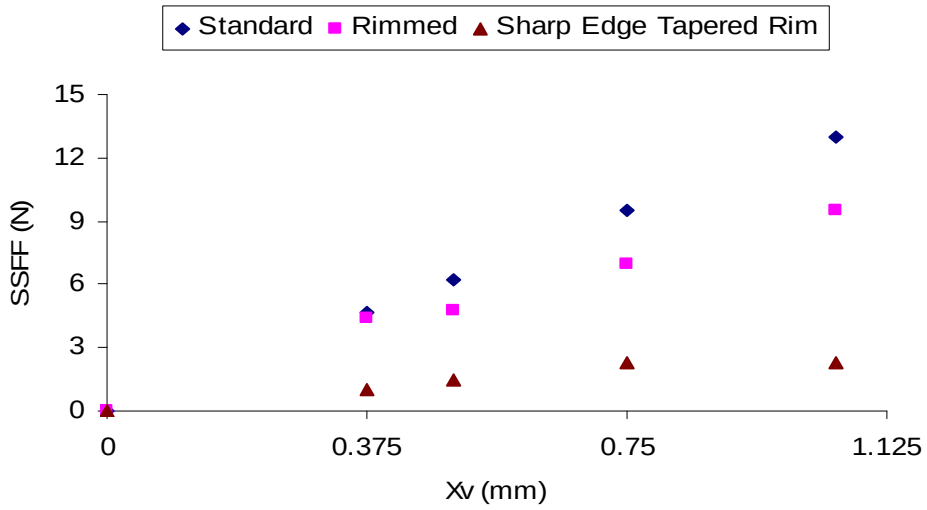

Figure 4.21: Plot of SSFF for different spool openings for the outflow condition

The percentage reduction in SSFF for the two compensation configurations is summarized in Table 4.13. For either inflow or outflow conditions, the sharp edge

tapered rim offers the best compensation for all openings of the spool. At a spool opening of 0.75 mm, the SSFF values saturate for the sharp edge tapered rim spool valve. Beyond the spool opening of 0.75 mm, the SSFF does not increase further when the spool opening was larger. The reduction in SSFF is also presented in Figure 4.22.

Table 4.13: Percentage reduction of TSSFF by the Rim and Sharp Edge Tapered Rim compared to the Standard land Spool (Outflow condition)

	Std	Rim	Sharp Tapered	**% reduction in SSFF**	
$x_v\,(mm)$	SSFF (N)	SSFF (N)	SSFF (N)	Rim valve	Sharp Tapered Rim
0	0	0	0	0	0
0.375	4.62	4.42	1.03	4.4	77.7
0.5	6.18	4.76	1.49	23.0	75.9
0.75	9.47	6.96	2.32	26.5	74.3
1.05	12.97	9.51	2.28	26.7	82.4

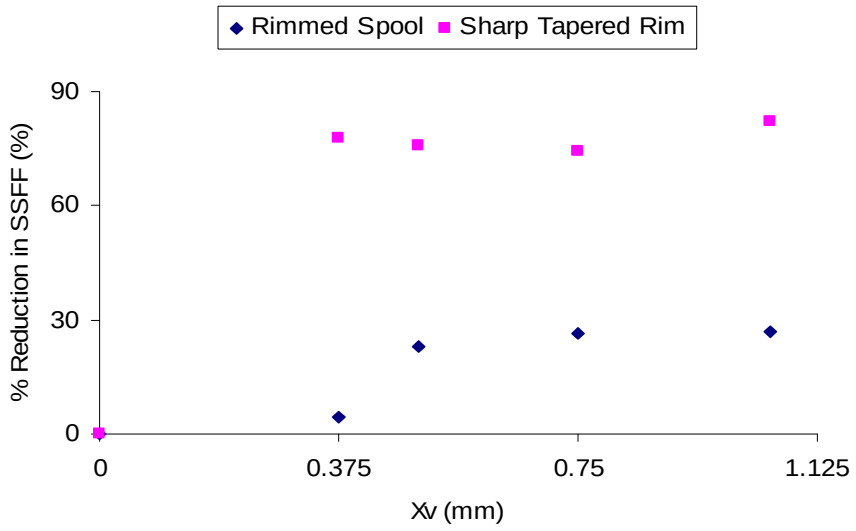

Figure 4.22: Plot showing the % reduction in SSFF for the outflow condition

4.11 Summary

In this section, CFD simulations were carried out to analyze the flow conditions inside a 2D model of a hydraulic spool valve. The numerical model was implemented in CFX 5.6 using the finite volume method (FVM).

Three configurations of the spool were considered: standard, rim and sharp tapered rim spool lands. The rim and the sharp tapered rim were specially designed geometrical changes to the lands in order to reduce the large SSFF inherent in the standard spool valve. For all openings of the spool, the sharp tapered rim valve provides the largest reduction in SSFF.

It was also observed that for all cases studied, the inflow SSFF's were smaller than for the outflow conditions.

Chapter 5

Application of CFD to a Rimmed Flow Divider Valve

The CFD approach was applied to the flow divider valve configuration introduced by Chan et al. (6, 7 and 8). This required an iterative and coupled approach, because the valve spool displacement (solved using Matlab/Simulink®) depended on the calculated flow reaction forces (solved using CFD techniques), which in turn depended on the spool position. Using this iterative procedure, the flow reaction forces and the flow dividing error were evaluated for the rimmed spool and the results are summarized below.

5.1 Model and Governing Equations of the Flow Divider Valve

A schematic of Chan's flow divider valve with a rim is shown in Figure 5.1. The geometry is assumed to imply "zero" net flow force The valve without the rim and its associated dimensions are given in Appendix G1. A flow divider valve is used to divide a single stream of fluid Q_s (see Figure 1.3) at some pressure P_s into two portions Q_1 and Q_2 at a predetermined ratio irrespective of the operating load pressures P_{L1} and P_{L2}. In Chan's (and subsequently, this) study, a 50 – 50 flow division was considered. The valve was designed such that the efflux jet angles θ_1 and θ_2 approached $90°$. The spool regulates the amount of flow to the load ports based on the force balance on the spool. For identical load pressures (i.e. $P_{L1} = P_{L2}$) and for zero net flow forces, the pressure drop across the fixed orifices A_1 and A_2 are the same, such that the intermediates pressures P_{i1} and P_{i2} are equal. Therefore,

$$P_{i1} - P_{i2} = 0 \qquad (5.1)$$

When this occurs, the flow across the fixed orifices is equal and hence the flow to the two loads (in the absence of leakage) is equal.

$$Q_1 - Q_2 = 0 \qquad (5.2)$$

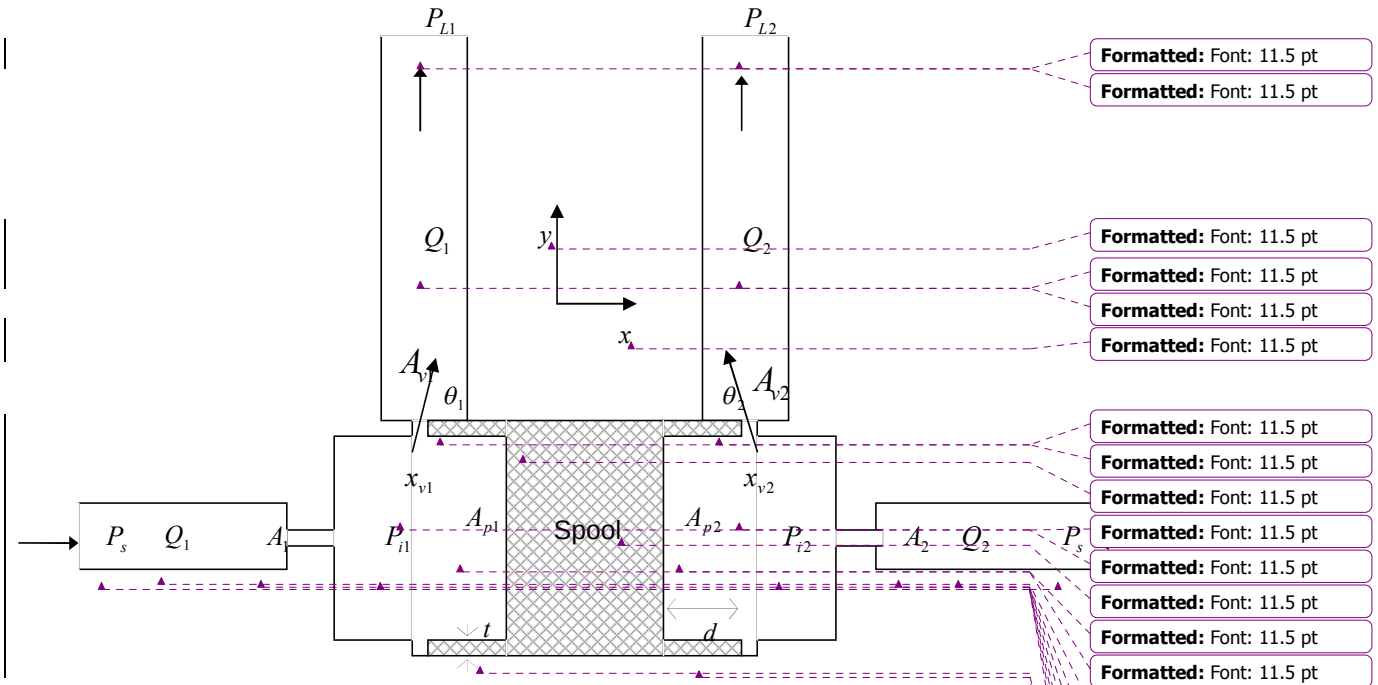

Figure 5.1: Schematic of a flow divider valve with the rim (6)

If there are flow reaction forces, Equation (5.1) is not valid in that the net flow forces F_f acts as a spring force on the piston ($P_{i1} - P_{i2} = \frac{F_f}{A_p}$) and hence for a steady-state force

balance, P_{i1} is not equal to P_{i2}. Q_1 and Q_2 are no longer equal and (referring to Figure 5.1) are given as;

$$Q_1 = A_1 K_1 \sqrt{(P_s - P_{i1})} \tag{5.3}$$

$$Q_1 = A_{v1} K_1 \sqrt{(P_{i1} - P_{L1})} \tag{5.4}$$

$$Q_2 = A_2 K_2 \sqrt{(P_s - P_{i2})} \tag{5.5}$$

$$Q_2 = A_{v2} K_2 \sqrt{(P_{i2} - P_{L2})} \tag{5.6}$$

and $$K_1 = K_2 = C_d \sqrt{\frac{2}{\rho}} \tag{5.7}$$

To demonstrate how the valve operates, assume the valve is in steady state conditions and hence is not moving. Assume that the load pressure in one of the ports, for example P_{L2}, increases with respect to its previous steady state value. Flow through the variable orifice A_{v2} temporarily decreases as does flow through the fixed orifice A_2 (see equations (5.5) and (5.6)). This can only happen if the intermediate pressure P_{i2} also increases. This, however, results in a force imbalance across the spool which, in turn, causes the spool to be displaced toward the negative *x* direction (Figure 5.1). As this happens, the variable orifice x_{v2} increases (subsequently P_{i2} decreases) and x_{v1} decreases (P_{i1} increases). The spool will continue to move until a new equilibrium is re-established (i.e. $P_{i1} - P_{i2} = \frac{F_f}{A_p}$).

As stated above, because of the flow reaction force (including friction forces), F_f, P_{i1} is not identical to P_{i2}, and thus equal flow division is not possible. The magnitude of the pressure in the left chamber P_{i1} depends on the area of the orifices A_1 and A_{v1}. Similarly, the same condition is true for the pressure in the right hand chamber. The difference

between the two load flows gives rise to the term " flow dividing error" and is defined in (6) and given as;

$$\%E_{ss} = \frac{Q_1 - Q_2}{Q_1 + Q_2} = \frac{Q_1 - Q_2}{Q_S} \tag{5.8}$$

Consider the spool shown in Figure 5.1. The force balance across the spool is given as,

$$P_{i1}A_{p1} + F_{f1} - P_{i2}A_{p2} - F_{f2} = m\ddot{x} + B\dot{x} + F_{fc} \tag{5.9}$$

where A_{pi} is the spool area surface *i,* F_{f_i} is the flow reaction forces on surface *i* (where *i* could be "1" or "2" and 1 refers to port 1 and 2 refers to port 2), F_{fc} is the frictional force which includes the static and Coulomb friction, m is the mass of the spool, and $\ddot{x}$, $\dot{x}$ are the acceleration and velocity of the spool, respectively. It should be noted that flow reaction forces act in a direction so as to close the valve such that on one side the force is positive and on the other, it is negative. From Chapter 2, the classical form of the flow force equation was given as:

$$F_{f1} = 2C_d A_{v1}\left(P_{i1} - P_{l1}\right)\cos\theta_1 \tag{5.10}$$

$$F_{f2} = 2C_d A_{v2}\left(P_{i2} - P_{l2}\right)\cos\theta_2 \tag{5.11}$$

where

$$A_{v1} = x_{v1}w \quad ; \quad A_{v2} = x_{v2}w \quad A_p = A_{p1} = A_{p2} \tag{5.12}$$

A_{vi} is the variable orifice area *i* , x_{vi} is the displacement of orifice *i* from its initial steady state point, and w is the area gradient (Merritt, 1967) which is equal to the depth of the flow domain. For the valve considered, the maximum opening of each variable orifice

was 0.004 m (see Figure 5.2). When the spool was exactly centered (6), $x_{v1} = x_{v2} = 0.002m$.

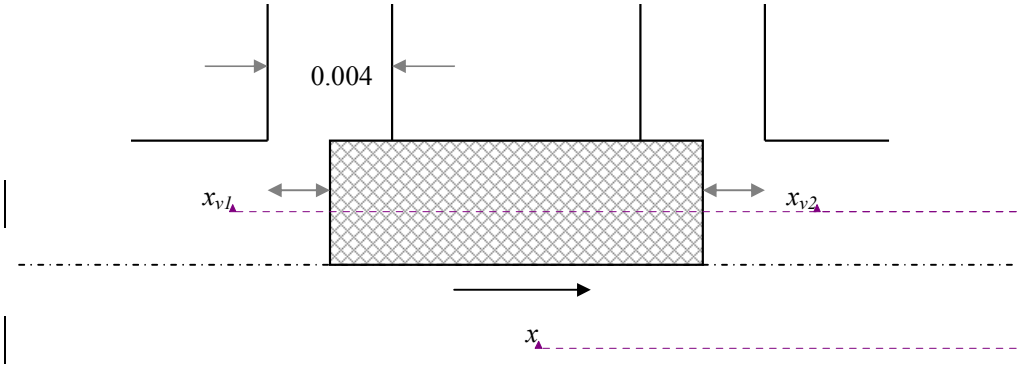

Figure 5.2: The relative spool position

Hence,

$$x_{v1} = x + 0.002 \quad ; \quad x_{v2} = 0.002 - x \quad ; \quad x_{v1} + x_{v2} = 0.004 \qquad (5.13)$$

Equations (5.3) to (5.7) and (5.9) to (5.13) are the dynamic equations which, when solved, will yield Q_1 and Q_2 for any load combination P_{L1} and P_{L2}. In order to solve these equations, a switch is made from static to dynamic analysis.

For this study, the equations were solved using a commercial program called Matlab/Simulink®. Simulink is a graphical user interface (GUI) of Matlab that allows the user to simulate a system by simply connecting the necessary "icons" together to construct the block diagram. The Simulink models and the model parameters are contained in Sections 2 and 3 of Appendix G.

For this simulation, it was assumed that the input supply pressure P_s ($3.45MPa$), and the load pressures ($P_{L1} = 1.2MPa$, $P_{L2} = 2.4MPa$) were constant. The dynamic model was studied using the Dormand – Prince 45 ordinary differential equation solver of Matlab. The discrete fixed step size was 0.001seconds, and the simulation time was set at 0.5 seconds.

Formatted: Font: (Default) Times New Roman, 12 pt, Complex Script Font: Times New Roman, Subscript

Formatted: Font: (Default) Times New Roman, 12 pt, Complex Script Font: Times New Roman, Subscript

Formatted: Font: (Default) Times New Roman, 12 pt, Complex Script Font: Times New Roman, 12 pt

The geometry for the CFD model is shown in Figure 5.1. The depth and hence flow areas were matched in both the dynamic and CFD models. The inputs to the dynamic model were defined as the boundary conditions for the CFD model. The flow reaction forces in the CFD model were estimated by calculating the net pressure force acting on faces A_{p1} and A_{p2}.

CFX 5.6 software solves for the pressure and flow for a given geometry. However, in this study the actual final geometry were not known because the spool position was dependent on the flow reaction forces, which, in turn, was not known because the geometry was, dependent on the spool position. Thus the solution involved an iterative process using both the dynamic model and the CFD software. The iterative process began by assuming jet angles (θ_1 and θ_2) for the dynamic model in order to estimate the spool position (x_{v1} and x_{v2}). These values for x_{v1} and x_{v2} were used to generate the CFD model to obtain the new jet angles θ_1' and θ_2', which were then substituted back in the dynamic model to determine the new spool position x_{v1}' and x_{v2}'. The iterative process was terminated when the values for subsequent θ_1''s and θ_2''s did not vary with successive iterations. This process was repeated 8 times to achieve an acceptable solution.

The following considerations were taken into account in order to compare the results from both models:

- In the dynamic simulation, the results were only taken after steady state conditions were reached.
- Sliding frictional effects were neglected. Chan's experimental results indicated that friction was present on the spool but because no value for friction was specified, friction effects were ignored in the dynamic model.

5.2 Simulation Results

The results obtained from the dynamic and CFD models will be presented in this section.

5.2.1 Results from the Dynamic Model

Figure 5.3 shows the simulated spool position determined from the dynamic model simulation after the iteration process was completed. The difference in the spool position for the valve without the rim versus the rim valve is due to the magnitude of flow forces F_{f_i} for the two valve configurations. For the rim case, the value of the flow forces was reduced as expected, and hence the spool required a smaller displacement in x to re-establish equilibrium. These spool positions were subsequently used for the final CFD model

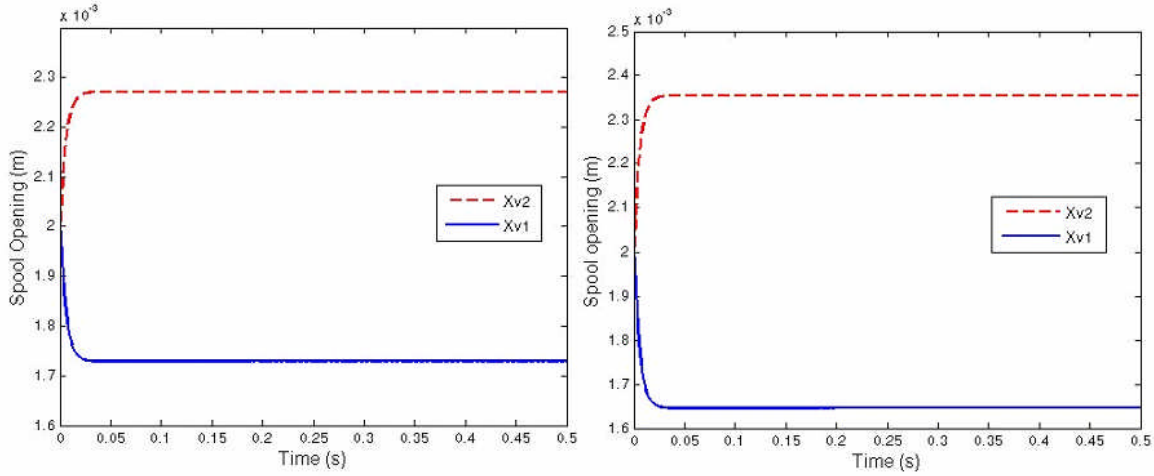

(a) Without rim (WOR) (b) With rim(WR)

Figure 5.3: Spool positioning of the flow divider valve (simulated from the dynamic valve)

Figures 5.4 and 5.5 show the dynamic model pressure in the two chambers for the spool WOR and WR, respectively. The pressures P_s, P_{L1} and P_{L2} are inputs to the system simulation. For both valve configurations, it is observed that the pressure drop ($P_s - P_{i1}$) and ($P_s - P_{i2}$) across the fixed orifices A_1 and A_2 are not the same because of the difference in load pressures P_{L1} and P_{L2} (which resulted in a difference in A_{v1} and A_{v2}).

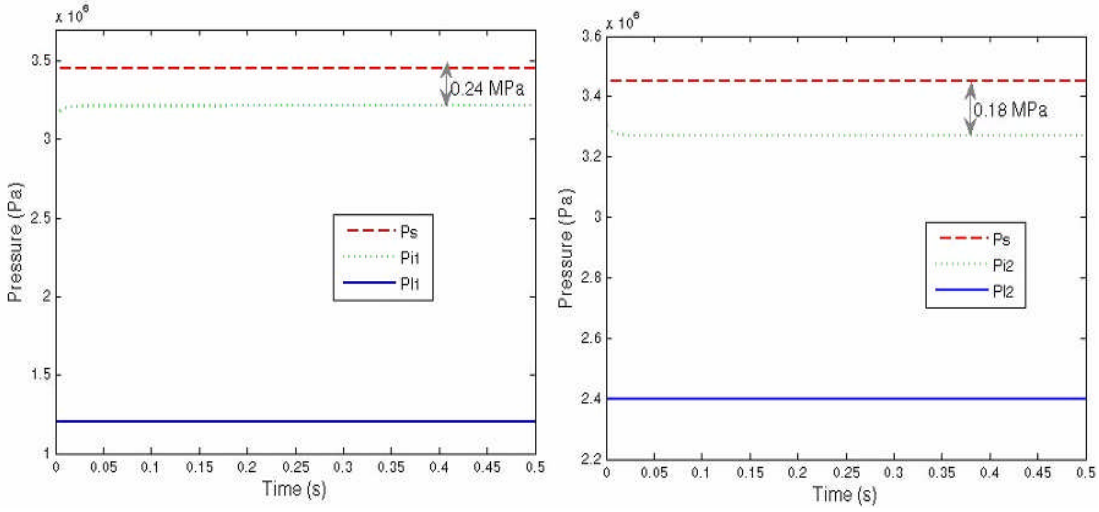

(a) LH *(P_{L1}, P_{i1})* (b) RH *(P_{L2}, P_{i2})*

Figure 5.4: Pressure plot (dynamic model) for the flow divider valve without the rim

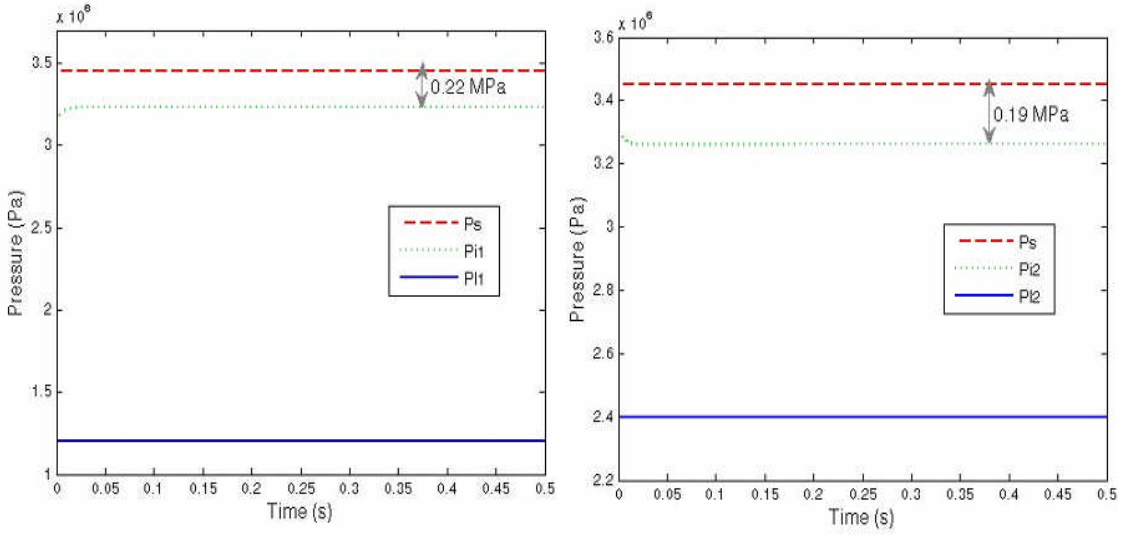

(a) LH (P_{L1}, P_{i1}) (b) RH (P_{L2}, P_{i2})

Figure 5.5: Pressure plot (dynamic model) for the flow divider valve with the rim

Figure 5.6 shows the divided flow rates Q_1 and Q_2 to each of the loads for the spool configurations with and without the rim. For both valve configurations, the flow through the right hand passage Q_2 (reference, Figure 5.1) is slightly larger because of the wider orifice opening caused by the increase in load pressure P_{l2} . The difference in the flow rates accounted for a flow dividing error of 7.3 % for the case without the rim case and 3.5 % for the case with the rim. Thus, the percentage reduction in flow dividing error with the inclusion of the rim in the valve geometry is approximately 53 %.

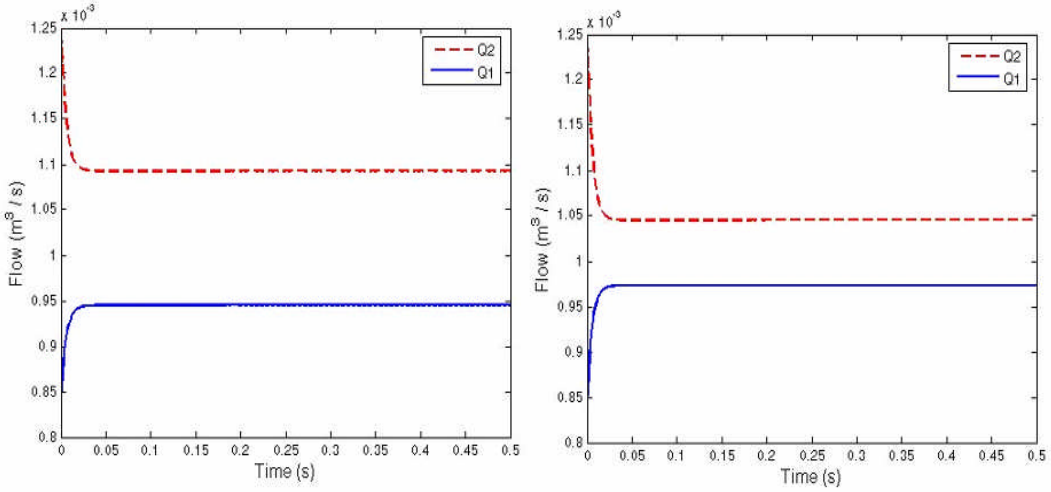

(a) Without rim (b) With rim

Figure 5.6: Load flow rates through the flow divider valve

Figure 5.7 shows the dynamic model flow force values for the valve configuration without the rim and with the rim included. For the condition without the rim, the net flow force value was 2.26 *N*, while the inclusion of the rim reduced the net force value to 1.09 *N*, thereby giving a percentage reduction of 52 %. It is noted that this reduction in flow force is close to the reduction in flow dividing error (53 %).

Recall at this point that the flow reaction forces calculated from the dynamic model were, in part, determined by the CFD simulations in that the jet stream angles used in equation (6.5) were obtained from the CFD plots using the technique discussed in Chapter 4. This will explain why in Figure 5.7, the flow reaction force, $F_{fl,}$ on the left hand side of the spool land face (Figure 5.1) was very small since the observed jet stream angles for both the spool with the rim and the spool without the rim at this orifice were close to 90^{o}.

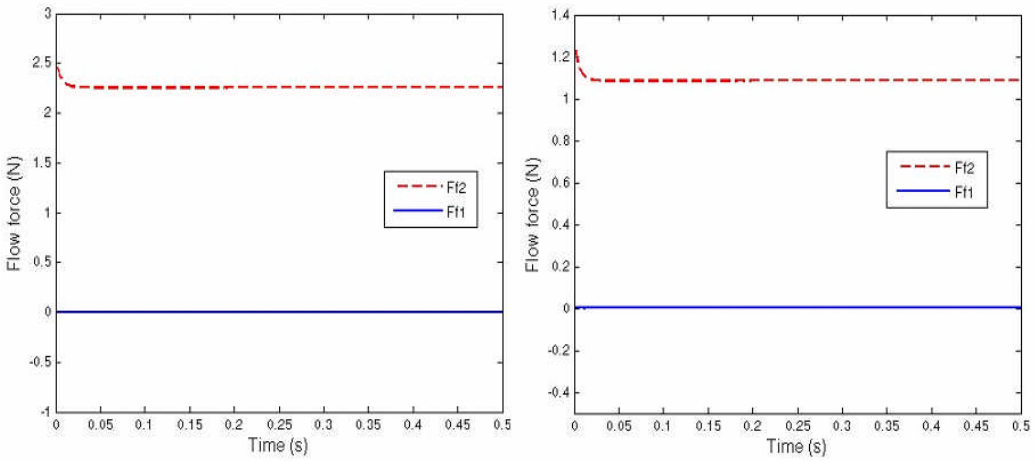

(a) Without rim (b) With rim

Figure 5.7: Flow forces on the flow dividing valve

5.2.2 CFD Model

Figures 5.8 and 5.9 show typical velocity and pressure values for the spool with and without the rim. The results for this case is best presented in contours. The downstream and upstream pressures were set to be the same as that in the dynamic simulation. At steady state conditions, the orifice areas between the chambers and the exit ports are observed to be different. For the valve without the rim, the jets from the inlet orifices (A_1 *and* A_2) to the chambers impinge directly on the faces A_{p1} and A_{p2}. As the jets leave the variable orifices (A_{v1} and A_{v2}), the jets attach to the LH port. For the spool with the rim, however, the jets from the inlet orifices do not impinge on the spool faces, but instead curve upward to travel through the restrictions (A_{v1} *and* A_{v2}), and then attach to the RH port. As a result, the two pressure forces acting on the spool faces are different. For the CFD model the flow reactions forces were evaluated by integrating the pressure profile along the spool surface.

In the WOR and WR cases, the smaller flow restriction area on the left side is a consequence of the larger pressure drop across the variable orifice (x_{v1}).

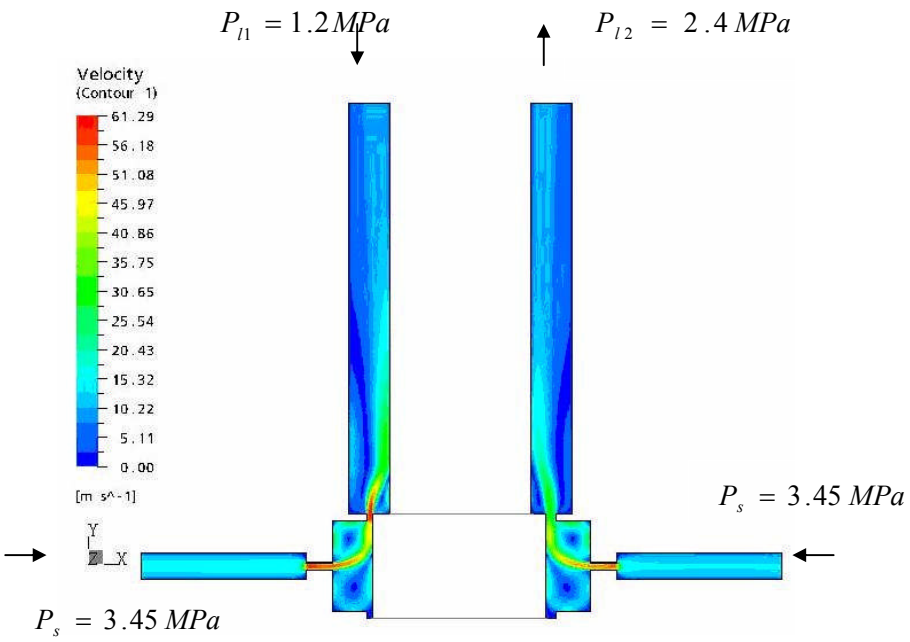

Figure 5.8.1: Velocity contours for the flow dividing valve WOR (x_{v1} = 0.174 cm; x_{v2} = 0.226 cm)

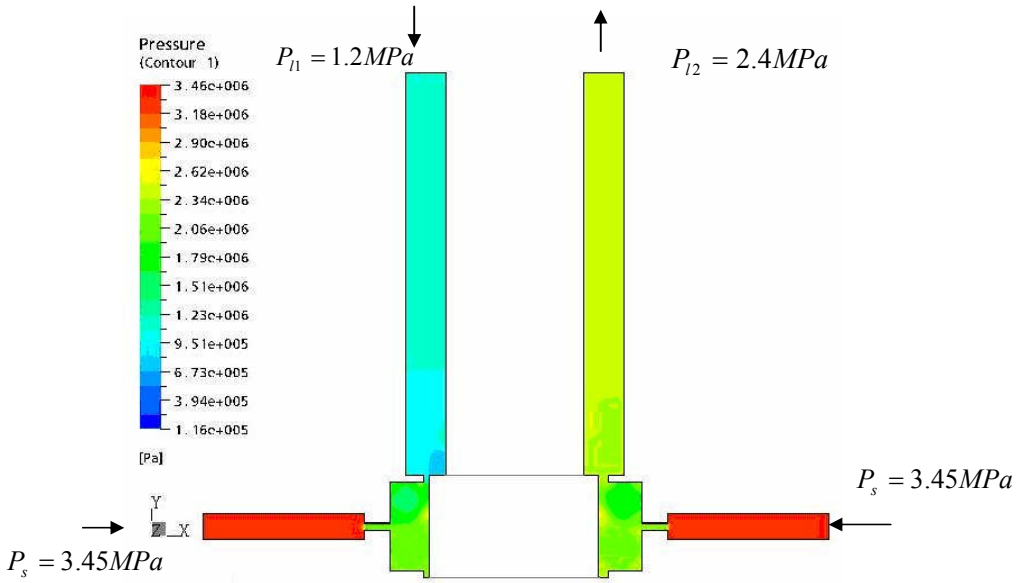

Figure 5.8.2: Pressure contours for the flow dividing valve WOR (x_{v1} = 0.174 cm; x_{v2} = 0.226 cm)

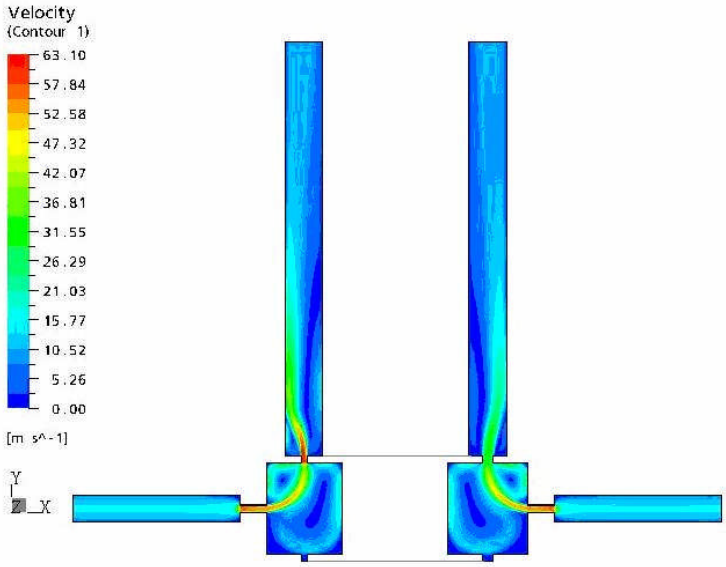

Figure 5.9.1: Velocity contours for the flow dividing valve WR (x_{v1} = 0.164 cm; x_{v2} = 0.236 cm)

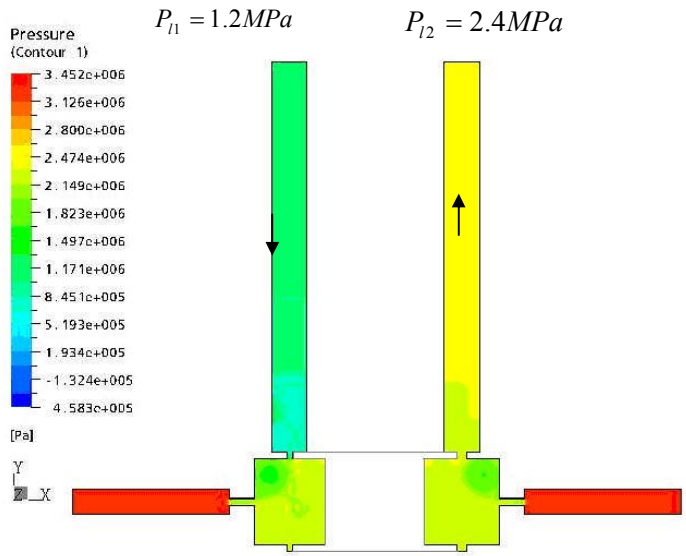

Figure 5.9.2: Pressure contours for the flow dividing valve WR (x_{v1} = 0.164 cm; x_{v2} = 0.236 cm)

The flow forces calculated from the CFD plots for the two cases are compared in Table 5.1. The results are presented for a pressure drop of 1.2 MPa across the load ports. At steady state conditions, the percentage reduction in flow reaction forces from the CFD simulation was calculated to be approximately 70% compared to 50% obtained from the dynamic flow simulation. These results are consistent with the trends obtained experimentally in Chan's work. Further, it must be pointed out that the values for the flow forces obtained from the CFD results are higher than those obtained from the dynamic model. This result is consistent with those presented in Table 4.4, in which the SSFF values from the CFD results were higher than those obtained using the classical equation even when the efflux jet angles from CFD simulation were used in the classical equation.

Table 5.1: Flow forces and jet stream angle for the flow divider valve (pressure differential across the ports of 1.2 MPa and rim thickness of 0.16 mm)

$x(cm)$	$x_{v1}(cm)$	$x_{v2}(cm)$	$\theta_1(^\circ)$	$\theta_2(^\circ)$	$F_f(N)$	Condition
0.06	0.174	0.226	90	88	3.9	WOR
0.04	0.164	0.236	90	89	0.75	WR

Table 5.1, shows that the accuracy of the iteration process depends on the validity of the estimate for discharge angles given that there exists only one degree difference between the two cases. As discussed in section 1 of Appendix F, the estimation of the jet angle followed a process of vector analysis. The process was approximate but consistent and was used to calculate the jet angles for the different positions of the spool.

5.3 Summary

In this chapter, the CFD method has been applied to the flow dividing valve designed by Chan et. Al (6, 7 and 8). The model for the flow dividing valve and the governing equations were presented in section 5.1.The solution procedure required an iterative approach because the actual spool displacement in the valve depended on the calculated flow reaction forces, which in turn depended on the spool position. The dynamic equations were solved using Matlab/ Simulink for assumed jet angles to determine a new steady state position. CFX 5.6 was applied to the new spool position and new jet angles were estimated. The value was then substituted back into the dynamic simulation and a new position calculated. The procedure was repeated 8 times until the change in jet angles became insignificant. The trends showed that the rim did indeed, reduce the flow dividing error and hence, the flow reaction forces. The percentage reduction in the flow reaction forces was in the order of 70 %.

Chapter 6

Conclusions and Recommendations for Future Research

In this chapter, a summary of the results will be presented and suggestions for future research will be made.

6.1 Summary of Accomplishments

As reported in section 1.4, the objectives of this study were (1) to use the CFD tool to present a better understanding of the physics of flow reaction forces, and (2) to study the flow reaction forces on the rimmed spool valve proposed by Chan et al. (6). The specific valve of interest was a flow dividing valve in which a special rim was machined into the spool lands in order to reduce the flow reaction forces and in doing so, reduce the flow dividing error. Since Chan et al. (6) were unable to show explicitly in their studies that the improvement in flow dividing capability was due to a reduction in flow forces, it was of particular interest to use CFD to demonstrate that the rim did reduce these flow forces and to understand how this reduction occurred.

In achieving these objectives, CFD simulations were done for two configurations of the spool, i.e. the standard and the rim spool valve. The numerical results revealed detailed features of the flow field. Flow recirculation is observed at different locations within the flow regions. The modeling results indicated that the rim does reduce flow reaction forces, but the effectiveness of the rim is dependent on the rim thickness. The study was extended to a new configuration of a valvewith a sharp edge tapered rim and contoured port, for which the flow reaction forces were further reduced to or by approximately 70 % , irrespective of the metering strategy. In Chapter 5, an iterative procedure using the CFD method and Matlab/Simulink® was applied to determine the percentage reduction in flow dividing error and flow forces for the flow divider valve. The Simulink model was used to obtain the dynamic behavior of the valve, and was complemented by the information

obtained from CFD simulations. First the simulink model was used to obtain the spool positions using an "assumed" jet angle. The positions in the CFD simulation were then updated to calculate the new jet angles. The SSFF was obtained from the CFD simulations when successive iterations did not produce significant change in the jet angle. The results showed that the reduction in SSFF was in the order of 70 % as was the case in Chan's (6, 7 and 8) valve.

6.2 Conclusions

1. The introduction of the rim to the land of the spool reduces the flow reaction forces for the outflow condition and, only to a very limited extent, the inflow conditions. The percentage reduction for the rim machined into the standard spool land configuration was in the order of 30 %. In all cases, the rim resulted in the jet efflux angle increasing as the reaction forces decreased.
2. Flow reaction forces for inflow and outflow conditions are not the same for standard spool configurations or for the rimmed valve design. The force is greater for the outflow condition. The exception was for the contoured port configuration at the tapered rimmed spool.
3. The sharp edge tapered rim and contoured port could reduce the flow forces of a single land to approximately 70 %, irrespective of the metering strategy (inflow or outflow).
4. The rim proposed by Chan (6, 7 and 8) did result in a reduction of the flow reaction forces, and the presence of a rim in any valve, standard or otherwise, can be a simple and effective way to reduce flow reaction forces for outflow conditions and to a lesser extent, inflow.
5. CFD combined with classical dynamic models is an effective tool to visualize flow and pressure in hydraulic components, and can be used to calculate special properties such as flow forces.

6. The results also showed that the contribution of viscous force is insignificant for this study.

6.3 Contributions

The major contributions of this study relate to the application of CFD to predict flow through a flow dividing valve.

The application of CFD has:

1. Provided a visualization of the flow and pressure patterns in a hydraulic spool valve which give rise to the phenomenon of flow reaction force.
2. Showed that viscous forces that act on the sleeve surfaces can increase (decrease) the net closing forces which exist on a spool.
3. Demonstrated that an iterative approach to using a dynamic model and steady-state CFD program can be used to solve a problem in which the final steady state values are not initially known.
4. Demonstrated that a rim does reduce flow reaction forces
5. Demonstrated that inflow flow forces are less than outflow flow forces, which is contrary to established opinion (1).
6. That the sharp edge tapered rim configuration provides the best configuration for SSFF.

6.4 Future Research

It is important to note that the CFD approach can be extremely useful as a simulation and design tool for hydraulic systems, but attempts should be made to compare CFD results with experimental results. Future research should address the following points:

1. A special experimental test rig to measure the flow reaction forces should be developed to validate the results of the CFD results in order to establish a true benchmark for future studies.
2. The model should be simulated with a dynamic mesh (moving boundary) to allow movement of the spool valve and see how the flow configuration adapts to it.
3. The SSFF values from CFD simulations were different from those obtained using the classical equations (Table 4.4), even when the jet efflux angles obtained from CFD simulation were used in the classical equations. Future research should explore the reason for the difference.
4. The results presented in Table 4.5 are very significant. The pressure profile in Figure 4.16 is substantially more uniform than that shown along the same surface in Figure 4.9 in the region close to the orifice. This means that the differential closing force on the faces of the lands is smaller than for the outflow conditions In the classical approach to flow reaction forces, inflow and outflow SSFF's are assumed to be the same for the same operating conditions. The results in Table 4.5 appear to contradict this assumption and hence this defines an area that needs to be investigated in greater detail in the future.

References

(1) Merritt, H. E. *Hydraulic Control Systems*. John Wiley and Sons, New York, 1967.

(2) Borghi M., Milani M., and Paoluzzi, R., 2002. Stationary Axial Flow Forces Analysis on Compensated Spool Valves. *International Journal of Fluid Power*, Vol. 1, No.1, pp. 13-22

(3) Bao, M. Fu, X., and Chen, Y., 2001. Computational Fluid Dynamic Approach to Pressure Loss Analysis of Hydraulic Spool Valve. *Proceedings of the 5th International Conference on Fluid Power, Transmission and Control*, Hangzhou, China.

(4) Jyh-Chyang Renn and Tien-Chis Kao., 2003. Application of CFD to Designing a Power-Saving Hydraulic Directional Two–Land–Four-Way Valve, *Proceedings of the First International Conference on Computational Methods in Fluid Power Technology*, Monash, Australia, Paper No. 08.

(5) Finke, M., and Becher, D., 2004. Product Design and Testing at Moog: Turning High Performance into Reality.*www.moog.com*

(6) Chan R, Schoenau G, and Burton R., 1981.A Simple Design Modification for Improved Accuracy of Piston Type Flow Divider Valves. *Proceedings of the 35th Conference on Fluid Power*, October, Chicago.

(7) Burton R.T., Chan R.K. and. Schoenau, G.J, 1979. Mathematical Model for Predicting the Steady State Flow Dividing Error of a Piston-Type Flow-Divider Valve. *Proceedings of the 35th National Conference on Fluid Power,* November, Chicago, Illinois.

(8) Burton, R.T. Schoenau, G.J. and Chan, R.J., 1980. A Single Stage Precision Flow Divider Valve. *Proceedings of the 36th National Conference on Fluid Power*, October, Cleveland, Ohio, pp 61-65.

(9) Wang, L., Shao, X., Ruan, X., Song, X., Yamamoto, F. 1997 PIV Measurement of Flow Field in Spool Valve Chamber, *Proceedings of the 4th International Conference on Fluid Power Transmission and Control (ICFP),* pp 42-45.

(10) Gao, D., 2004, Investigation of Flow Structure inside Spool Valve with FEM and PIV Methods, International Journal of Fluid Power, Vol. 5, No 1, pp 51-66

(11) Linda, T. and Glen, W. 2002. Application of Computational Fluid Dynamics (CFD) Anylsis in improving Valve Design, Transactions of the SAE, International Off-Highway & Powerplant Congress, March 2002, Las Vegas, NV, USA, Paper Series. 2002-01-1397,

(12) Vescovo, G. and Lipolis, A., 2003(a). CFD Analysis of Flow Forces on Spool Valves, *Proceedings of the First International Conference on Computational Methods in Fluid Power Technology*, Paper no 29 Nov., Monash, Australia.

(13) Vescovo, G. and Lipolis, A., 2003(b). Three – Dimensional Analysis of Flow Forces on Directional Control Valves. International Journal of Fluid Power, Vol 4, No 2, July

(14) Yuan, Q., and Li., P., 2002(a). An experimental Study on the use of Unstable Electrohydraulic Valves for Control, Proceedings of the American Control Conference Anchorage, Alaska. Vol. 6, pp 4843-4848

(15) Yuan, Q., and Li., P., 2002(b). Modelling and Experimental Study of Flow Forces for Unstable Valve Design, *America Society of Mechanical Engineering*, *Fluid Systems Technology Division Publication FPST.* Vol 10. pp 29-38

(16) Menter F. R., 1994. Two – equation eddy – viscosity turbulence models for engineering applications. *AIAA – Journal*, 32(8), pp.269-289.

(17) AEA Technology, 2001. CFX – 5 Documentation.

(18) Matlab/Simulink. Matlab Help. The Mathworks, Natick, MA. 2002.

(19) Okungbowa, N., Bergstrom, D. J., Burton, R. T., 2005. Determining the Steady State Flow Forces in a Rimmed Spool Valve using CFD Approaches. *Proceedings of the Bath Workshop on Power Transmission and Motion Control*. September, University of Bath, UK.

(20) Armaly, B.F., Durst, F., Peireira, J.C. F., Schonung, B., 1983, Experimental and Theoretical Investigation of Backward – Facing Step Flow, J. Fluid Mech., 127, pp. 473 – 496.

(21) Biswas, G., Breuer, M, Durst, F., 2004, Backward Facing Step Flows for Various Expansion Ratios at Low and Moderate Reynolds Numbers, J. Fluid Mech., vol 126, pp.362 – 374,.

(22) Patankar S. V., Numerical Heat Transfer and Fluid Flow, McGraw Hill, New York, 1980.

(23) Harlow F. H., Welch J. E., Numerical Calculations of Time Dependent Viscous Incompressible Flow of Fluid with a Free Surface, Physics of Fluids, 8:2182, 1965.

(24) Ferziger J. H., Peric M., Computational Methods for Fluid Dynamics, Springer, 2002.

(25) Munson, B. R., Young, D. F., Okiishi, T. F., Fundamentals of Fluid Mechanics, John Wiley and Sons, New York, 4th Edition, 2002.

(26) Blackburn, J. F., Reethof, G., Shearer, L. L., Fluid Power Control, MIT Press, 1960.

(27) Manring, N. D. *Hydraulic Control Systems*. John Wiley and Sons, New York, 2005.

Appendix A

Modeling Steady Flow Forces (Lumped Parameter Approach)

In this section, the intent is to develop models for steady state flow forces that consider viscosity under certain widely used assumptions which were used to facilitate the analysis. In a typical valve configuration such as that shown in Figure 2.2, there are two chambers; one metering-out flow (chamber 1) and the other metering-in flow (chamber 2). The steady state flow force models will be derived for both cases, namely; outflow and inflow conditions. The analysis for the steady state flow force model for a metering-out valve shall be presented in Section 1 of the Appendix A while the case of a metering-in valve shall be contained in Section 2 of Appendix A.

A.1 Basic Assumptions

(1) Flow is two dimensional (2D). This implies that the flow variables depend on two spatial coordinates; to approximate this, it is assumed that the axial length of the orifice is small compared to its peripheral width.

(2) Flow is steady and so the time dependency of the flow is neglected.

(3) Flow is incompressible which means, the fluid density is constant ($\beta \to \infty$ where β is the fluid Bulk modulus)

(4) Flow is viscous; therefore, the effect of viscosity is taken into account

(5) Fluid is Newtonian; there is a simple linear relationship between the shear stress and shear strain rate.

(6) Turbulent flow occurs across all orifices

It is also assumed that the valve has the following characteristics;

(7) Valve is matched (symmetric) and critically lapped and there is no clearance between the spool lands and the valve sleeve; thus, there is no leakage flow across the orifice

(8) Equal lands area; therefore, $A_1 = A_2 = A_3 = A$

(8) Flow geometry is symmetric, thus analysis can be done for half part of the valve

A1.1 Outflow Condition

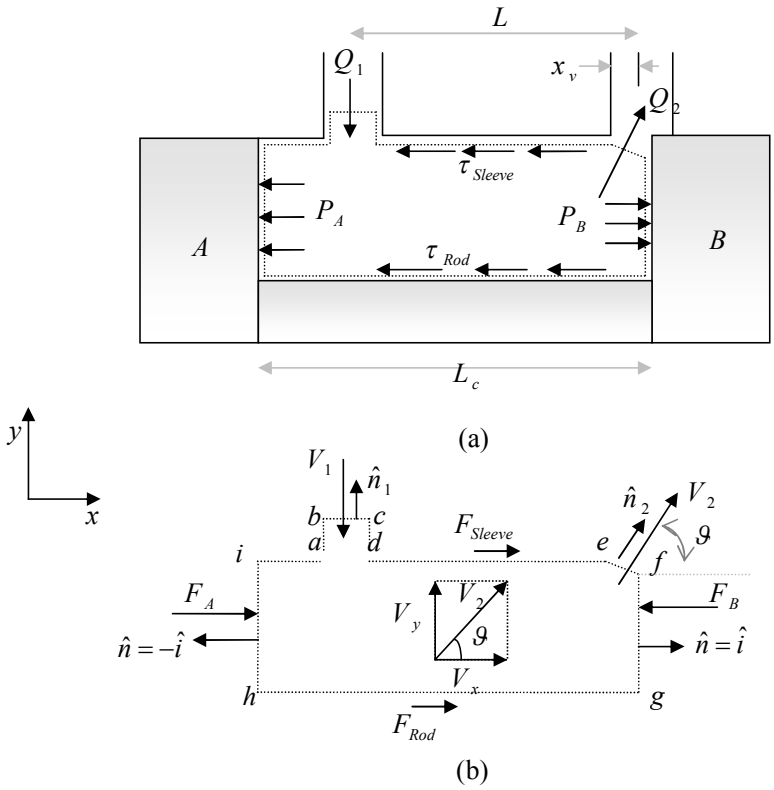

Figure A1. 1: Schematic of the fluid control volume for a metering–out valve chamber

Figure A1.1 shows a schematic of the control volume which consists of the valve chamber. Fluid enters the control volume at velocity V_1 and exits at V_2 at an angle given as θ. The pressure acting on the land faces are represented appropriately as P_A and P_B. The shearing stresses acting on the sleeve and rod surfaces are represented respectively by τ_{Sleeve} and τ_{Rod}. The dimension L_c is the full length of the chamber and L is the length between the inlet and the outlet of the chamber. L is called the damping length and the valve opening is given by the dimension x_v.

Consider Figure A1.1. The control volume is defined as (*a-b-c-d-e-f-g-h-i*) for a metering – out valve chamber. The spool consists of the two lands (A and B) and the rod.

The force on the spool is given by;

$$\vec{F}_{Spool} = \vec{F}_{Lands} + \vec{F}_{Rod} \quad . \tag{A1.1}$$

Equation (A1.1) is the force that the spool experienced from the fluid and it is equal to the sum of the net pressure forces on the lands and the rod.

Generally, for the sign convention adopted in Figure A1.1, equation (A1.1) can be expressed as;

$$\vec{F}_{Spool} = -\iint_{A(Lands)} P\hat{n}dA + \iint_{A(Rod)} \tau_{Rod}\, dA \ , \tag{A1.2}$$

where P is the pressure acting on the appropriate land face and τ_{rod} is the shear stress acting along the rod surface area. The first term of the *RHS* of equation (A1.2) represents the resultant axial pressure force on the spool lands, and the second term is the shearing force on the spool rod. Equation (A1.2) does <u>not</u> assume a uniform pressure and shear stress distribution on the lands and rod surfaces respectively.

If, for instance, it is assumed that the pressure on the appropriate land faces are uniform (i.e. for ease of analysis), the resultant axial pressure forces (first term of equation A1.2) can be given as;

$$-\iint_{A} P\hat{n}dA = -P_A A(-\hat{i}) - P_B A(\hat{i}) = A(P_A - P_B) \ , \tag{A1.3}$$

where the unit normal $\hat{n}$ associated with the pressure is assigned positive in the positive coordinate direction and negative in the negative coordinate direction.

Figure A1.1b shows the reaction forces that the spool and sleeve walls exert on the fluid inside the control volume. By applying the momentum equations in the x – coordinate direction to the fluid inside the fixed control volume;

$$\underbrace{\iiint_{\forall} \rho \vec{g} d\forall}_{Body\ \ Force} - \underbrace{\vec{F}_{Spool} - \vec{F}_{Sleeve} + \vec{R}}_{Surface\ \ Forces} = \underbrace{\frac{d}{dt}\iiint_{\forall} \rho \vec{V}_x d\forall}_{} + \underbrace{\iint_{A} \rho \vec{V}_x \vec{V}.\hat{n} dA}_{Flux} \quad . \tag{A1.4}$$

The integrand $\vec{V}.\hat{n}dA$ represents the volume flow rate through the differential area dA and $\rho\vec{V}.\hat{n}dA$ is the mass flow rate through dA. Furthermore, the sign of the dot product $\vec{V}.\hat{n}$ is positive for flow out of the control volume and negative for flow into the control volume. This is shown in Figure A1.1a.

The L.H.S of equation (A1.4) accounts for the total force acting on the control volume and it includes the body and surface forces. The R.H.S is the sum of the rate of change of momentum and the net momentum flux out of the control volume.

To evaluate equation (A1.4), the following assumptions are made;

(i) Body forces are neglected since only horizontal forces are considered.

(ii) The reaction force, $\vec{R} = 0$ (Since the control volume does not cut across any solid material, the control volume is all fluid).

(iii) Since steady flow is assumed, therefore $\frac{d}{dt}\iiint_{\forall} \rho \vec{V}_x d\forall = 0$

Also, the force acting on the sleeve wall can be expressed as;

$$\vec{F}_{Sleeve} = \iint_{A(Sleeve)} \tau_{Sleeve} dA \tag{A1.5}$$

Thus, substituting equation (1.2) into equation (A1.4) becomes;

$$\vec{F}_{Spool} = -\underbrace{\iint_{A} \rho \vec{V}_x \vec{V} . \hat{n} dA}_{Flux} - \iint_{A(Sleeve)} \tau_{Sleeve} dA \tag{A1.6}$$

Equation (A1.5) states that the force on the spool is balanced by the momentum flux and the viscous force acting on the sleeve wall.

By applying the assumption of a Newtonian fluid, the second term of equation (A1.6) is given as;

$$\vec{F}_{Spool} = -\underbrace{\iint_{A} \rho \vec{V}_x \vec{V} . \hat{n} dA}_{Flux} - \iint_{A(Sleeve)} \mu \frac{\partial V_x}{\partial y} dA \tag{A1.7}$$

Since there is no leakage, only the inlet and outlet surfaces have flux across them. Thus the flux term is evaluated as;

$$\iint_{A} \rho \vec{V}_x \vec{V} . \hat{n} dA = \iint_{A(inlet)} \rho \vec{V}_x \vec{V} . \hat{n} dA + \iint_{A(outlet)} \rho \vec{V}_x \vec{V} . \hat{n} dA \tag{A1.8}$$

Also, if it is assume that the fluid enters the valve chamber perpendicular to the spool axis i.e. 90^o, then the inlet flux is neglected (as $V_y = V_2 \cos \vartheta = 0$).

If the fluid leaves the chamber at a vena contracta[2] (not illustrated in FigureA1.1) with a uniform velocity V_2, at an angle θ, then equation (A1.7) becomes:

[2] As the stream of fluid approaches the orifice, the flow lines converge strongly and the average velocity increases greatly. The area at which the jet of fluid attained its maximum velocity is called the vena contracta.

$$\iint_{A} \rho \vec{V}_x \vec{V}.\hat{n}dA = \iint_{A(outlet)} \rho \underbrace{\vec{V}_2 \cos\vartheta}_{V_x} \underbrace{\vec{V}.(i)dA}_{Q} = \rho \vec{V}_2 Q \cos\vartheta \qquad \text{(A1.9)}$$

Substituting equation (A1.8) into equation (A1.6);

$$\vec{F}_{Spool} = -\underbrace{\rho \vec{V}_2 Q \cos\vartheta}_{Flux} - \iint_{A(Sleeve)} \mu \frac{\partial V_x}{\partial y} dA \qquad \text{(A1.10)}$$

But

$$V_2 = \frac{Q}{A_c} = \frac{Q}{C_c A_o} \approx \frac{Q}{C_D A_o} \qquad \text{(A1.11)}$$

Assuming $C_c = C_D$ (since the orifice opening is small compared to the port diameter, the flow and pressure equations obey the Bernoulli's principle) and substituting equation (A1.11) into equation (A1.10) yields;

$$\iint_{A} \rho \vec{V}_x \vec{V}.\hat{n}dA = \frac{\rho Q}{C_D A_O} \cos\vartheta \qquad \text{(A1.12)}$$

To evaluate the second term of equation (A1.6), the following assumptions are made:

(a) The fluid in the chamber is laminar and Newtonian.

(b) The flow in the chamber is fully developed; therefore the velocity profile is constant.

(c) The fluid only flows reasonably between the dimension L such that at other region in the chamber, the fluid is at a dead zone, where the fluid is not moving.

Using the above assumptions, the second term of equation (A1.6) will reduce to the analytical solution for steady laminar flow between two fixed parallel plates as shown in equation (B23) of Appendix B. From equation (B23), the viscous force can be evaluated by knowledge of the flow rate Q, the dynamic viscosity μ and the geometrical dimensions; the gap width h and the damping length L. However, the weakness of this formulation is that the value of the shearing force at the sleeve wall will be the same as the shearing force on the rod surface since the same h separates them. This is not exactly correct. Also, for higher flow rate, the flow may become turbulent in the chamber, in which case, the assumption of laminar flow becomes invalid. The Reynolds Average Navier – Stokes (RANS) equations must be used to approximate turbulence. The shear stresses will now consist of the Reynolds stress tensor which results from the averaging procedure and this makes the analytical solution to the flow problem impossible. The only way this can be resolved is by the doing experiments or using CFD simulations. Performing experiments may be an uphill task as it is almost impossible to install sensors and transducer to a valve body as it operates. Also, introduction of sensors could change the flow dynamics. Some researchers like Wang (2002) and Gao (2004) have used PIV experiments to map the flow field of a valve chamber. However, since PIV required that the fluid must be transparent, they (Gao, 2004) used water as the fluid which does not represent hydraulic fluid. Based on these arguments, CFD techniques become the best choice to analyze the flow through a valve chamber.

Thus, the steady flow force equation is now given as:

$$\vec{F}_{Spool} = -\left(\underbrace{\frac{\rho Q^2}{C_D A_o} \cos\vartheta}_{Flux} + \iint_{A(Sleeve)} \mu \frac{\partial V_x}{\partial y} dA \right) \tag{A1.13}$$

In order to relate the flow rate, Q, to the spool opening, x_v, the classical orifice equation can be applied. The orifice equation states that, for any given pressure drop across the valve, the flow rate Q, is proportional to the orifice opening x_v and the square root of the pressure drop.

$$Q = C_D A_O \sqrt{\frac{2\Delta P}{\rho}} \tag{A1.14}$$

where C_D is assumed to be a constant value of *0.62* (Merritt 1967). Substituting equation (A1.14) into equation (A1.13) yields;

$$\vec{F}_{spool} = -\left(2C_D A_o \Delta P \cos\vartheta + \iint_{A(sleeve)} \mu \frac{\partial V_x}{\partial y} dA \right) \tag{A1.15}$$

The negative sign in the equations (i.e. equations A1.12 and A1.15) for flow force models implied that the force, $\vec{F}_{Spool}$ is acting in the opposite direction to what was assumed (i.e. towards the left). This means that the Steady Flow Force is always acting in the direction as to close the valve.

In most fluid power applications, the viscosity contribution to the steady state reaction force is neglected (Merritt 1967), that is;

$$\vec{F}_{spool} = -\left(2C_D C_v A_o \Delta P \cos\vartheta\right) \tag{A1.16}$$

where again, all variables are define as before, and C_v is the velocity coefficient and it is usually assumed to be 1.

A1.2 Inflow Condition

Similarly, the same analysis can be performed for a meter – in valve chamber .Again, consider the control volume *(a-b-c-d-e-f-g-h-i)* as showed in Figure A2.1.

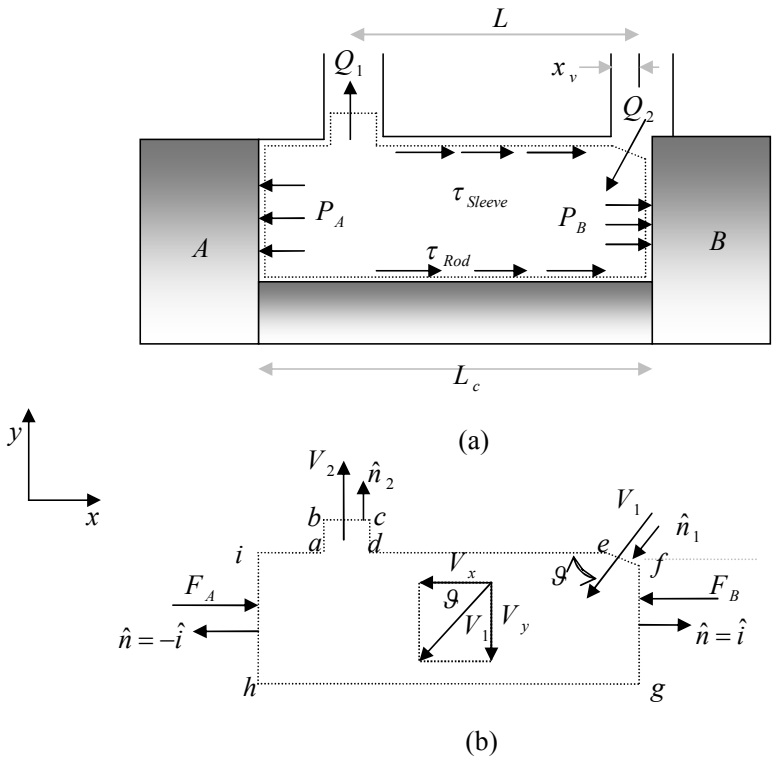

Figure A2. 1: Schematic of the fluid control volume for metering–in valve chamber

The force on the spool is given by;

$$\vec{F}_{Spool} = \vec{F}_{Lands} + \vec{F}_{Rod} \qquad \text{(A2.1)}$$

Again, equation (A2.2) does not assume a uniform pressure and shear stress distribution on the lands and rod surfaces respectively.

Generally, for the sign convention adopted in Figure A2.1, equation (A2.1) can be expressed as;

$$\vec{F}_{Spool} = -\iint_{A(Lands)} P\hat{n}dA + \iint_{A(Rod)} \tau_{Rod}\, dA \qquad \text{(A2.2)}$$

where the nomenclature was described in the above section..

If for instance, it is assume that the pressure on the appropriate land faces are uniform (for easy analysis), the resultant axial pressure forces (first term of equation A2.2) can be given as;

$$-\iint_{A} P\hat{n}dA = -P_A A(\hat{i}) - P_B A(-\hat{i}) = A(P_B - P_A) \qquad \text{(A2.3)}$$

where the unit normal $\hat{n}$ associated with the pressure is assigned positive in the positive coordinate direction and negative in the negative coordinate direction.

Figure A2.1b shows the reaction forces that the spool and sleeve walls exert on the fluid inside the control volume. By applying the momentum equations in the x – coordinate direction to the fluid inside the fixed control volume;

$$\underbrace{\iiint_{\forall} \rho\vec{g}d\forall}_{Body\ \ Force} - \underbrace{\vec{F}_{Spool} - \vec{F}_{Sleeve} + \vec{R}}_{Surface\ \ Forces} = \underbrace{\frac{d}{dt}\iiint_{\forall} \rho\vec{V}_x d\forall}_{} + \underbrace{\iint_{A} \rho\vec{V}_x\vec{V}.\hat{n}dA}_{Flux} \qquad \text{(A2.4)}$$

The integrand $\vec{V}.\hat{n}dA$ represents the volume flow rate through the differential area dA and $\rho\vec{V}.\hat{n}dA$ is the mass flow rate through dA. Furthermore, the sign of the dot product $\vec{V}.\hat{n}$ is positive for flow out of the control volume and negative for flow into the control volume since $\hat{n}$ is considered positive when it points out of the control volume and negative when it points into the control volume. This is shown in Figure A2.1a.

The *L.H.S* of equation (A2.4) accounted for the total force acting on the control volume and it includes the body and surface forces, and the *R.H.S* is the sum of the rate of longitudinal momentum and the net momentum flux out of the control volume.

To evaluate equation (A2.4), the following assumptions are made;

(iv) Body forces are neglected since only horizontal forces are considered.

(v) The reaction force, $\vec{R} = 0$ (Since the control volume does not cut across any solid material – control volume is all fluid).

(vi) Since steady flow is assumed; therefore $\frac{d}{dt}\iiint_{\forall} \rho \vec{V}_x d\forall = 0$

Also, the force acting on the sleeve wall can be expressed as;

$$\vec{F}_{Sleeve} = \iint_{A(Sleeve)} \tau_{Sleeve} dA \qquad \text{(A2.5)}$$

Thus, equation (A2.4) becomes;

$$\vec{F}_{Spool} = -\underbrace{\iint_{A} \rho \vec{V}_x \vec{V}.\hat{n} dA}_{Flux} - \iint_{A(Sleeve)} \tau_{Sleeve} dA \qquad \text{(A2.6)}$$

Equation (A2.6) states that the force on the spool is balanced by the momentum flux and the viscous force acting on the sleeve wall.

By applying the assumption of Newtonian fluid, the second term of equation (A2.6) is given as;

$$\vec{F}_{Spool} = -\underbrace{\iint_{A} \rho \vec{V}_x \vec{V}.\hat{n} dA}_{Flux} - \iint_{A(Sleeve)} \mu \frac{\partial V_x}{\partial y} dA \qquad \text{(A2.7)}$$

Since there is no leakage, only the inlet and outlet surfaces have flux across then. Thus the flux term is resolve as;

$$\iint_{A} \rho \vec{V}_x \vec{V}.\hat{n} dA = \iint_{A(inlet)} \rho \vec{V}_x \vec{V}.\hat{n} dA + \iint_{A(outlet)} \rho \vec{V}_x \vec{V}.\hat{n} dA \qquad \text{(A2.8)}$$

Also, if it is assumed that the fluid enters the valve chamber at a vena contracta with a uniform velocity V_1, at an angle ϑ and leaves the chamber perpendicular to the spool axis i.e. 90^o, then the outlet flux is neglected (as $V_y = V_1 \cos\vartheta = 0$).

Hence equation (A2.8) becomes;

$$\iint_{A} \rho \vec{V}_x \vec{V}.\hat{n} dA = \iint_{A(outlet)} \rho \underbrace{\vec{V}_1 \cos\vartheta}_{V_x} \underbrace{\vec{V}.(-i) dA}_{Q} = -\rho \vec{V}_1 Q \cos\vartheta \qquad \text{(A2.9)}$$

Substituting equation (A2.9) into equation (A2.7), we have;

$$\vec{F}_{Spool} = \underbrace{\rho \vec{V}_1 Q \cos\vartheta}_{Flux} - \iint_{A(Sleeve)} \mu \frac{\partial V_x}{\partial y} dA \qquad \text{(A2.10)}$$

$$V_1 = \frac{Q}{A_c} = \frac{Q}{C_c A_o} \approx \frac{Q}{C_D A_o} \qquad \text{(A2.11)}$$

By substituting equation (A2.11) into equation (A2.10) ;

$$\vec{F}_{Spool} = \underbrace{-\frac{\rho Q^2}{C_D A_o} \cos\vartheta}_{Flux} - \iint_{A(Sleeve)} \mu \frac{\partial V_x}{\partial y} dA \qquad \text{(A2.12)}$$

Substituting equation (A2.11) into equation (A2.12), yields;

$$\vec{F}_{Spool} = -2 C_D A_o \Delta P \cos\vartheta - \iint_{A(Sleeve)} \mu \frac{\partial V_x}{\partial y} dA \qquad \text{(A2.13)}$$

Appendix B

Analytical Solutions for Steady Laminar Flow Between Parallel Plates for Viscous, Incompressible Fluid

The flow through the chamber can be model as a steady laminar flow between two fixed parallel plate. Hence this section will derived the analytical solutions for steady laminar flow between parallel plates for viscous, incompressible flow.

Consider the flow in the chamber to be laminar and to be similar to the flow between two infinite plates, separated by a gap width 2h. The plates are also considered infinite in the z – direction, with no variation of any fluid property in that direction.

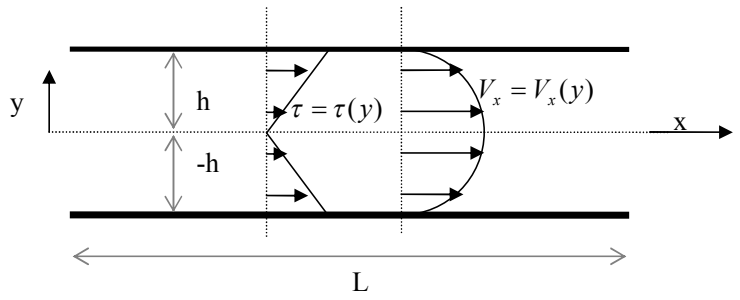

Figure B. 1: Typical velocity and shear stress distribution for viscous flow between parallel fixed plates

Assumptions:

(1) Flow is steady, incompressible and 2D.

(2) Flow is fully developed (FD) which means that the velocity profile in the stream wise direction is constant ($\frac{\partial(\ )}{\partial x} = 0$), and there is a linear pressure decrease ($\frac{\partial P}{\partial x} = -ve$).

(3) Flow is laminar with constant properties (μ, ρ are constant).

The equations that governed the flow are the continuity and Navier – Stokes equations.

Continuity equation:

$$\frac{\partial V_x}{\partial x} + \frac{\partial V_y}{\partial y} = 0 \qquad \text{(B1)}$$

The following boundary conditions are assumed:

I. Flow is fully developed (FD)

$$\frac{\partial(\ )}{\partial x} = 0, \qquad \text{(except for pressure, P)} \qquad \text{(B2)}$$

Since flow is fully developed (FD), the velocity cannot vary with *x* in the stream wise direction, and hence depends on y only, so that *u = u (y).* Only the pressure can vary with x, ($\partial P / \partial x$ is not zero).

II. At y = $\pm$ h,

$V_x = 0$ (no slip condition at the wall)

$V_y = 0$ (no penetration at the wall)

By applying boundary conditions (I) and (II) to equation (B1), equation (B1) becomes;

= 0 (F.D)

$$\frac{\partial V_x}{\partial x} + \frac{\partial V_y}{\partial y} = 0 \qquad \text{(B3)}$$

Equation (B.3) reduces to;

$$V_y = 0 \qquad \text{(everywhere)} \qquad \text{(B4)}$$

Momentum equation:

x - direction

0 = (F.D) $V_y = 0$ Ignore = 0 (F.D)

$$\rho V_x \frac{\partial V_x}{\partial x} + \rho V_y \frac{\partial V_x}{\partial y} = -\frac{\partial P}{\partial x} + \rho g_x + \mu\left(\frac{\partial^2 V_x}{\partial x^2} + \frac{\partial^2 V_x}{\partial y^2}\right) \qquad \text{(B5)}$$

y – direction

0 = (F.D) = 0 ($V_y = 0$) Ignore 0 = (F.D) = 0 ($V_y = 0$)

$$\rho V_x \frac{\partial V_y}{\partial x} + \rho V_y \frac{\partial V_y}{\partial y} = -\frac{\partial P}{\partial y} + \rho g_y + \mu\left(\frac{\partial^2 V_y}{\partial x^2} + \frac{\partial^2 V_y}{\partial y^2}\right) \qquad \text{(B6)}$$

By applying the assumption of fully developed (FD) conditions to equation (B.3), equation (B5) simplifies to:

$$0 = -\frac{\partial P}{\partial x} + \mu \frac{\partial^2 V_x}{\partial y^2} \tag{B7}$$

and equation (B6) simplifies to;

$$\frac{\partial P}{\partial x} = 0 \tag{B8}$$

Equation (B7) can be simplified as:

$$\frac{\partial^2 V_x}{\partial y^2} = \frac{1}{\mu}\frac{\partial P}{\partial x} \tag{B9}$$

Integrating equation (B9) with respect to y, equation (B9) becomes;

$$\frac{\partial V_x}{\partial y} = \frac{1}{\mu}\frac{\partial P}{\partial x} y + C_1 \tag{B10}$$

The pressure gradient term ($\partial P / \partial x$) in the integration is treated as constant since it is not considered to varied with respect to y.
Again, integrating equation (B10) with respect to y, it becomes;

$$V_x = \frac{1}{\mu}\frac{\partial P}{\partial x}\frac{y^2}{2} + C_1 y + C_2 \tag{B11}$$

By implementing the following boundary condition:

(i) at y = $\pm$ h, $V_x = 0$

Applying these conditions to equations (B10) and (B11) yields;

$C_1 = 0$ (B12)

$$C_2 = -\frac{1}{2\mu}\left(\frac{\partial P}{\partial x}\right)h^2 \quad \text{(B13)}$$

Velocity Profile

The velocity distribution is obtained by substituting equations (B12) and (B13) into equation (B11). Thus;

$$V_x = \frac{1}{2\mu}\left(\frac{\partial P}{\partial x}\right)\left(y^2 - h^2\right) \quad \text{(B14)}$$

Equation (B14) shows that the velocity profile between the plates is parabolic.

Volume Flow Rate

The volume flow rate is given by;

$$Q = \iint_A V_x . dA = \int_{-h}^{h} V_x w dy \quad \text{(B15)}$$

The volume flow rate per unit width w, in the z – direction is given as;

$$\frac{Q}{w} = q = \int_{-h}^{h} \frac{1}{2\mu}\left(\frac{\partial P}{\partial x}\right)\left(y^2 - h^2\right)dy = \frac{2h^3}{3\mu}\left(-\frac{\partial P}{\partial x}\right) \quad \text{(B16)}$$

Equation (B16) shows that the flow is proportional to the pressure gradient, inversely proportional to the viscosity and strongly dependent on the gap width ($\approx h^3$).

where $-\frac{\partial P}{\partial x} = \frac{\Delta P}{l}$ (B17)

and where ΔP represents the pressure drop between two points at a distance *l* apart.

Maximum Velocity

The maximum velocity occurs at the centerline, i.e. $y = 0$; $V_x = V_{\max}$; substituting these conditions into equation (B14) yields;

$$V_{\max} = \frac{h^2}{2\mu}\left(-\frac{\partial P}{\partial x}\right) \quad \text{(B18)}$$

Average Velocity

The mean velocity is given as;

$$V_{ave} = \frac{1}{2h}\int_{-h}^{h} V_x dy = \frac{2}{3}\left(-\frac{\partial P}{\partial x}\right)\frac{h^2}{2\mu} = \frac{2}{3}V_{\max} \quad \text{(B19)}$$

Shear stress distribution

The shear stress distribution is resolved at the walls; i.e. y = $\pm$ h.

$$\tau_{wall} = \mu\frac{\partial V_x}{\partial y} = y\left(\frac{\partial P}{\partial x}\right) \quad \text{(B20)}$$

Viscous Force

The viscous force is calculated as;

$$F_{viscous} = \iint_A \mu \frac{\partial V_x}{\partial y} dA = \int_0^L \tau_{wall} \underbrace{w dx}_{dA} = \tau_{wall} wL = y\left(\frac{\partial P}{\partial x}\right) wL \qquad \text{(B21)}$$

$$F_{viscous} = \frac{-3y}{2h^3}[\mu QL]$$

where $\frac{\partial P}{\partial x}$ comes from equation B16. (B22)

The viscous force at the walls (i.e. $y = h$) is given as;

$$F_{viswalls} = \frac{-3}{2h^2}[\mu QL]_{y=\pm h} \qquad \text{(B23)}$$

Equation (B23) shows that the viscous force at the walls is proportional to the dynamic viscosity (μ), inversely proportional to the gap width (h^2) and proportional to the flow rate Q.

Appendix C

The 2-D Incompressible Navier-Stokes Equations

For the steady, 2D, incompressible flow neglecting body forces, the differential equations that govern the flow are the Navier-Stokes (*x*- and *y*-momentum relations) and the non-trivial continuity equation.

Continuity:

$$\frac{\partial(\rho u)}{\partial x}+\frac{\partial(\rho v)}{\partial y}=0 \qquad \text{(C1.1)}$$

x - momentum

$$\rho u\frac{\partial u}{\partial x}+\rho v\frac{\partial u}{\partial y}=-\frac{\partial p}{\partial x}+\mu\left(\frac{\partial^2 u}{\partial^2 x}+\frac{\partial^2 u}{\partial^2 y}\right) \qquad \text{(C1.2)}$$

y - momentum

$$\rho u\frac{\partial v}{\partial x}+\rho v\frac{\partial v}{\partial y}=-\frac{\partial p}{\partial y}+\mu\left(\frac{\partial^2 v}{\partial^2 x}+\frac{\partial^2 v}{\partial^2 y}\right) \qquad \text{(C1.3)}$$

where P is the pressure, u and v are the velocity components in the x and y direction respectively.

The above equations are to be solved for (u, v and P) as a function of x, and y. There are three equations and three unknowns. Thus, the equations are closed. Closure means there is sufficient number of equations for the number of unknowns.

For incompressible flow, most of the work relates to solving for P (the pressure field). The pressure is coupled to velocity in the momentum equations and the problem is that there is no differential equation for which the dominant derivatives involve *p*. This situation has led to several differential 'pressure adjustment' schemes, most of which manipulate the continuity equation to insert a pressure correction. The pressure correction is intended to modify the pressure-velocity field to better conserve mass.

A second difficulty in the above equation is the presence of nonlinear convective acceleration such as $u(\partial u / \partial x)$ which creates asymmetry in viscous flow. Convection is what characterizes and complicates fluid flow. Due to the non -linearity of the Navier-Stokes equation, a solution can be obtained by iteration. This has led to several numerical convection schemes.

In principle, the N-S equation describes both laminar and turbulent flow without the need for additional information. However, turbulence consists of fluctuations in the flow field in time and space. It is a complex process, mainly because it is three dimensional, unsteady and consists of many scales. Turbulent flow at realistic Reynolds numbers span a large range of turbulent length and time scales and would generally involve length scales much smaller than the smallest finite volume mesh which can be practically used in numerical analysis. In turbulent flow, the total viscosity is made up of the laminar viscosity which is constant and the turbulent or eddy viscosity, which is dependent on the flow field. Every velocity and pressure term is a rapidly varying function of time and space. The instantaneous variables are split into a mean plus a fluctuating component ($P = \bar{P} + P'$). For example, P is equal to the mean pressure $\bar{P}$ and the fluctuating component term P'. The same can be said for the velocities. These variables are solve

using a time average. So for turbulent flow, the expression for the time- averaged momentum field decomposes to:

x - momentum:

$$\rho\left(\bar{u}\frac{\partial\bar{u}}{\partial x}+\bar{v}\frac{\partial\bar{u}}{\partial x}\right)=-\frac{\partial\bar{p}}{\partial x}+\frac{\partial}{\partial x}\left(\mu\frac{\partial\bar{u}}{\partial x}-\overline{\rho u'u'}\right)+\frac{\partial}{\partial y}\left(\mu\frac{\partial\bar{u}}{\partial y}-\overline{\rho v'u'}\right) \qquad \text{(C1.4)}$$

y - momentum

$$\rho\left(\bar{u}\frac{\partial\bar{v}}{\partial x}+\bar{v}\frac{\partial\bar{v}}{\partial x}\right)=-\frac{\partial\bar{p}}{\partial y}+\frac{\partial}{\partial x}\left(\mu\frac{\partial\bar{v}}{\partial x}-\overline{\rho v'u'}\right)+\frac{\partial}{\partial y}\left(\mu\frac{\partial\bar{v}}{\partial y}-\overline{\rho v'v'}\right) \qquad \text{(C1.5)}$$

Equations (C1.4 and C1.5) are the expanded form of equation (3.2).

This equation remains very much the same like equations (C1.2) and (C1.3), except that it is written for the mean field. The time averaging of the Navier - Stokes equation introduces four more unknown terms ($u', v', , \bar{u}, \bar{v},$), thereby complicating the flow problem. This leads to closure problems. The correlations $-\overline{\rho v'u'}$, $-\overline{\rho v'u'}$, are called the Reynolds stresses which are also non-linear. To enable the effects of turbulence to be predicted, a large amount of CFD research has concentrated on methods, which make use of turbulence models. Turbulence models have been specifically developed to account for the effects of turbulence without recourse to a prohibitively fine mesh. Turbulence models are used to close the Reynolds average Navier - Stokes equations by introducing some additional variables, which express the Reynolds stress in terms of known field variables ($\partial u_i / \partial x_j$). One such model that has been widely used in simulating hydraulic flow is the $k-\varepsilon$ model. It introduces two additional transport equations and as such it is a two-equation closure model. In CFX-5.6, these two transport equations are resolved as K-TurbKE and E-Diss.K.

For a steady, 2D, incompressible, turbulent flow with no thermal interaction, the CFX-5.6 solver solves five equations simultaneously, - the continuity, the two momentum equations and the two-transport equation introduced by the turbulence model.

C2.1 Steady 1-D Convection-Diffusion Flow

The general form of the transport equation for a general fluid property ϕ can be written as;

$$\frac{\partial}{\partial t}(\rho\phi)+\frac{\partial}{\partial x}\left(\rho u\phi-\Gamma\frac{\partial\phi}{\partial x}\right)=S \qquad \text{(C2.1)}$$

In equation (C2.1), ϕ is the variable in question and the only unknown in the equation, u is the velocity. Γ is the diffusion coefficient, ρ is the density and S is the source term. For steady flow with no source term, equation (C2.1) yields;

$$\frac{\partial}{\partial x}(\rho u\phi)=\Gamma\frac{\partial\phi}{\partial x} \qquad \text{(C2.2)}$$

The continuity equation is written as;

$$\frac{\partial}{\partial x}(\rho u)=0 \qquad \text{(C2.3)}$$

The description of the control volume is shown in Figure C2.1. The letter P represents the current computational cell and E and W represent the nodal points at the east and west side of P. The letterings e and w represent the control volume faces in the east and west direction respectively.

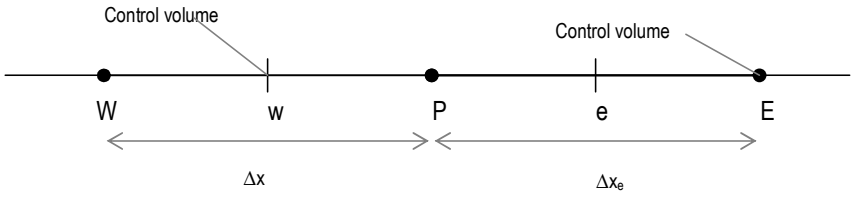

Figure C2. 1: Control volume

The finite volume method prescribes integrating the above equations i.e. equations (C2.2 and C2.3) over the 1D control volume. Upon integrating, equations (C2.2 and C2.3) yield;

$$\left(\rho u A \phi\right)_e - \left(\rho u A \phi\right)_w = \left(\Gamma A \frac{\partial \phi}{\partial x}\right)_e - \left(\Gamma A \frac{\partial \phi}{\partial x}\right)_w \tag{C2.4}$$

And for the continuity;

$$\left(\rho u A\right)_e - \left(\rho u A\right)_w = 0 \tag{C2.5}$$

where A (which appears because of a unit depth) represents the area of the control volume face.

The convective and diffusive fluxes are defined as;

$$\dot{m} = \rho u A \qquad \text{and} \qquad D = \frac{\Gamma A}{\Delta x} \tag{C2.6}$$

Substituting equation (C2.6) into equations (C2.4 and C2.5) yield the following;

$$\dot{m}_e \phi_e - \dot{m}_w \phi_w = \left(D \Delta x \frac{\partial \phi}{\partial x}\right)_e - \left(D \Delta x \frac{\partial \phi}{\partial x}\right)_w \tag{C2.7}$$

$$\dot{m}_e - \dot{m}_w = 0 \qquad u_e - u_w = 0 \tag{C2.8}$$

where $\dot{m}_w$ and $\dot{m}_e$ are the mass flow rates at cell faces *w and e* respectively.

Equation (C2.7) requires an estimate of both the value of ϕ and its derivative $\partial\phi/\partial x$ at the face. As such the central differencing scheme[3] is employed. This uses a linear approximation between adjacent nodes to evaluate the flux at the face. Thus;

$$\phi_e = \frac{\phi_P + \phi_E}{2} \qquad \text{and} \qquad \phi_w = \frac{\phi_P + \phi_w}{2} \tag{C2.9}$$

$$\left.\frac{\partial\phi}{\partial x}\right)_e = \frac{\phi_E - \phi_P}{\Delta x_e} \quad \text{and} \quad \left.\frac{\partial\phi}{\partial x}\right)_w = \frac{\phi_P - \phi_W}{\Delta x_w} \tag{C2.10}$$

and similarly;

$$u_e = \frac{u_P + u_E}{2} \qquad \text{and} \qquad u_w = \frac{u_W + u_P}{2} \tag{C2.11}$$

Substituting equation (C2.11) into equation (C2.8) yields;

$$u_E - u_W = 0 \tag{C2.12}$$

Equation (C2.12) shows that the discretized continuity equation demands the equality of velocities at alternate (and not at adjacent) grid points. Substituting in for appropriate terms yields:

[3] The central differencing scheme is used in the analysis for convenience. In CFX 5.6, the default for the differencing scheme is the hybrid differencing scheme of Patankar (22).

$$\dot{m}_e\left(\frac{\phi_P+\phi_E}{2}\right)-\dot{m}_w\left(\frac{\phi_P+\phi_W}{2}\right)=D_e\Delta x_e\left(\frac{\phi_E-\phi_P}{\Delta x_e}\right)-D_w\Delta x_w\left(\frac{\phi_P-\phi_W}{\Delta x_w}\right) \qquad \text{(C2.13)}$$

$$\frac{\dot{m}_e\phi_P}{2}+\frac{\dot{m}_e\phi_P}{2}-\frac{\dot{m}_w\phi_P}{2}-\frac{\dot{m}_w\phi_P}{2}=D_e\phi_E-D_e\phi_P-D_w\phi_P+D_w\phi_w \quad . \qquad \text{(C2.14)}$$

Collecting like terms;

$$\left(\frac{\dot{m}_e}{2}-\frac{\dot{m}_w}{2}+D_e+D_w\right)\phi_P=\left(D_e-\frac{\dot{m}_e}{2}\right)\phi_E+\left(D_w+\frac{\dot{m}_w}{2}\right)\phi_W \quad . \qquad \text{(C2.15)}$$

The discrete equation can be written in the following form;

$$a_P\phi_P=a_E\phi_E+a_W\phi_W+b\,, \qquad \text{(C2.16)}$$

where $a_E=D_e-\frac{\dot{m}_e}{2}$; and $a_W=D_w+\frac{\dot{m}_w}{2}$. (C2.17)

Relating a_P to a_E and a_W yields

$$a_P=a_E+a_w+k\,,$$

$$\frac{\dot{m}_e}{2}-\frac{\dot{m}_w}{2}+D_e+D_w=D_e-\frac{\dot{m}_e}{2}+D_w+\frac{\dot{m}_w}{2}+k\,,$$

$$k=\dot{m}_e-\dot{m}_w\,.$$

Thus

$$a_P=a_E+a_W+\left(\dot{m}_e-\dot{m}_w\right). \qquad \text{(C2.18)}$$

The above equations (C2.16, C2.17 and C2.18) form a tri – diagonal system and can be solved by any iterative scheme such as the Gauss – Seidel point by point iteration method.

Appendix D

Geometry Creation and Mesh Generation using the Commercial CFD Software Module CFX-Build

The objective of this appendix is to demonstrate the solution process of commercial numerical software, CFX 5.6. The same valve that was used by Gao (10) in his study shall be employed for illustration.

D.1.1 Creating the Database

Start *CFX-Build* from the CFX-5 Launcher.
When CFX-Build is loaded, select File > New … from the Main Menu.
Create a new database called **GaoValve75cm**
When the *New Model Preferences* form appears:

Set *Geometry dimensions* In to **centimetre (cm)**.
Set *Global Model Tolerance* to 0.005

Select Preference > Mesh Mode … from the Main Menu
When the *Mesh Mode* form appears:
Set Volume Meshing to Patran Volume Meshing and Apply

D1.2 Creating the Geometry and Mesh

The geometry and mesh was created in the CFX – Build module, using the CFD commercial code, CFX 5.6. The steps are illustrated as follows;

Step 1:

Create all points first
(Create > Point > XYZ)

Create curves between two points
(Create > Curve > Point)

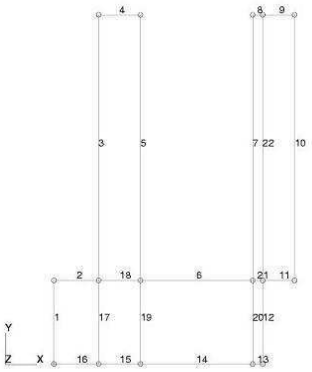

Step 2:

Create surfaces
(Create > Surface > Curve)

These surfaces should be parametric surface, i.e. each surface has four edges, four vertices

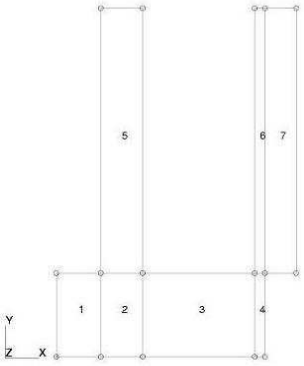

Step 3:

Create parametric solids.
(Create > Solid > Extrude)

Use the Extrude function to create solid, make sure the solid type is isomeshable. Extrude the solid 3 cm in the z - direction

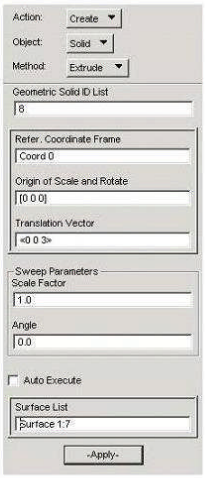

Step 4:

Create the 3D region. The name is GaoValve75cm.Select the whole geometry and Apply

The 3D region defines the region of fluid flow

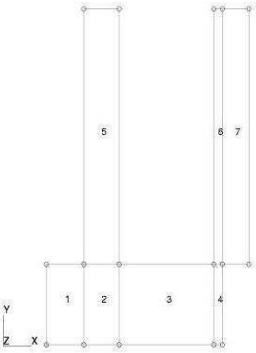

Step 5:

Create the 2D regions by entering their names in the Name data box and selecting their appropriate faces.

The 2D regions are planes within the flow domain at which boundary conditions shall be apply in CFX - Pre. The boundaries so created are : IN, OUT, FRONT & BACK symmetry boundaries.The code considered other surfaces that are not assigned a boundary as a no slip wall

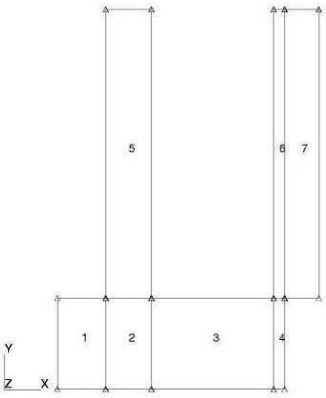

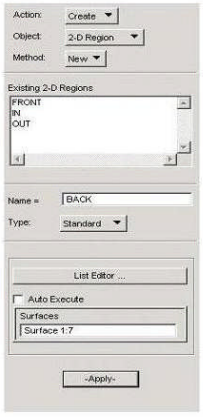

Step 6:

Use Mesh Seed to specify the mesh distribution. This is done by deciding on the number of Mesh Seeds on a given curve and also properly selecting the distribution ratio

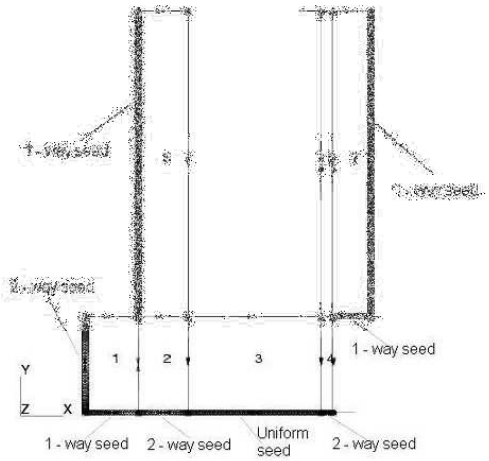

Block	Number of mesh
1	25 x 50
2	24 x 50
3	80 x 50
4	14 x 50
5	24 x 160
6	14 x 160
7	22 x 160

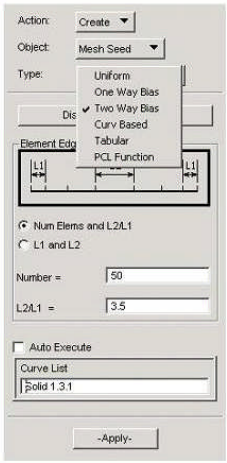

Step 7:

Create the 2D solid mesh. The Global Edge Lenght was set to 3 cm, which is equal to the domain width. In this way, only one control volume is placed in the z - direction

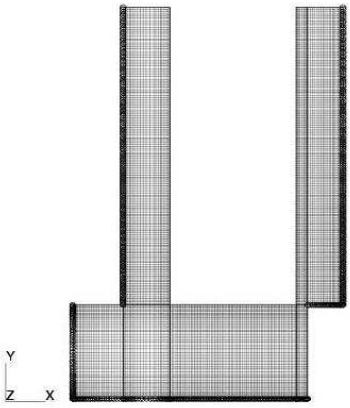

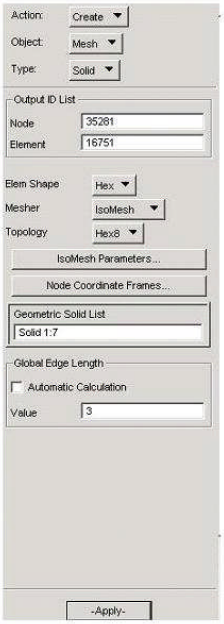

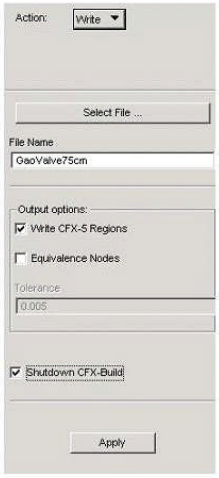

Step 8:

The last step in CFX - Build is to write the file which contains the geometry and mesh information.

This file is to be imported into CFX - Pre for pre - processing.

D2 Defining the Flow Physics in CFX-Pre

D2.1 Creating the CFX file

Start *CFX-Pre* from the CFX-5 Launcher.

When CFX-Pre is loaded, select File > New … from the Main Menu.

Create a new file called **GaoValve75cm.**

Click the *Import Mesh* icon …..

When the *Import Mesh* form appears:

On Definitions

Set *Mesh Format* to *Patran Neutral*

Set *File* to **GaoValve75cm.out**

Leave *Mesh Assembly Name* as *Assembly*

Set *Mesh Units* to **cm**

On advanced Options:

Enable *Duplicate Node Checking*

Set *Relative Tolerance* to **1e – 005**

Press – Apply

Physical Models:

D2.2 Defining the Fluid Properties

Select *Tool* > *Material Editor*… from the Main Menu.

When the Material Editor form appears:

In the *Name* data box, type *Hydraulic Oil*.

Set *Density* to **871 kgm^-3**

Enable *Transport Properties*

Set *Dynamic Viscosity* to **0.0375 kg m^-1 s^-1**

Press Apply

D2.3 Creating the Fluid Domain

The Fluid Domain for this simulation is isothermal and laminar.

Select *Domains* radio button.
Enter **GaoValve75cm** in the *Name* data box.
Open the *Domain* Options… form. Choose the following:
Leave *Assembly* as *Location*
Set *Fluid Lists* to *Hydraulic Oil*
For *Reference Pressure*, enter a value of **0 Pa.**
Set *Buoyancy Option* to *Non – Buoyant*
Set *Domain Motion Option* to *Stationary*
Open the *Fluid Model* form. Choose the following;
Set *Heat Transfer Model* to *Isothermal*
Set *Turbulence Model* to *None (Laminar)*
Press - Apply - to create the Fluid Domain.

D2.4 Defining Boundary Conditions

The problem involves applying the following boundary conditions.

1. Fully developed velocity profile at the inlet
2. Pressure Outlet
3. Symmetry boundaries at the low and high z- faces
4. No slip wall boundary condition for all walls.

Select *the Boundary Conditions* radio button.

The simulation requires Inlet, Outlet, Wall and Symmetry plane boundary conditions.

The inlet velocity profile is defined by using equation B.14. The expression is defined in CFX code by using the CFX – 5 Expression Language (CEL). The expression is defined as:

Select *Tool* > *Expression Editor* …. From the Main Menu
When the Expression Editor form appears:
Click on the *New Expression* icon
Type **h** in the *Name* data box
Press *ok*
In the *Definition* box, Enter **1.5 [cm]**
Press *Apply*

Click on the New Expression icon
Type *Vmax* in the Name data box
Press OK
In the Definition box, Enter **0.01 [m s^-1]**
Press Apply

Click on the *New Expression* icon
Type ***Vprof*** in the *Name* data box
Press *ok*
In the *Definition* box, Enter ***Vmax* (abs (1-(x/h) ^2))***
Press *Apply*

The solver will fail if $(1-(x/h))$ is negative as slightly negative values can be obtained at the walls due to geometry tolerance errors (i.e. $x = 0.015000001$, when $h = 0.015$).

In order to prevent this, negative values of $(1-(x/h))$ are set equal to 0.0 using the abs (absolute) function.

Select *Define* > *Boundary Conditions* … from the Main Menu

Type *IN* in the *Name* Data box
Set the *Type* Option to *Inlet*

Open the values… form
Set *Flow Regime* to *Subsonic*
Set *Mass and Momentum* to *Normal Speed*
Use the Expression icon to enter Vprof

Close the Values form.

Set the *Auto Execute* toggle *OFF*, and in the *Surfaces* data box pick the *inlet plane*.
Press Apply to create the Inlet boundary condition

Select *Define* > *Boundary Conditions* … from the Main Menu

Type *OUT* in the *Name* Data box
Set the *Type* Option to *Outlet*

Open the values… form
Set *Flow Regime* to *Subsonic*
Set *Mass and Momentum* to *Static Pressure*
Enter a value of **0.0 Pa** for the *Relative Pressure*

Close the Values form.

Set the *Auto Execute* toggle *OFF*, and in the *Surfaces* data box pick the outlet plane.
Press Apply to create the Outlet boundary condition

Select *Define* > *Boundary Conditions* … from the Main Menu
Type *FRONT* in the *Name* Data box

Set the *Type* Option to *Symmetry*
In the *Surfaces* data box select the ***High z*** face of the rectangular region

Press Apply to create the Symmetry Plane boundary condition

Select *Define* > *Boundary Conditions* … from the Main Menu

Type *BACK* in the *Name* Data box
Set the *Type* Option to *Symmetry*
In the *Surfaces* data box select the ***Low z*** face of the rectangular region

Press Apply to create the Symmetry Plane boundary condition

The remaining wall surfaces of the rectangular region that were not define, by default, are consider as a no slip boundary condition by the code.

Select *Define* > *Solver Control* … from the Main Menu
On *Basic Setting* Option;
Set *Advection Scheme* to *High Resolution*
Set *Max. No. of Iterations* to **800**
Set *Length Scale* Option to *Conservative*
Set *Residual Type* to *RMS*
Set *Residual Target* to **1e-9**
Enable the *Conservation Target* and set the value to **0.0001**
Press Apply

Select *Define* > *Write Definition File* … from the Main Menu
Set *File Name* to *D35*
Set *Operation to Start Solver Manager with def*
Enable *Quit CFX – Pre*
Press Apply

D3 Visualizing the Results in CFX-Post

When the Solver Manager has completed run, on Solver Manager

Select *Tool* > *Post – Process Results* … from the Main Menu in CFX Solver Manager
When the Start CFX – Post form appears
Enable *Shut down Solver Manager*
Click *ok*

When CFX – Post appears
Press the *View Toward –Z* Toolbar icon

D3.1 Creating Vector Plot

A vector plot shall be created to show the velocity vectors at the FRONT plane (one of the two symmetry planes)

Select *Create* > *Vector* …..from the main menu in CFX – Post
Type **Velocity** in the *Name* data box
When the Velocity vector form appears:
On the Geometry Options
Select *All Domains* for *Domains*
Select **FRONT** from the list of *Locators*
Select *Variable* to *Velocity*
Enable the *Visibility* button
Press *Apply* to create the vector plot

D3.2 Creating Pressure Contour Plot

Select *Create* > *Contour*…..from the main menu in CFX – Post

Type Pressure in the Name data box

When the Pressure Contour form appears:

On the *Definition* Options

Select *All Domains* for *Domains*

Select **FRONT** from the list of *Locators*

Select *Variable* to *Pressure*

Select *Global* for *Range*

Enable the *Visibility* button

Press *Apply* to create the pressure contour plot

Appendix E

E Numerical Methodology

The objective of this appendix is to discuss concepts which are necessary to facilitate the understanding of the numerical methodology discussed in Chapter 3.

E1 Modeling Flow Near the Wall[4]

In the region near a no – slip wall, there are strong gradients in the dependent variables. In addition, viscous effects on the transport processes are large. The representation of these processes within a numerical simulation raises the following problems:

- How to account for viscous effects at the wall.
- How to resolve the rapid variation of flow variables which occurs within the boundary layer region.

Experiments and mathematical analysis have shown that the near – wall region can be divided into two layers. In the innermost layer, the so called "viscous sub-layer" is where the flow is almost laminar and the molecular viscosity plays a dominant role in momentum and heat transfer. Further away from the wall is the "turbulent layer", where turbulence dominates the mixing process. Finally, there is an intermediate region between the viscous sub-layer and the turbulent layer called the "overlap layer", where the effects of molecular viscosity and turbulence are of equal importance. Figure E1 illustrates these subdivisions of the near wall region.

[4] The information presented in this section was extracted from the CFX 5.6 User Documentation

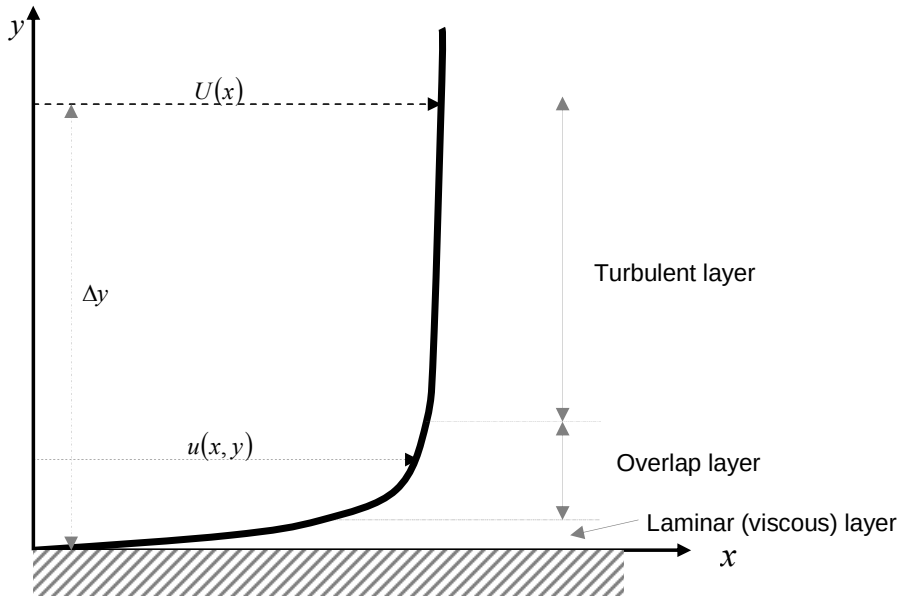

Figure E1. 1: Typical velocity profile in turbulent flow near a wall

Two approaches are commonly used to model the flow in the near wall region: the wall Function and the Low Reynolds Number Methods. These are now briefly described.

- The Wall Function method uses empirical formulas by assuming a functional shape (i.e., the log – law) to approximate the velocity distribution near the wall, without resolving the boundary layer.

$$\frac{u}{u_\tau} = \frac{1}{k}\ln\frac{\Delta y u_\tau}{\nu} + B \qquad \text{(Overlap layer)} \qquad \text{(E1)}$$

where u is the velocity; u_τ is the friction velocity; Δy is the distance between the wall and the first node; and κ and B are dimensionless constants having approximates values of 0.41 and 5, respectively. Also in Figure E1, U is the free stream velocity.

The major advantage of the wall function approach is that the high gradient shear layers near the walls can be modeled with relatively coarse meshes, yielding substantial savings in CPU time and storage. It also avoids the need to account for viscous effect in the turbulence model. The disadvantage is that it imposes an upper grid limitation on the resolution of the mesh near the wall. For example, the y^+ (y^+ is discussed in the next section) values must be greater than 11.5 for the model to work well. In the CFX 5.6 code, when the "Scalable Wall Function" option is used for near wall modeling, the y^+ values should ideally be 30 – 150. If y^+ is below 11.5, the wall function is no longer valid and the wall shear calculations are wrong and could affect the flow pattern. So sometimes refining the mesh could give worse results.

- The Low – Reynolds – Number method (low – *Re* method) resolves the details of the boundary layer profile by using very small mesh length scales in the direction normal to the wall. The SST and models based on the ω - equation are suitable for a Low – Re method. It should be noted that the low – *Re* method does not refer to low Reynolds number, but to the turbulent Reynolds number which is low in the viscous sub-layer. The method can be used in simulations with high Reynolds number, as long as the viscous sub-layer has been resolved.

  The computations are extended through the viscosity affected sub-layer close to the wall. The low – *Re* approach requires a very fine mesh in the near wall zone and correspondingly large number of nodes. Computer storage and runtime requirements are higher than those of the wall function approach and care must be taken to ensure good numerical resolution in the near wall region to capture the rapid variation in variables. Since the SST model uses the low - *Re* approach, it is critical to ensure that all near-wall nodes are less than some specified value. However, it is advisable to resolve the boundary layer with at least 10 mesh nodes (CFX 5.6 documentation).

E2 Near-Wall Resolution

Most turbulence model works well depending on the near wall resolution. Hence it is a good practice to check how the mesh near the wall is resolve after the simulation. One parameter to check is the values of y^+. The quantity y^+ is a non-dimensionless wall distance that provides an indicator of the "effective proximity" of the first node to the wall. For example, for a turbulence model using the wall function approach, the value of y^+ should be greater than 11, otherwise the computation will degrade in accuracy. It is calculated as follows:

$$y^+ = \frac{\mu \Delta y u_\tau}{\rho} \qquad \text{(E2.1)}$$

$$u_\tau = \sqrt{\frac{\tau_w}{\rho}} \qquad \text{(E2.2)}$$

where Δy is the distance between the wall and the first node, u_τ is the friction velocity and τ_w is the shear stress at the wall.

Using CFX 5.6 the friction velocity is calculated by the code by equation (E2.2) and comes as part of the solution. To ensure that placement of the node to reflect y^+, is done on a trial and error basis and since the solution is continuously evolving, it is not possible to know y^+ purely based on Δy; thus, u_τ also has to be known. Thus, the user uses a mesh, runs the simulation for few iterations and then checks y^+. By knowing the value of y^+, the value of Δy can be determine from equation (E2.1). Depending on this value, the mesh is refined or made coarse. So if Δy is known, that value of Δy is set equal to L_1 in a one–way bias seeding (as shown in section 6 of Appendix D1). A geometrical progression is used with first term $a = L_1$ and common ratio $r = L_2/L_1$ to distribute the mesh.

E3 PIV Experiment of Gao (10)

Since the CFX 5.6 results were compared to both the PIV and FEM results of Gao (10), it is helpful to first provide a brief description of the PIV method. The PIV method is a flow measurement technique which provides information a section of the flow field.

The PIV test model of the valve used the geometry given in Figure 3.1, which was also used for the FEM simulation. The test model was made from a transparent acrylic sheet 4 *mm* thick; it was *7 cm* in width, with an opening of *3.75 cm*. The flow medium was water, seeded with particles that were assumed to follow the flow. The tracing particles were spherical, with a diameter of $30-50\mu m$. The general principle of PIV (Adrian, 1991) was to measure the displacement Δs of tracing particles moving with the fluid over a very short time known interval Δt. The velocity was calculated as $u = \Delta s/\Delta t$.

Gao's PIV experimental setup consisted of a reservoir that contained the fluid with the tracing particles, a pump to circulate the fluid, two rotating flow meters with different measuring ranges to record the amount of flow that was passed through the test model, the model spool valve being tested, and connecting pipes and valves for controlling the flow rate. The PIV measurement system consisted of two pulsed lasers, a digital camera, Data Acquisition (DAQ) systems and PC for data and image processing. The test section was illuminated by the two pulsed lasers, which were mounted normal to a fast frame transfer CCD camera which recorded the images of the tracing particles. The digital camera was synchronized with the pulsed lasers so that every time a laser flashed, the camera took a picture of the tracing particles (or the light reflected by them.). The time interval Δt, between flashes was $1.5ms$.

The Fast Fourier Transform (FFT) algorithm was used in image processing software. The results of the PIV experiments were post-processed and presented in the form of velocity vector plots. The velocity values at specified locations in the flow domain were extracted and compared with the results of the FEM simulations. For convenience of comparing the results of PIV with that of FEM, a 49 x 32 mesh structure, which was the same as for the

FEM simulation, was used to process the particle images. Hence, the flow domain of both PIV experiments and FEM simulation had the same total of 895 nodes. It should be pointed out that PIV is a powerful full field velocity measuring tool, but in general, the accuracy of PIV technique is affected by a number of factors such as the transparency of the model walls, the quality of the laser light sheet, the properties of the tracing particles and the image processing algorithm.

E4 Comparison of CFX 5.6 Results to Gao's FEM Results for Spool Opening of 0.75 and 1.125 cm

In this section of the appendix, CFX results shall be compared to Gao's FEM results for spool opening of 0.75 and 1.125 *cm*. There were no PIV results presented for these openings.

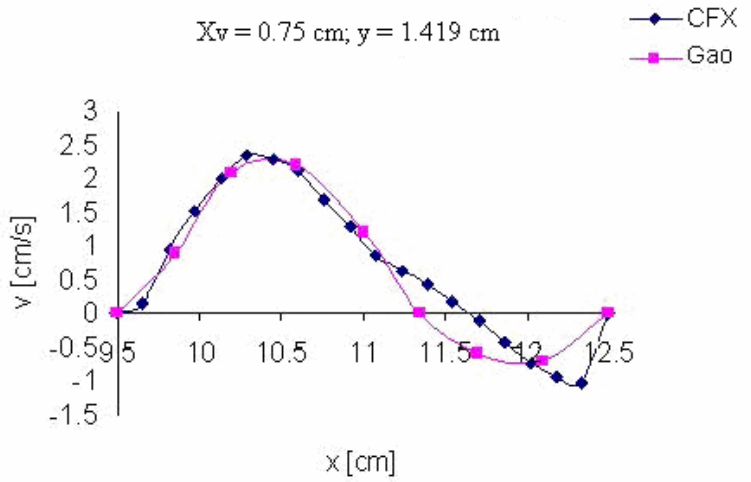

Figure E4. 1: The vertical velocity profile at y = 1.419 cm for a spool opening of 0.75 cm. The simulated results from CFX 5.6 were compared to the FEM based simulations of Gao (6)

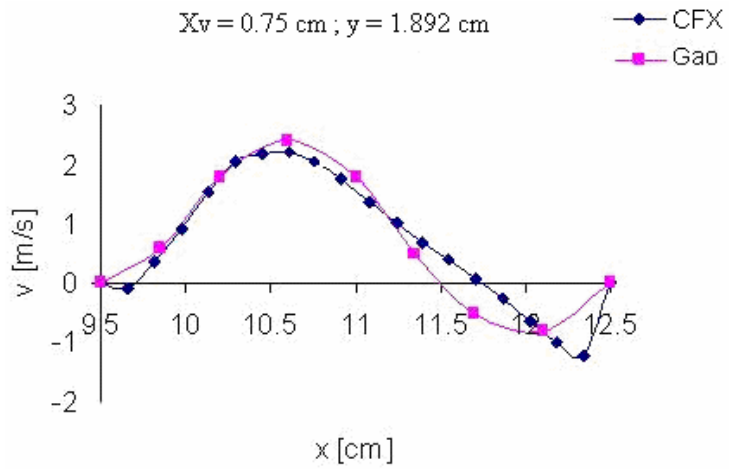

Figure E4. 2: The vertical velocity profile at y = 1.892 cm for a spool opening of 0.75 cm. The simulated results from CFX 5.6 were compared to the FEM simulations of Gao (6)

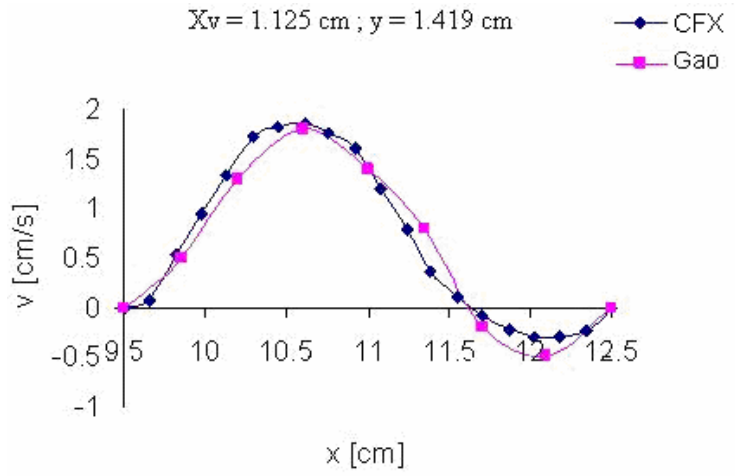

Figure E4. 3: The vertical velocity profile at y = 1.419 cm for a spool opening of 1.125 cm. The simulated results from CFX 5.6 were compared to the FEM simulations of Gao (6)

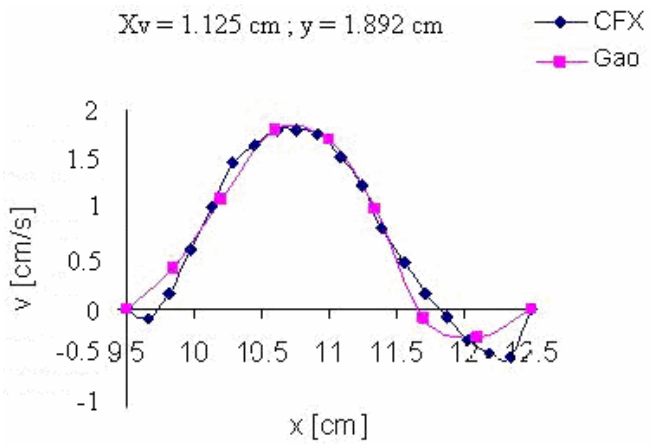

Figure E4. 4: The vertical velocity profile at y = 1.892 cm for a spool opening of 1.125 cm. The simulated results from CFX 5.6 were compared to the FEM simulations of Gao (1)

Appendix F

Calculation of the Fluid Jet Angle from CFD Results

This section shall describe the systematic approach adopted to calculate the jet efflux angle at the metering section using the results from the CFX 5.6 simulations. The logic is to sum the local components of the velocity, which is weighted by the control volume area. The approach was to create an $x - y$ plane at the metering section as show in Figure F1.1. The 'streamline velocity', 'velocity u', and 'velocity v' on the $x - y$ plane were extracted from the CFD results. Since the mesh distribution is not uniform, the area – weighted average of the resultant velocity V_{RES} and the u and v velocity components (U and V) were calculated on all location in the plane. The area-weighted average takes into account the mesh element sizes; otherwise the average will be biased towards the velocity values in regions of high mesh density. This gave the average of the resultant velocity and the x and y components of velocity respectively. Using these three values, a vector diagram could be drawn (see Figure F1.2) and the angle between the resultant and x component computed.

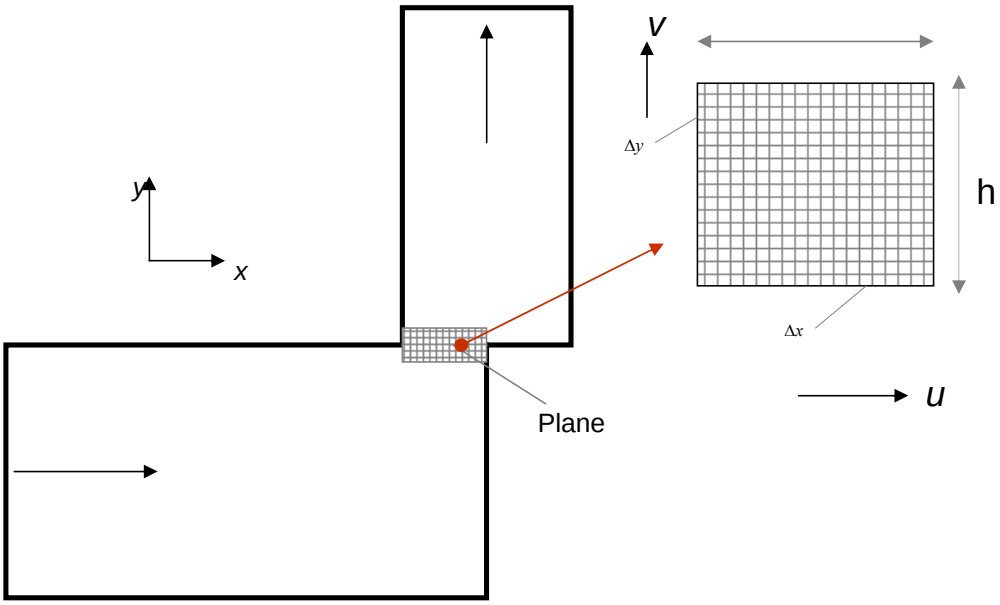

Figure F1. 1: Estimation of velocity streamlines showing the jet angle

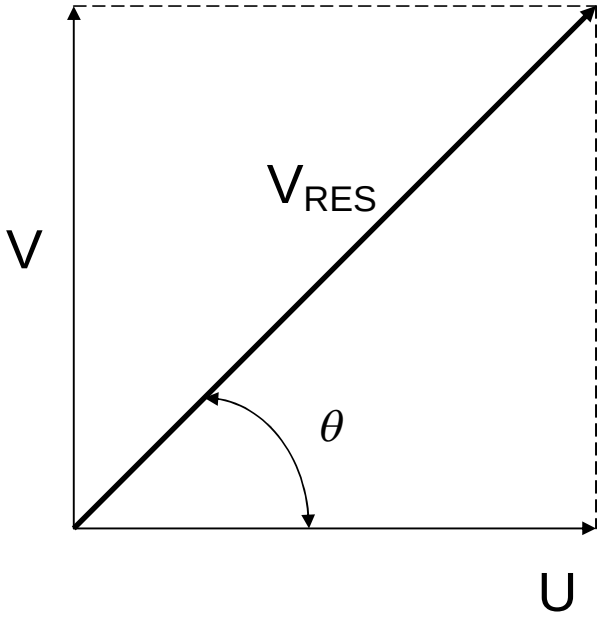

Figure F1. 2: Vector diagram

Mathematically, the area-weighted average of some quantity "F" on some plane "A" is defined as,

Area –weighted average of quantity F = [Area integral (F) on Plane A] / [Area (Plane A) (F1.1)

Hence the area integral for the *u* and *v* velocities shown in Figure F1.1 (a) are defined as,

$$U = \frac{1}{XY}\sum_{i=1}^{n} u_i dydx \qquad \text{(F1.2)}$$

$$V = \frac{1}{XY}\sum_{i=1}^{n} v_i dxdy \qquad \text{(F1.3)}$$

where X and Y are the extents of the plane in the x and y directions.

The fluid jet angle calculated is only some average value (referring to Figure F1.2), and is obtained from the expression;

$$\theta = \tan^{-1}\left(\frac{V}{U}\right) \qquad \text{(F1.4)}$$

F2 Velocity Plots for the Inflow Conditions

This section shall presents velocity contour (because it produced the best graphical representation of the flow field) plot obtained from CFD simulation for the case of a meter – in orifice. Results were presented for the three different valve configurations namely; standard, rim and sharp edge tapered rim spool, for spool displacement of 0.5 mm.

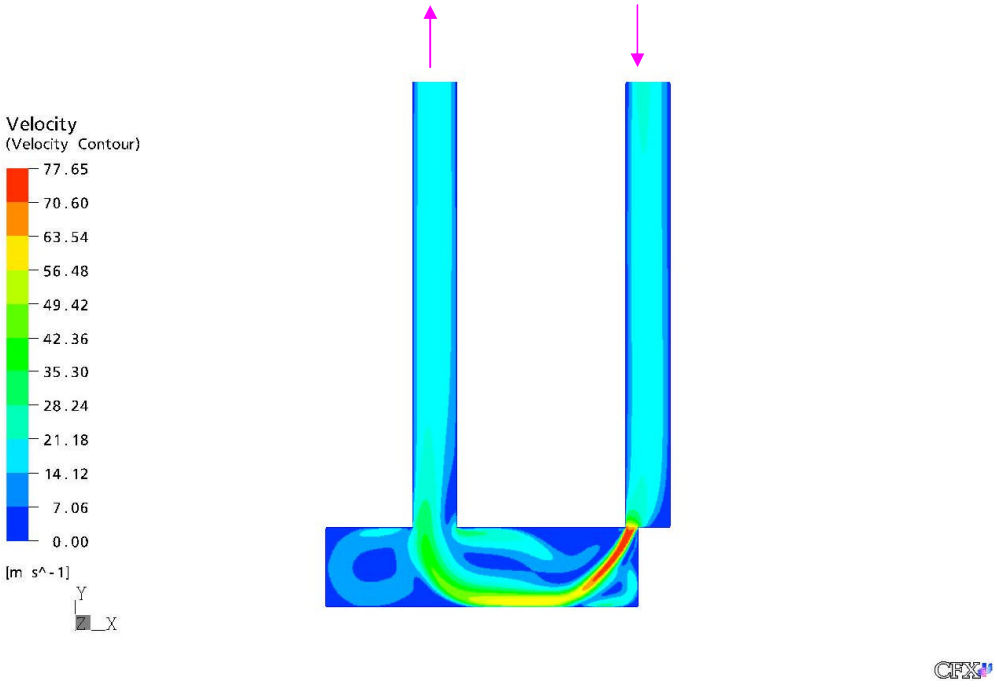

Figure F2.1.1: Velocity contours of the flow field of the standard spool valve for a meter–in orifice (x_v = 0.5 mm)

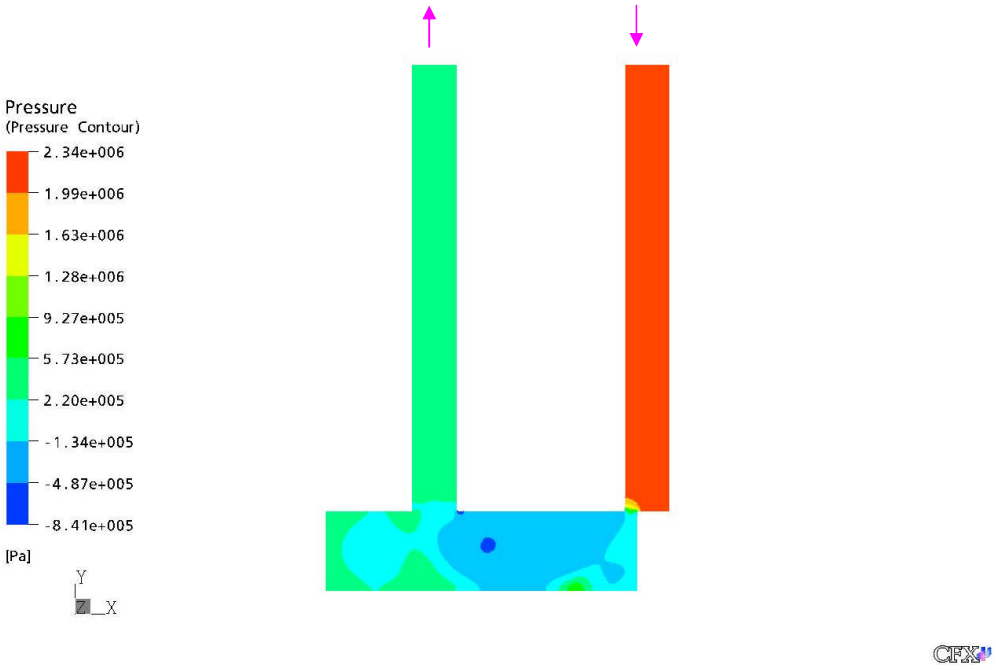

Figure F2.1.2: Pressure contours of the flow field of the standard spool valve for a meter–in orifice (x_v = 0.5 mm)

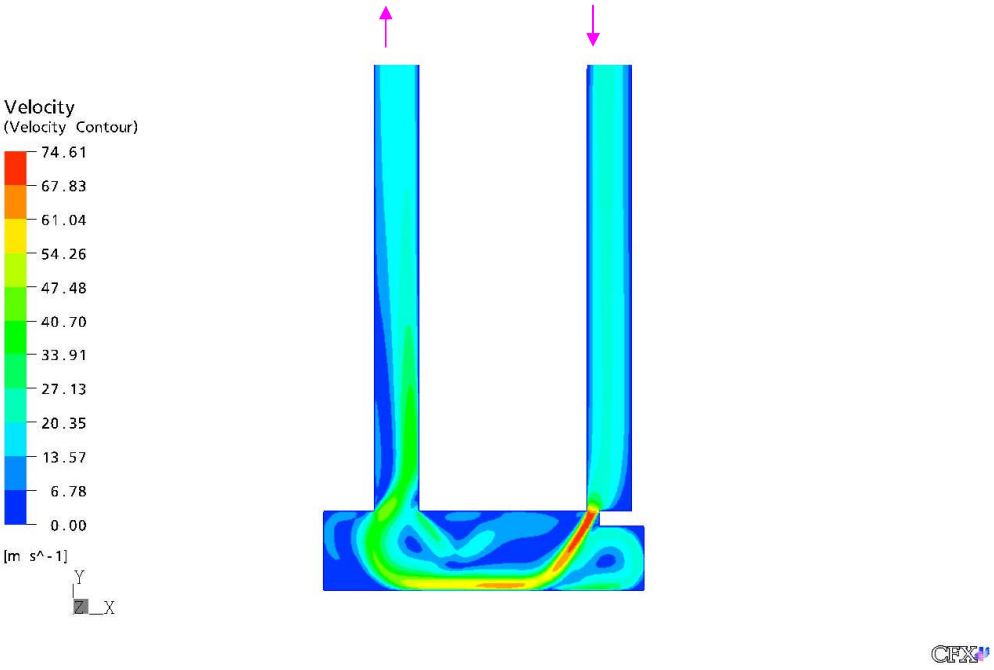

Figure F2.2.1: Velocity contours of the flow field of the rim spool valve for a meter–in orifice (x_v = 0.5 mm)

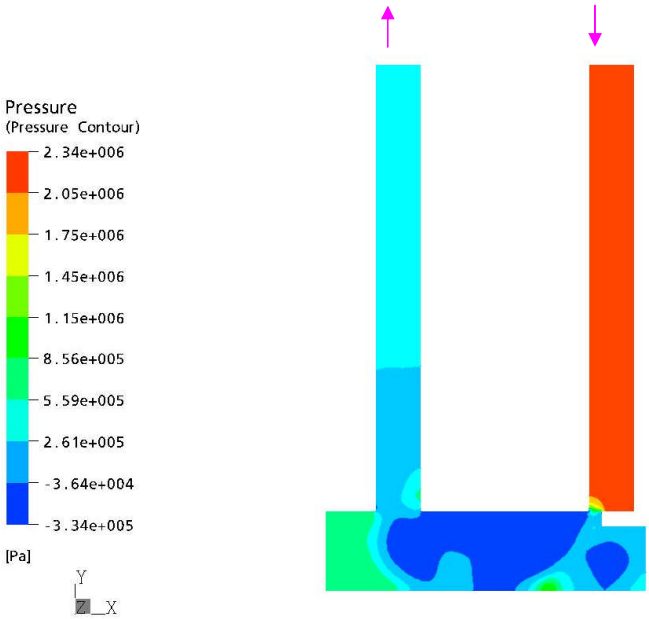

Figure F2.2.2: Pressure contours of the flow field of the rim spool valve for a meter–in orifice (x_v = 0.5 mm)

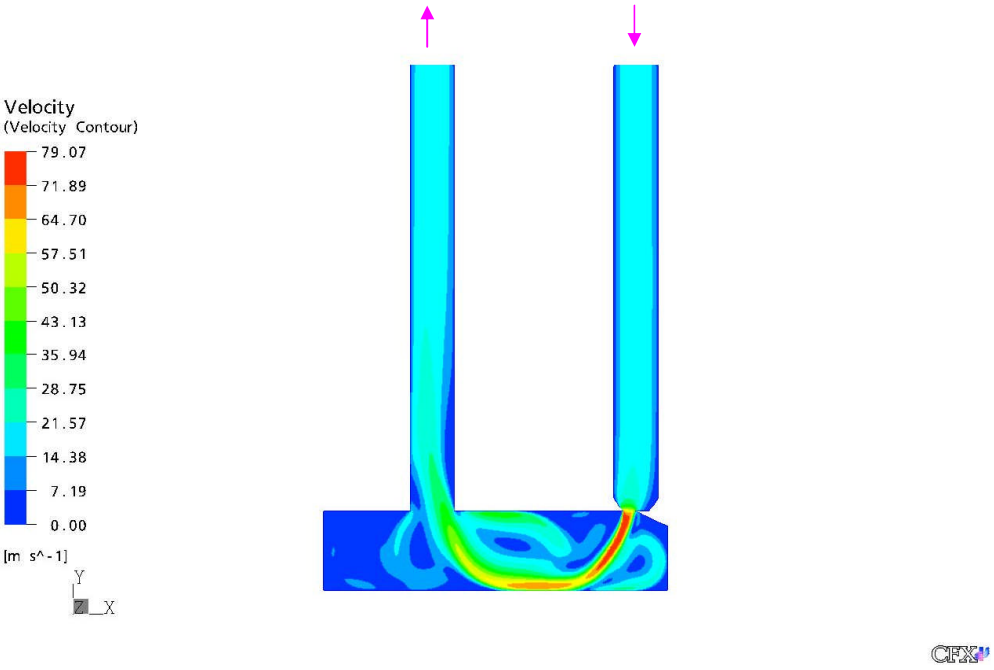

Figure F2.3.1: Velocity contours of the flow field of the sharp edge tapered rim spool for a meter – in orifice (x_v = 0.5 mm)

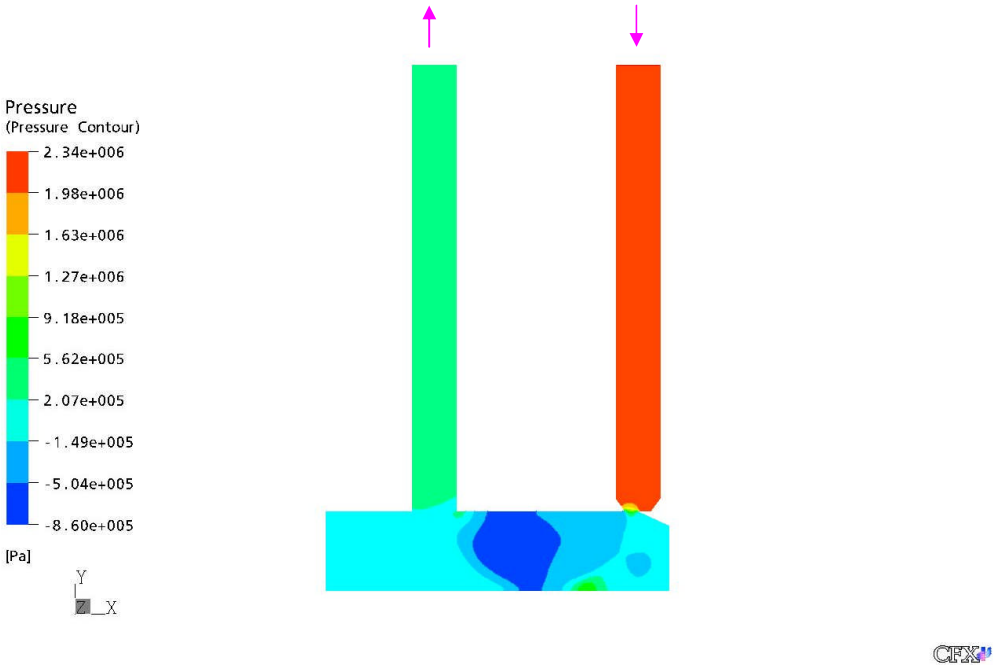

Figure F2.3.2: Pressure contours of the flow field of the sharp edge tapered rim spool for a meter – in orifice (x_v = 0.5 mm)

F3 Velocity and Pressure Contours for Spool Opening of 0.375 and 0.75 mm for the Outflow

This section presents the velocity and pressure field of the flow through the valve for the meter – out orifice. The results are presented in terms of velocity and pressure contour the three different valve configurations and for spool displacement of 0.375 and 0.75 mm.

F3.1 Standard Spool Valve

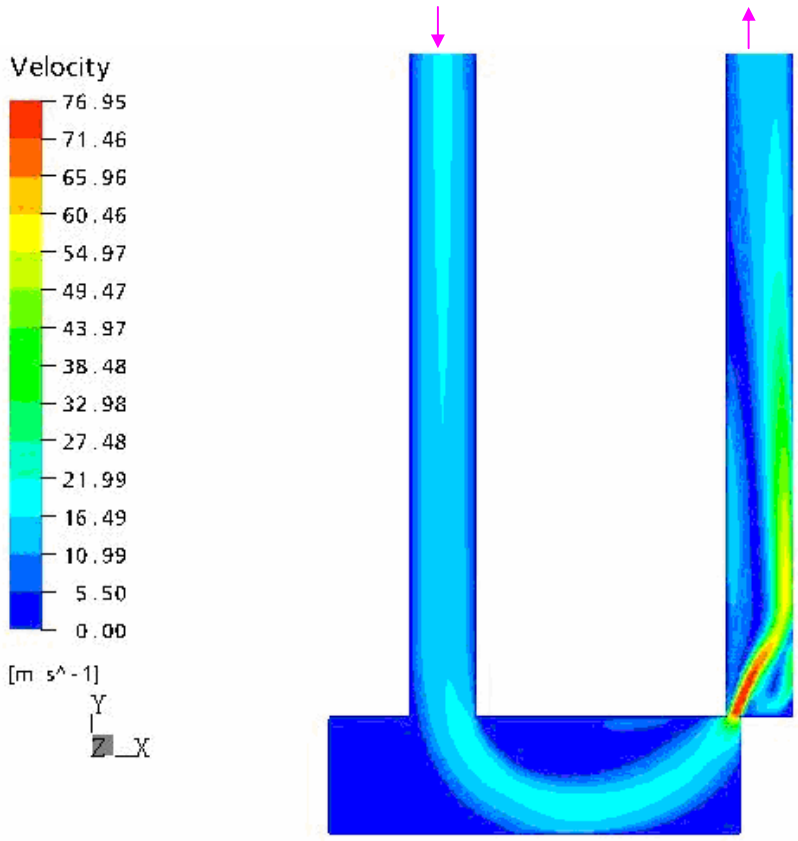

Figure F3.1.1: Velocity contours for the standard spool configuration (x_v = 0.375 mm)

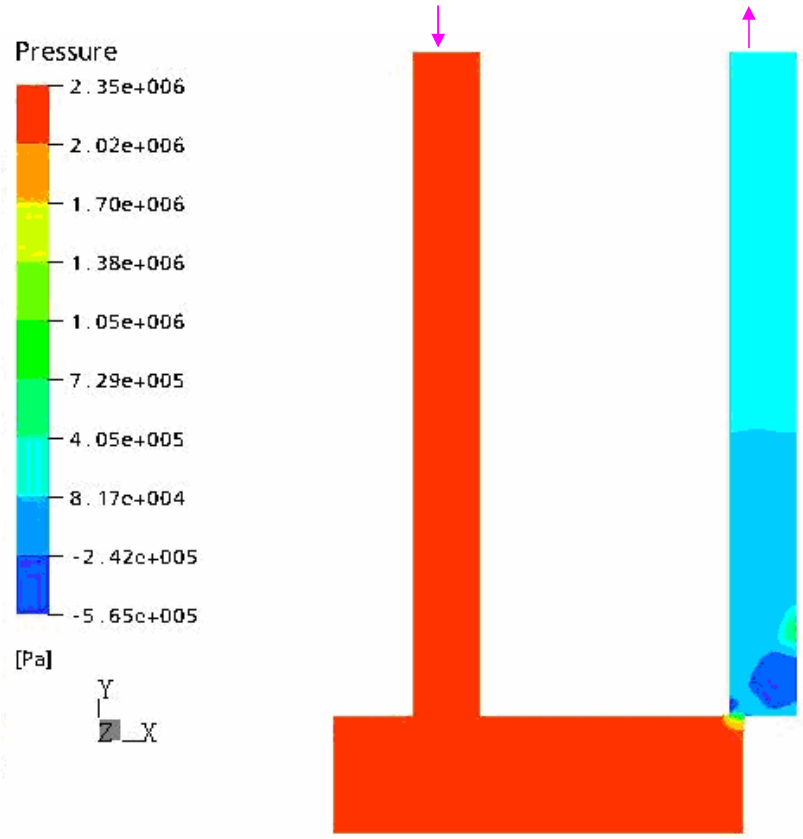

Figure F3.1.2: Pressure contours plot for the standard spool configuration (x_v = 0.375 mm)

F3.2 Rimmed Spool Valve

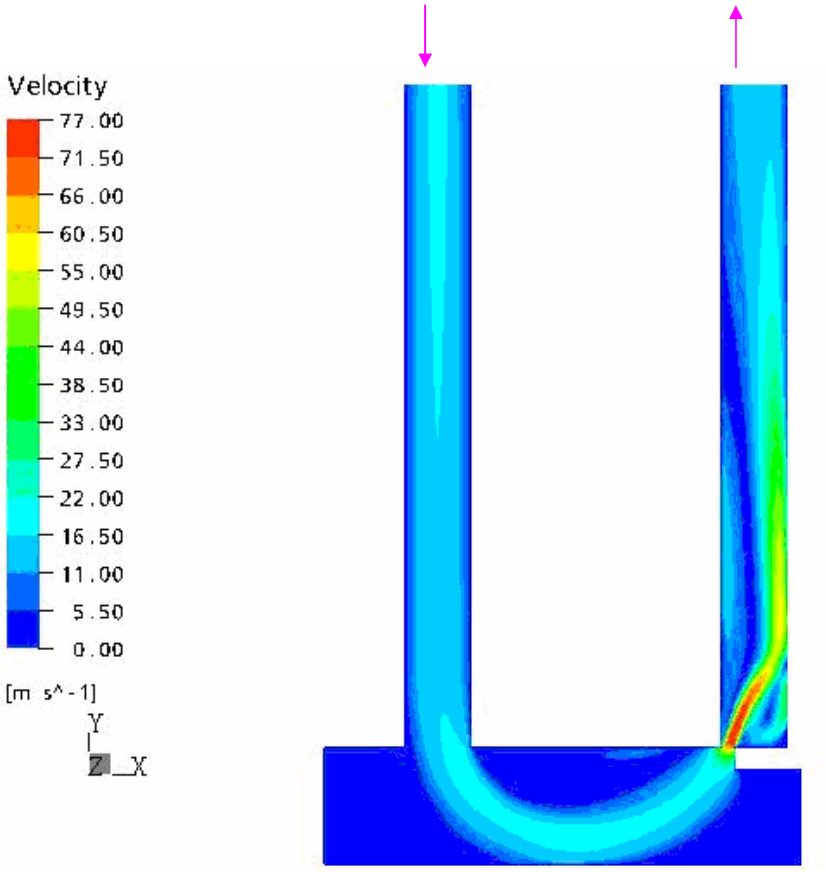

Figure F3.2.1: Velocity contours for the rim spool valve configuration (t = 0.8 mm and x_v = 0.375 mm)

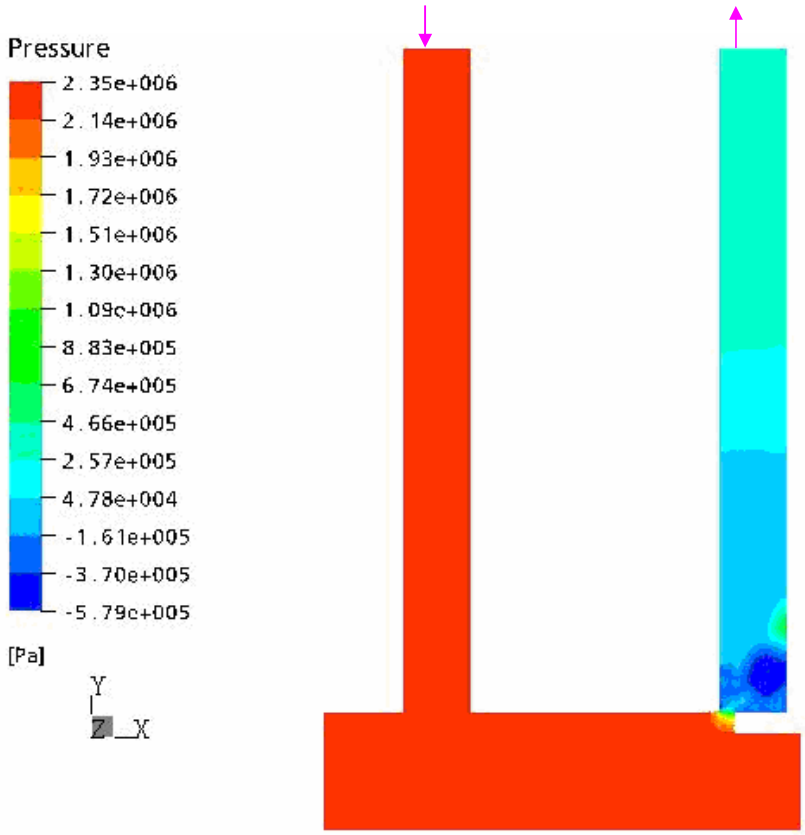

Figure F3.2.2: Pressure contours for the rim spool valve configuration (t = 0.8 mm and x_v = 0.375 mm)

F3.3 Sharp Edge Tapered Rim Spool Valve

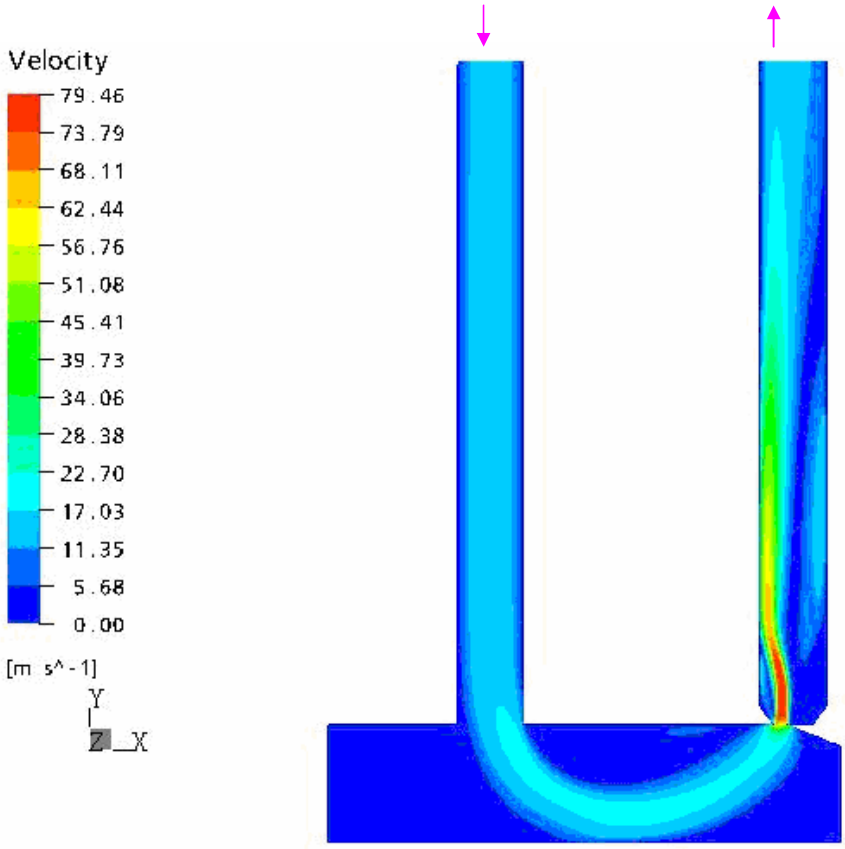

Figure F3.3.1: Velocity contours for the sharp edge tapered rim spool valve configuration ($\theta_1 = 52°, \theta_2 = 18°$ and $x_v = 0.375$ mm)

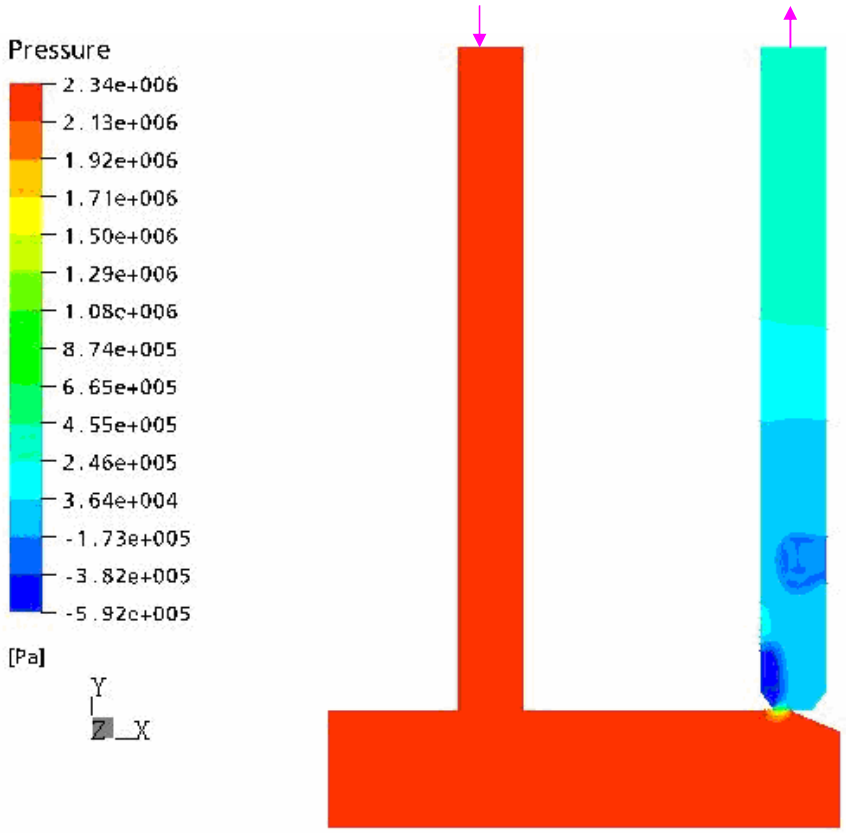

Figure F3.3.2: Pressure contours for the sharp edge tapered rim spool valve configuration

($\theta_1 = 52°, \theta_2 = 18°$ and x_v = 0.375 mm)

Appendix G

Model Parameters and Dynamic Model

The objectives of this appendix are to present the geometry for the flow divider valve studied by Chan et. al (6), to show the dynamic model that was constructed using Matlab / Simulink, and to provide values for the parameters used in the model.
In order to build the model in Simulink, equations (6.3) and (6.5) were rewritten as follows:

$$P_{i1} = P_s - \frac{Q_1^2}{A_1^2 K_1^1} \qquad \text{(G.1)}$$

$$P_{i2} = P_s - \frac{Q_2^2}{A_2^2 K_2^2} \qquad \text{(G.2)}$$

Using these equations, the plots of Figures 6.2 to 6.6 were plotted using the Simulink function code. As an example, flow and pressure, were defined as;

```
plot(Time,flow(:,1),'r',Time,flow(:,2))
```
(G.3)

```
plot(Time,pressure(:,1),'r',Time,pressure(:,2),'g',Time,pressure(:,3))
```
(G.4)

where ‘r’ and ‘g’ indicate red and green colours respectively.

G.1 Geometry for the Without-Rim (WR) Flow Divider Valve

Figure G.1 illustrates the geometry of a flow divider valve spool along with appropriate dimensions. The valve specifications are those used by Chan et al.(6).

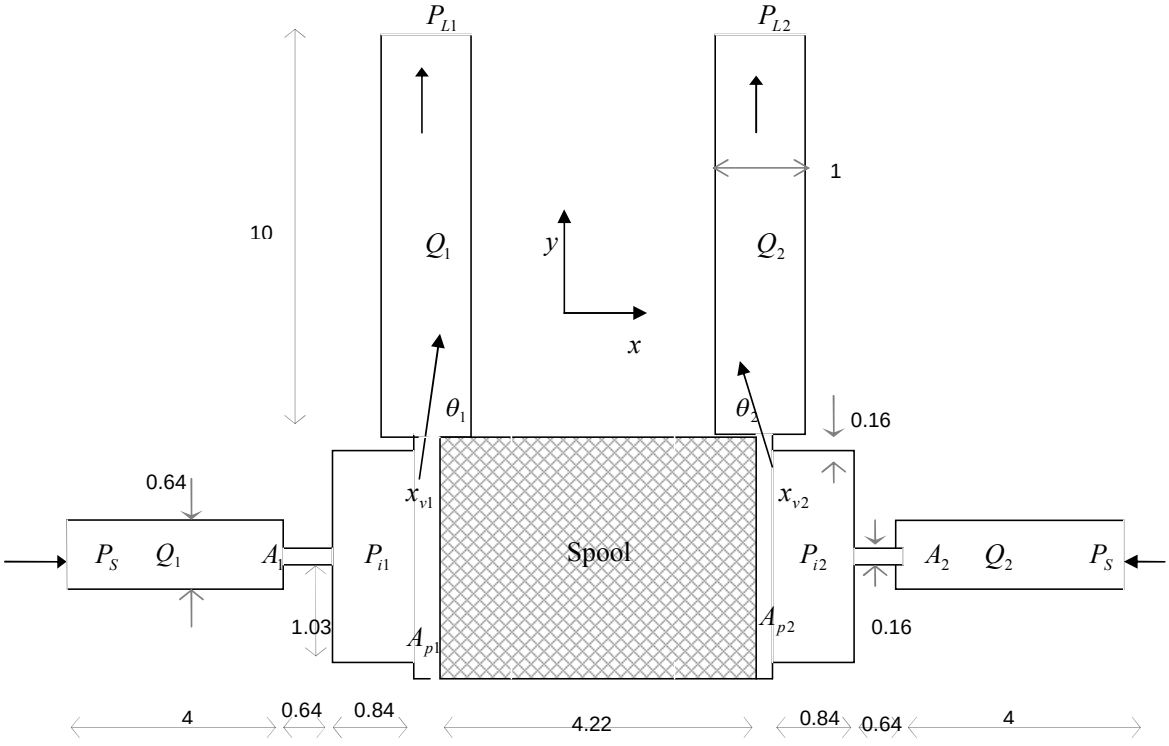

Figure G.1: Schematic of a Flow Divider Valve without the rim (6)

G.2 Parameters for Simulation

This section contains the values for each parameter used in the dynamic model.

Table G. 1: The parameter values used in the dynamic model

Parameters	P_s	P_{l1}	P_{l2}	m	B	A_1 x 10^{-5}	A_2 x 10^{-5}	K	C_d	ρ
Specified Value	3.45 MPa	1.2 MPa	2.4 MPa	0.04 kg	80 Ns/m	3.75 m^2	3.75 m^2	0.03	0.62	871 kg/m^3

G.3 Dynamic Model

This section contains the block diagram of the Simulink model for the simulation of Chan's flow divider valve. The model was constructed using the equations presented in Chapter 5 and the parameter values presented in Table G.1. The inputs of the system are the supply pressure P_S and the two load pressures P_{L1} and P_{L2}. The outputs are the flow Q_1 and Q_2.

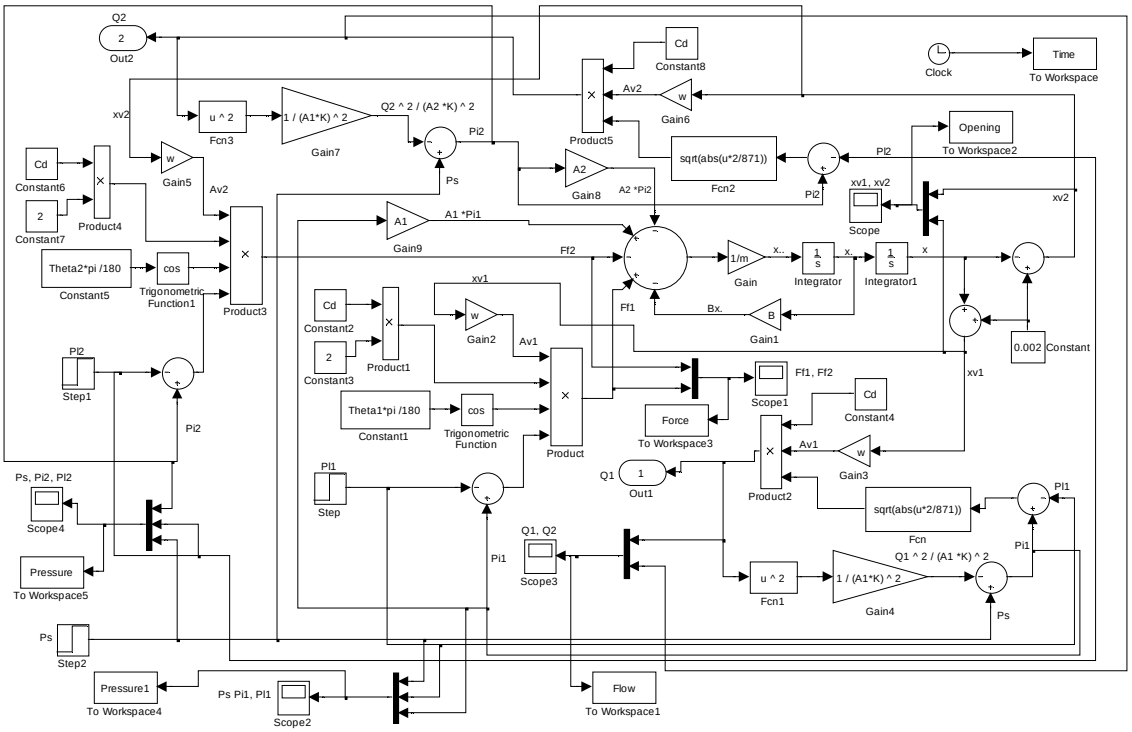

Figure G. 2: The dynamic model